

STINFO/DTIC COPY

AFRL-RW-EG-TR-2009-7020

AUTONOMOUS MICRO AIR VEHICLES WITH HOVERING CAPABILITIES

Sergey Shkarayev

The University of Arizona
Department of Aerospace and Mechanical Engineering
1130 N Mountain Ave.
Tucson, AZ 85721



GRANT NO. FA8651-07-1-0002

February 2009

FINAL REPORT FOR PERIOD APRIL 2007 – AUGUST 2008

DISTRIBUTION A: Approved for public release; distribution unlimited. 96th ABW/PA Approval and Clearance # 96ABW-2009-0067, dated 20 February 2009

AIR FORCE RESEARCH LABORATORY, MUNITIONS DIRECTORATE

■ Air Force Materiel Command ■ United States Air Force ■ Eglin Air Force Base

NOTICE AND SIGNATURE PAGE

Using Government drawings, specifications, or other data included in this document for any purpose other than Government procurement does not in any way obligate the U.S. Government. The fact that the Government formulated or supplied the drawings, specifications, or other data does not license the holder or any other person or corporation; or convey any rights or permission to manufacture, use, or sell any patented invention that may relate to them.

This report was cleared for public release by the 96 Air Base Wing, Public Affairs Office, and is available to the general public, including foreign nationals. Copies may be obtained from the Defense Technical Information Center (DTIC) <<http://www.dtic.mil/dtic/index.html>>.

AFRL-RW-EG-TR-2009-7020 HAS BEEN REVIEWED AND IS APPROVED FOR PUBLICATION IN ACCORDANCE WITH ASSIGNED DISTRIBUTION STATEMENT.

FOR THE DIRECTOR:

//SIGNED//

MIKEL M. MILLER, PhD, DR-IV
Technical Director
Advanced Guidance Division

//SIGNED//

GREGG L. ABATE, PhD, DR-III
Team Lead, Airframe Dynamics & Robust Control
Weapon Dynamics & Controls Sciences Branch

This report is published in the interest of scientific and technical information exchange, and its publication does not constitute the Government's approval or disapproval of its ideas or findings.

REPORT DOCUMENTATION PAGE

Form Approved
OMB No. 0704-0188

Public reporting burden for this collection of information is estimated to average 1 hour per response, including the time for reviewing instructions, searching existing data sources, gathering and maintaining the data needed, and completing and reviewing this collection of information. Send comments regarding this burden estimate or any other aspect of this collection of information, including suggestions for reducing this burden to Department of Defense, Washington Headquarters Services, Directorate for Information Operations and Reports (0704-0188), 1215 Jefferson Davis Highway, Suite 1204, Arlington, VA 22202-4302. Respondents should be aware that notwithstanding any other provision of law, no person shall be subject to any penalty for failing to comply with a collection of information if it does not display a currently valid OMB control number. **PLEASE DO NOT RETURN YOUR FORM TO THE ABOVE ADDRESS.**

1. REPORT DATE (DD-MM-YYYY) 02-02-2009		2. REPORT TYPE FINAL		3. DATES COVERED (From - To) Apr 2007 - Aug 2008	
4. TITLE AND SUBTITLE AUTONOMOUS MICRO AIR VEHICLES WITH HOVERING CAPABILITIES				5a. CONTRACT NUMBER N/A	
				5b. GRANT NUMBER FA8651-07-1-0002	
				5c. PROGRAM ELEMENT NUMBER 62602F	
6. AUTHOR(S) Sergey Shkarayev				5d. PROJECT NUMBER 2068	
				5e. TASK NUMBER 99	
				5f. WORK UNIT NUMBER 20	
7. PERFORMING ORGANIZATION NAME(S) AND ADDRESS(ES) The University of Arizona Department of Aerospace and Mechanical Engineering 1130 N Mountain Ave. Tucson, AZ 85721				8. PERFORMING ORGANIZATION REPORT NUMBER	
9. SPONSORING / MONITORING AGENCY NAME(S) AND ADDRESS(ES) AFRL/RWGN 101 W Eglin Blvd Eglin AFB, FL 32542				10. SPONSOR/MONITOR'S ACRONYM(S) AFRL-RW-EG	
				11. SPONSOR/MONITOR'S REPORT NUMBER(S) AFRL-RW-EG-TR-2009-7020	
12. DISTRIBUTION / AVAILABILITY STATEMENT DISTRIBUTION A: Approved for public release; distribution unlimited. 96 th ABW/PA Approval and Clearance # 96ABW-2009-0067, dated 20 February 2009.					
13. SUPPLEMENTARY NOTES					
14. ABSTRACT In this project was investigated novel concepts of micro aerial vehicles (MAVs) with vertical takeoff and landing capabilities. Two fixed-wing MAV configurations were tested in a wind tunnel. These concepts were a tilt-wing concept MAV by two non-coaxial counter-rotating propellers and a tilt-body concept based on coaxial motors and counter-rotating propellers. Values of thrust, torque, power, and efficiency were measured for these concepts. The development of an automatic control system and the investigation of the flight dynamics of the VTOL MAV during the hovering phase of flight were undertaken for the second stage of the project. The second focus of the project was on the development of a dynamic model for a flapping-wing air vehicle (ornithopter) and on the identification of the model parameters for this vehicle using in-flight data. The system identification procedure is proposed based on the value of a scalar objective function in the least squares sense. Finally, the ornithopter was equipped with an automatic control system that provides stability augmentation and navigation of the vehicle and flight data acquisition. Wind tunnel tests were conducted with the control surfaces fixed in neutral position and the flapping motion of the wings activated by a motor at a constant throttle setting. Coefficients of a lift, drag, and pitching moment were determined.					
15. SUBJECT TERMS Hovering MAVs, Micro Munitions, MAV, Loitering MAV					
16. SECURITY CLASSIFICATION OF:			17. LIMITATION OF ABSTRACT	18. NUMBER OF PAGES	19a. NAME OF RESPONSIBLE PERSON
a. REPORT	b. ABSTRACT	c. THIS PAGE			Gregg Abate
UNCLASSIFIED	UNCLASSIFIED	UNCLASSIFIED	UL	114	19b. TELEPHONE NUMBER (include area code) 850 883 2596

Standard Form 298 (Rev. 8-98)
Prescribed by ANSI Std. Z39.18

This page intentionally left blank

Table of Contents

Abstract.....	1
Results.....	5
Recommendations	7
Appendix 1: Aerodynamic Design of VTOL Micro Air Vehicles.	9
Appendix 2: On Fixed-Wing Micro-Air Vehicles with Hovering Capabilities.....	29
Appendix 3: Investigation of Flight Dynamics and Automatic Controls for Hovering Micro Air Vehicles.	45
Appendix 4: Dynamic Model and System Identification Procedure for Autonomous Ornithopter.....	65
Appendix 5: Flight Dynamics of Flapping-Wing Air Vehicle.	79
Appendix 6: Autonomous Micro Air Vehicles with Hovering Capabilities.....	93

This page intentionally left blank

Abstract

This report presents research studies performed under the Statement of Work for the Grant FA8651-07-1-0002. The report is organized in six chapters comprised of papers published during the course of the project.

In the present project, we investigated novel concepts of MAVs with vertical takeoff and landing capabilities. Two fixed-wing MAV configurations were tested in the wind tunnel and compared: a tilt-wing concept controlled by two non-coaxial counter-rotating propellers and a tilt-body concept based on coaxial motors and counter-rotating propellers. The tilt-wing concept, although superior to the tilt-rotor concept, does not provide a significant benefit over an equivalent tilt-body MAV configuration. Finally, two tilt-body coaxial prototypes were designed and successfully flight tested to demonstrate the capability of fixed-wing MAV configurations to lift off, sustain hover flight, and perform transition between forward and hover flight. Special attention was paid to the coaxial tail-sitter concept for which the propellers slipstream guarantees aerodynamic efficiency over the whole flight envelope. Side-by-side comparison of a mini- and a micro-sized coaxial tail-sitter model was carried out and discussed.

The tilt-body, tail-sitter concept for VTOL MAVs was analyzed and designed based on a contra-rotating propeller-motor electric propulsion system. It can be equipped with video cameras that capture and transmit video to a ground station for analysis, making it a very effective research platform. Values of thrust, torque, power, and efficiency of this propulsion system were measured in pusher and tractor arrangements of propellers and compared against single motor-propeller propulsion. With comparable efficiency, the developed propulsion system has very little propeller torque. Hot-wire measurements have been conducted to investigate the velocity profile in slipstream. Wind tunnel testing was conducted for a motor, a wing, and an arrangement of a wing with a motor. The drag force on the wing is produced by two mixing airflows: free stream and propeller-induced pulsating slipstream. A drag force model based on the classical propeller momentum theory was introduced in the present study, and a formula for the drag coefficient for the wing in the presence of a free stream and slipstream is derived. The results of this study were utilized in the design of a VTOL MAV prototype that was successfully flight tested.

The development of an automatic control system and the investigation of the flight dynamics of the VTOL MAV during the hovering phase of flight were undertaken for the second stage of the project. A state-space model was formulated and used in a control law design. The effects of propeller slipstream impinging on the airframe are discussed in the context of control design. Feedback control laws based on a proportional, integral, and derivative (PID) control were developed and programmed into the autopilot. The development and evaluation of two VTOL MAVs with wingspans of 65 and 31 cm are presented. A number of test flights of vehicles with attitude stabilization and altitude hold were conducted with telemetry acquisition. Despite the difference in size, similarities were noted in the dynamic responses for both aircraft. The actuation delays in the propulsion systems caused a systematic error in altitude. Average amplitudes of rotational oscillations in all three axes were also about the same for both aircraft. Higher roll rates were explained by lower inertia in roll axis.

The second focus of the project was on the development of a dynamic model for a flapping-wing air vehicle (ornithopter) and on the identification of the model parameters for this vehicle using in-flight data. The proposed dynamic model combines the flapping wings motion with the motion of the ornithopter's center of mass. A set of six equations in the integral form was obtained for the motion of the center of mass of the ornithopter. The aerodynamic forces acting on the wing during one full stroke are presented as a sum of stroke-averaged forces, acting during upstroke and downstroke. The dynamic model is linearized with respect to the state variables and the equations of motion are obtained for the longitudinal mode in state-space form. Parameters of the linearized model are conventional stability and control derivatives. The system identification procedure is proposed based on the value of a scalar objective function in the least squares sense.

Finally, the ornithopter with a wing span of 74-cm was equipped with an automatic control system that provides stability augmentation and navigation of the vehicle and flight data acquisition. Wind tunnel tests were conducted with the control surfaces fixed in neutral position and the flapping motion of the wings activated by a motor at a constant throttle setting. Coefficients of a lift, drag, and pitching moment were determined. In addition, variations of derivatives of aerodynamic coefficients with the freestream velocity were investigated. A series of flight tests were conducted with fixed controls demonstrating ornithopter stability in all axes. Proportional control laws were programmed into the autopilot for the closed-loop controls. A

number of test flights of the autonomous ornithopter were conducted with the telemetry acquisition. During the autonomous flights, the autopilot performed waypoint and altitude navigation demonstrating stable performance.

Based on the results of international MAV competitions, no other university has demonstrated the level of mastery of the UA team in creating autonomous micro MAVs. The 1st US-Asian Demonstration and Assessment of Micro Aerial and Unmanned Ground Vehicle Technology was held in Agra, India, March 10-15, 2008. For the competition, the University of Arizona team used an MAV system that includes two types of MAVs developed under the present project that are capable of performing three separate missions. Twelve teams from universities and companies from the US, France, Germany, Netherlands, Japan, Australia, Spain, and India participated in this competition. The University of Arizona team received the following awards: Best Mission Performance (tied with 3 other teams), Best design, and US Army Aviation & Missile Research Development & Engineering Center (ARMDEC) Meritorious Award.

The results of the study presented in this report have been disseminated via seven conference and two journal papers, and presented at six conferences and seminars. As part of the technology transfer, we worked closely with the Battle Command Battle Laboratory (Ft. Huachuca, Arizona) and provided them with results of the present study. One MS thesis by Bharani Malladi was completed in December of 2007 and one PhD thesis by Bill Silin is in progress and expected by May 2009.

This page intentionally left blank

Results

The results of this grant have been very well documented in five conference papers and one presentation that are included as appendices to this report. The following task outline highlights the results and progress under this grant and refers the reader to the appropriate appendix.

Task 1. Conceptual design of fixed-wing VTOL MAVs [Completed Sept 2007]

- 1.1 Flight performance analysis for three VTOL MAV concepts
- 1.2 Development of novel propulsion and design method for VTOL

Appendices: [1, 2]

Task 2. Aerodynamics of fixed and flapping wings [Completed March 2008]

- 2.1 Studies on VTOL MAV propulsion
- 2.2 Wind tunnel measurements on wing under free stream and slipstream
- 2.3 Development of model for zero-lift drag of thin cambered wing
- 2.4 Wind tunnel studies on an ornithopter

Appendices: [1, 2]

Task 3. Flight testing of VTOL MAVs [Completed May 2008]

- 3.1 Test flights with stability augmentation
- 3.2 Studies on automatic controls for VTOL MAV in hover
- 3.3 Technology demonstration and assessment

Appendices: [5, 6]

Task 4. Flight dynamics and controls of flapping-wing MAVs [Completed Sept 2007]

- 4.1 Dynamic model for an ornithopter
- 4.2 Integration of autopilot into ornithopter
- 4.3 Flight dynamics of an ornithopter

Appendices: [3, 4, 6]

This page intentionally left blank

Recommendations

Theoretical and experimental capabilities developed in the course of the project will enable investigations of the following challenges in future micro flight research.

1. **Unsteady Aerodynamics of Rapidly Maneuvering MAVs.** High rotational rate maneuvers at high angle of attack cause unsteady flow regimes. Flight experiments with data acquisition by micro autopilot and wind tunnel measurements utilizing sensitive sting balance will be conducted on MAVs with vertical takeoff and landing capabilities. The unsteady aerodynamic effects on small aircraft cannot be adequately described with time-invariant aerodynamic coefficients and linear dynamic models. Therefore, an approach based on state-space formulation will be developed providing a direct coupling of unsteady flow with flight dynamics. This approach enables system identification through the measurements of the quasi-steady and transient responses from appropriate maneuvers.
2. **Basic Experimental and Theoretical Studies on Aerodynamics and Controls of Flapping Wings.** Instantaneous aerodynamic forces and deformations in membrane flapping wings will be measured using sensitive sting balance and high-speed cameras, respectively. Reduced-order flapping-wing model for forces as functions of initial wing shape parameters will be derived. This model will be integrated into multi-body dynamic model of a flapping-wing apparatus making possible the development of aerodynamic controls by way of wing shape changes.
3. **Non-Linear Dynamic Effects and Development of Control Laws for Autonomous Micro Air Vehicles.** Non-linear dynamic effects will be investigated using flight data acquired by micro autopilots and high-speed cameras during rapid maneuvers in wall and ground proximity. Dynamic models for fixed- and flapping-wing micro aerial vehicles will be developed. The nonlinear nature of the micro flight suggests a control design based on adaptive algorithms for gain scheduling. Finally, flight tests of novel MAV designs are planned in order to examine a correlation with theoretical results and to adjust developed control laws.

This page intentionally left blank

Appendix 1

Aerodynamic Design of VTOL Micro Air Vehicles

This page intentionally left blank

Aerodynamic Design of VTOL Micro Air Vehicles

Sergey Shkarayev¹

The University of Arizona, Tucson, AZ, USA, 85721

Jean-Marc Moschetta² and Boris Bataille³

SUPAERO, Toulouse, France, 35055

The research and development efforts outlined in this paper address the aerodynamic design of micro air vehicles (MAVs) with hovering, vertical take-off, and landing capabilities (VTOL). The tilt-body configuration of the VTOL MAV is proposed based on the propulsion system consisting of two coaxial contra-rotating motors-propellers. Values of thrust, torque, power, and efficiency of this propulsion system were measured in pusher and tractor arrangements of propellers and compared against single motor-propeller propulsion. With comparable efficiency, the developed propulsion system has very little propeller torque. Hot-wire measurements have been conducted to investigate the velocity profile in slipstream. The lower average velocity and significant decrease of velocity in the core of the slipstream found in the tractor arrangement are mostly due to the parasite drag caused by the motors. It causes the decrease of the thrust force observed for the tractor arrangement in comparison with the pusher one. Wind tunnel testing was conducted for a motor, a wing, and an arrangement of a wing with a motor. The drag force on the wing is produced by two mixing airflows: free stream and propeller-induced pulsating slipstream. The zero-lift drag coefficient increases by about three times with propeller-induced speed increase from 0 to 15 m/s indicating the change of transition mechanism in the boundary layer from a laminar to turbulent state. The results of this study were realized in the design of a VTOL MAV prototype that was successfully flight tested.

Nomenclature

C_D	=	drag coefficient
C_{D_0}	=	zero-lift drag coefficient
C_L	=	lift coefficient
c	=	chord
F_{total}	=	total force measured by a wind tunnel balance
P	=	electric power input
P_{ind}	=	induced power
Q	=	torque
R	=	propeller radius
R_m	=	maximum distance of velocity measurements from the s -axis
Re	=	mean aerodynamic chord Reynolds number
S_0	=	wing area
S_p	=	area of a part of the wing covered by propeller slipstream
S_s	=	area of the side wall
T	=	thrust force
T_s	=	thrust force determined from air velocity data
V_0	=	free stream velocity

¹ Associate Professor, Aerospace and Mechanical Engineering Dept., 1130 N. Mountain Ave.

² Professor, Department of Aerodynamics, SUPAERO BP 54032.

³ Research Assistant, Department of Aerodynamics, SUPAERO BP 54032.

W	=	take-off weight of an aircraft
$w(s)$	=	induced velocity based on propeller momentum theory
w_e	=	measured induced velocity
w_{ult}	=	ultimate propeller-induced velocity
α	=	angle of attack
ρ	=	air density

I. Introduction

THE truly successful use of MAV technology is somewhat difficult without the capability of aggressive vertical maneuvering and hovering autonomously. One way to fulfill these requirements is in the design of rotary wing MAVs, and several helicopters have been developed in recent years. However, they are sensitive to air turbulence due to their large rotor disc. In general, when compared to fixed-wing aircraft, rotorcrafts have a smaller range, endurance, and payload capacity.

Design methods and general theoretical aerodynamic principles for large VTOL aircraft are well developed and have been summarized in the literature.^{1,2} As the field of VTOL evolved, much attention was paid to propulsion system considerations and development of an aerodynamic theory for the propeller and rotor. Other subjects included design studies of configurations and control issues during hover and transition. Overall, there is a sufficient amount of relevant data and knowledge to begin exploring the VTOL concept with applications to MAVs.

In the present study, we begin a research project on novel fixed-wing MAVs capable of vertical take-off and landing, and hovering, based upon our previous successful designs. The University of Arizona has developed one of the world's smallest mission-capable autonomous MAVs, the Dragonfly.³ Obviously, adding hovering capabilities to these aircraft requires additional motor power to get off the ground without using the wings' aerodynamics. Another technical problem is in controlling the vehicle transition from vertical to horizontal flight. In order to provide effective control at low speed, the MAVs will feature large control surfaces and throws, changing the baseline design in a significant way. The present project will also benefit from an independent experimental study of the "Vertigo" concept developed at SUPAERO.⁴ The Vertigo consists of a fixed delta wing powered by coaxial contra-rotating propellers and side by side motors. Its capability to hover and transition flights has been recently demonstrated on a radio-controlled prototype.

In the following discussion, the two concepts for VTOL MAVs will be briefly presented, and their aerodynamics, performance, and controls will be examined. The two concepts are (1) single propeller tilt-body aircraft and (2) contra-rotating propellers tilt-body aircraft.

Aerobatic single-propeller RC aircraft emerged as a result of the integration of the latest developments in electric motor and battery technology into a lightweight structure. With high thrust-to-weight ratio and large control surfaces and throws, these airplanes can perform spectacular aerobatic maneuvers. However, they feature a very low wing loading, resulting in a very low flight speed.

In general, designing of a single-propeller tilt-body MAV is largely affected by the following basic issues of the propulsion itself: propeller torque, p-factor, swirling slipstream, and gyroscopic moment. The propeller torque, which appears as a left rolling tendency, is a serious drawback in a single propeller-driven aircraft. Typically, the wingspan of aerobatic airplanes is greater than 1 m, which limits the maximum torque-roll rate by about 180° per second, allowing an inexperienced pilot to control the airplane. The maximum size for MAVs is 3-5 times smaller. Assuming that the torque-roll rate is inversely proportional to the square of the wing span, if the wingspan of an MAV decreases by a factor of 2, the torque-roll rate increases by a factor of 4. Thus, the torque-roll may become a driving factor in the design of the control system for VTOL MAVs.

Another negative effect in the single-propeller-driven aircraft is the p-factor that occurs as a result of the difference in angle of attack between the blades of a rotating propeller and causes a single-engine propeller aircraft to yaw to the left. Keeping the rudder to the right helps to maintain straight flight, however, as a consequence, the aircraft drag increases.

The effect of the rotational airflow is inherent to a single-propeller propulsion system. The air rotating into a twisting helix around the fuselage presses against the left side of the ventral vertical tail, causing the plane to yaw and roll to the left. It also results in energy losses, reducing overall thrust efficiency of the propulsion.

In a tilt-body VTOL with contra-rotating propellers, the second coaxial propeller is installed immediately behind the first one and rotates in the direction opposite to the rotating flow after the first one. The air flow coming out of contra-rotating propeller is symmetrical, without a torque and side forces. The induced velocity behind the first propeller may increase the total thrust of the system in comparison with two propellers staying apart.

In 1953-55, Convair designed and successfully tested the XFY-1 Pogo aircraft with contra-rotating propellers. Pogo has successfully completed VTOL flights, but the project was cancelled at completion of the test program. A jet tail-sitter, Ryan X-13 Vertijet, also completed VTOL flights in 1956-57. Historically, large tilt-body tail-sitters have been envisioned for military use on both land and sea in situations disallowing airfields, or for operating from limited space. Although short-lived, tail-sitters paved the way for fixed-wing, jet-thrust-vector aircraft, such as the Harrier. Among the problems, the pilot's uncomfortable accommodation was an important one, which, of course, is not important for unmanned air vehicles. Therefore, the tail-sitter designs with contra-rotating propellers-motors are the focus of the current project.

Aerodynamic interaction of the wing with the propeller was studied by Prandtl⁵ in a wind tunnel. In a series of tests, lift, drag, and pitching moment on the wing and propeller thrust were measured. Increase of the drag was found to be noticeable when the wing propeller is right behind the propeller. One of the issues of the interpretation of propeller-wing interaction is the right choice of reference speed. The increase of the speed behind the propeller was used⁵ for the explanation of the effect of drag increase, however, only a free stream speed was employed as a reference speed in the drag coefficient calculations, thus, not taking into account actual propeller-induced velocity.

In general, a propeller generates a pulsating slipstream that can diminish the enhanced performance of laminar wings in a tractor configuration. On the other hand, a pure pusher configuration is not an acceptable solution for VTOL aircraft that employ a propeller slipstream in aerodynamic controls.

In an earlier work,⁶ the laminar boundary layer was investigated on the NACA 27-212 airfoil in the presence of a free stream and propeller slipstream. It was found that the laminar-to-turbulent transition point is moving toward the leading edge of the wing, causing a significant increase in the drag.

One of applications of large unmanned air vehicles is for high-altitude surveillance. Aerodynamic design of this class of vehicles requires investigation of propeller-wing interaction at low Reynolds numbers, but at high subsonic Mach numbers. Hot-film measurements were conducted in study⁷ in order to determine laminar, transitional, and turbulent boundary layer states. It was concluded that propeller-induced slipstream does not eliminate laminar separation bubble. Note that test conditions corresponded to Reynolds number of 5×10^5 and relatively low propeller's RPM.

The effect of a propeller slipstream on the wing laminar boundary layer was investigated⁸ with the help of hot-wire sensors. Measurements in the boundary layer on the wing surface showed the periodic change of the laminar velocity profile to turbulent and back at the same rate as of the propeller rotation.

Additional references on the boundary layer transition as a function of a turbulence can be found elsewhere.⁹ It is important to emphasize the fact that the previous studies⁶⁻⁸ were performed for Reynolds numbers and thrust values relevant to large aircraft and high speed flights. Also, these studies were concerned with a rotational flow behind a single-propeller. Consequently, the results of the previous studies may or may not be applicable to the flow conditions pertaining to VTOL MAVs. Studies of slipstream disturbances and corresponding boundary layer flows characteristic to low Reynolds numbers free streams and slipstream induced by small propellers with high RPM are needed.

Since 2001, electric motors and lithium polymer batteries, especially those mass-produced for cellular phones, have become an enabling technology for MAVs.¹⁰⁻¹² The components of electric propulsion systems and guidelines for their evaluation and selection have been presented in detail for MAV applications.¹³

Effects of propulsive-induced flow on aerodynamic characteristics of MAVs in tractor configurations with a wing right behind a propeller have been studied experimentally.¹⁴ A significant increase in lift coefficients (referred to a dynamic pressure in the free stream) and the delayed stall phenomenon was reported, especially when it comes to low-speed flight performance. The delayed stall seen with the induced propeller flow would allow a MAV to attain a higher angle of attack before aerodynamic stall, and hence attain a higher lift coefficient and slower flight speed than what would be thought possible just from wing aerodynamics alone. On the other hand, it was noticed that the lift-to-drag ratio for nearly all angles of attack are greater for the wing-only tests. It appears that even though the lift coefficients are increased due to the induced flow, the subsequent increase in the drag coefficient, both from the added lift and the parasite drag of the motor/propeller combination, increases the drag by a more substantial amount, leading to the decrease in the lift-to-drag ratios. To the contrary, investigations of a bi-plane configuration showed that the pusher arrangement of the propeller improves the overall performance of the vehicle.¹⁵

VTOL capabilities pose difficult problems for the fixed-wing MAV design. VTOL MAVs flying at low Reynolds numbers will have relatively large propeller sizes and larger control surfaces and throws. Owing to the complexity of the propeller-wing interactions, no design methods exist for sizing these airplanes. Therefore, in the present study, the aerodynamics of VTOL MAVs will be studied through wind tunnel measurements on the propulsion system consisting of two coaxial contra-rotating motors-propellers, wing, and wing-propeller combinations. As evident from the above discussion, the tilt-body concept with contra-rotating propellers

represents a workable solution for the reduction or elimination of negative effects of other concepts. In the present study, a tilt-body VTOL MAV was designed based on previous successful designs.^{3,4}

II. Models and Methods

A. Propulsion System for VTOL MAVs

The propulsion system shown in Fig. 1 consists of two pairs of coaxial contra-rotating motors and propellers. Each propeller is powered by a separate motor, rotating in opposite direction. This propulsion system was assembled by utilizing off-the-shelf brushless outrunners, MP Jet AC 22/4-60D.¹⁶ The motors are joined at their stator backplates. The outrunner motors have a sufficient space inside the stators to allow a cross shaft through both motors, as shown in Fig. 1. The propeller 1 is attached to one end of the cross shaft and the other end is fixed to the rotor case of motor 1. The rotor of motor 2 was modified with an extended shaft, which also houses two bearings supporting the cross shaft. The motors have a diameter of 27 mm, and the total length of the propulsion is 60 mm. In this work, the motors are regulated by an electric speed controller, Phoenix-25, providing the same RPM (revolutions per minute) to both motors. The effect of unequal RPMs may be of interest for future studies, especially with regard to possible roll controlling of a vehicle through the differential RPMs.

Two arrangements of the propellers with respect to the motors were analyzed: tractor and pusher. In a tractor configuration, propellers are attached to the motors such that the thrust force is generated in the positive direction of the s -axis and the propeller slipstream hits the motors. For the pusher configuration, shown in Fig. 1, propellers were flipped 180°, and the polarity of the electric power was set to opposite. Propellers used are APC with a 140-mm diameter (radius $R = 75$ mm) and 114 mm-pitch. The distance between propellers is 17 mm.

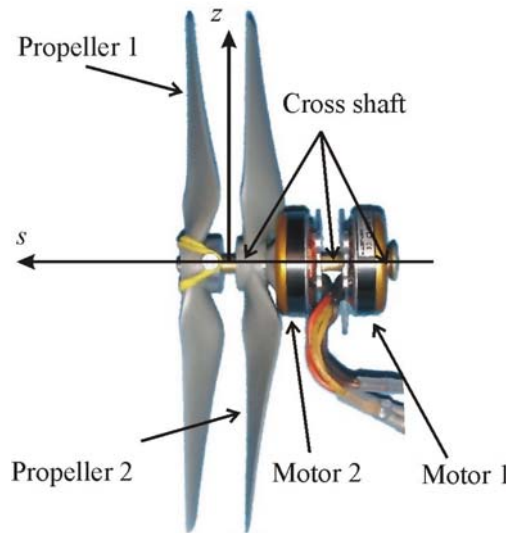


Fig. 1 Propulsion system of two coaxial contra-rotating motors-propellers.

B. Wing Design

The Zimmerman planform wing with a 254-mm wing span, 169-mm root chord, and aspect ratio of 1.91 is studied in this work. The S5010-TOP24C-REF airfoil¹⁷ was utilized in designing the wing, with a maximum camber of 3% located at $0.24c$ and an inverse camber of 1% at $0.85c$. The wing geometry, presented in Fig. 2, was generated using SolidWorksTM as described in Ref. 18. It is stiffened by a plywood rib along the root chord, as shown in Fig. 3. The mold was manufactured employing 3D Printer InVision Si2. No fuselage or controls were attached to the wing studied in this work.

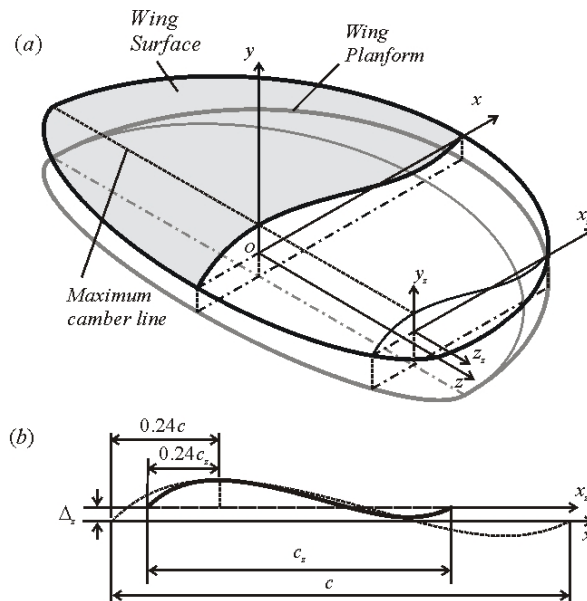


Fig. 2 Zimmerman wing (a) and representative cross section (b).

C. Motor Testing Bench and Hot-Wire Measuring System

The SUPAERO Propulsion Lab motor testing bench is used for the evaluation of small electric motor propulsion. It measures RPM, current, thrust and torque, with the voltage holding constant. Two load cells provide thrust and torque values. Calibration of the devices was done by applying a calibrated mass to the sensors. The resolution for the thrust force was 0.005 N and for the torque 0.2 N mm.

A hot-wire measuring system has been used to investigate the velocity profile of propeller flow. The sensor is a 2D hot-wire, Model 1241-20 from TSI. It allows two normal velocity components to be measured, but in this study only axial flow velocity was used. This sensor is managed by an IFA 300 constant-temperature anemometer system from TSI. The two electric signals resulting from this acquisition system are translated into two velocity values using a MATLAB routine on the acquisition computer. Calibration of the acquisition system is achieved in the wind tunnel test section. A 2D map of each wire voltage is generated using wind speed and sensor angle as the two input parameters. Discrete values of wind speed from 0 to 30 m/s are set with a step of 1 m/s. For each wind speed, the sensor angle is set from -45° to 45° , with a 1° step. The resulting 2D map for one wire is a continuous surface. A voltage value for this wire will result in a line in the (wind speed, angle) plane. Given a voltage for each wire, the intersection of the resulting lines will lead to a single point equivalent to unique speed and angle values. This calibration method provides better accuracy for the whole measurement range than the usual polynomial formula. The wind speed measured during calibration is provided from a calibrated Pitot tube, whose accuracy is better than 0.1 m/s for the speed range obtained from the propeller flow. The angle is measured by a digital potentiometer, which has a precision of 0.01° .

Experimental arrangements for testing a wing with a motor is presented in Fig. 3. For testing of the motor only, the wing was removed and testing was conducted using the same fixture.

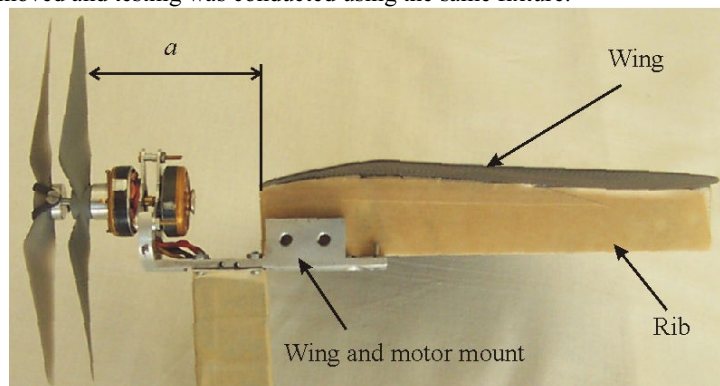


Fig. 3 Experimental arrangements for testing of a wing with a motor.

D. Wind Tunnel Facility

The SUPAERO low-speed wind tunnel is a closed-loop wind tunnel where test section has a 0.45×0.45 m cross section and is 0.7 m long. The contraction ratio is 6.2 and the turbulence level is 1%. Speeds from 2 m/s to 30 m/s can be obtained with a standard deviation below 0.2 m/s.

The balance measures all the aerodynamic components except for the side force. It is composed of 6 single-ended load cells. Three struts, each linked to 2 cells, go through the test section floor and connect to the test model. Balance calibration is achieved by computing the calibration slope of each cell using calibrated weights. The resolution for forces is less than 0.004 N.

A calibration of the wind tunnel and the balance was performed before each test series. Utilizing calibration measurements and the small-sample method,¹⁹ the uncertainty intervals in aerodynamic coefficients were determined. Standard deviations of aerodynamic coefficients were estimated. Solid blockage, wake blockage, and streamlined curvature corrections were estimated based on the methods described in Ref. 20.

III. Evaluation of Propulsion System

A. Motor Static Testing

The performance in hover and vertical climb of a VTOL aircraft is a driving factor in the take-off weight determination and power selection. Since these flight conditions are characterized by a relatively low speed, knowledge of the static thrust at zero free stream velocity becomes very important. Other parameters affecting the design include torque, RPM, and power requirements. Several propulsion systems were evaluated on the motor testing bench. The tests were conducted for a constant voltage from 6 to 11 V, with a step of 0.5 V. With the voltage set, the motor(s) was started and measurements were taken at the control signal to the motors in terms of PWM (pulse width modulation) varied from 50% to 80%, where the former corresponds to 1.5 ms and latter to 1.8 ms. Both tractor and pusher arrangements of contra-rotating propulsion were investigated, as well as a conventional single motor-propeller setup.

In Fig. 4, the variation of thrust and torque with PWM is presented for the tractor at 11 V. The thrust force increases linearly with PWM and reaches a maximum at 3.42 N and at 12,000 RPM. This thrust is 1.9 greater than the thrust generated by a single propeller-motor under the same voltage and PWM. Thus, there is a small loss of the thrust in the contra-rotating system compared to a single propeller-motor, which can be explained by the non-optimal propellers selected for the present study. Note that the linear relationship simplifies thrust control in an automatic system.

The maximum torque in this test was 0.42 N cm, which is also the maximum torque measured in all tests conducted for contra-rotating systems. As expected, this torque was about 10 times lower in comparison with a torque measured on a single propeller-motor system. This feature of the contra-rotating propulsion significantly simplifies controls for VTOL aircraft, and it is a major advantage of the presented propulsion system.

Figure 5 shows static thrust generated by both pusher and tractor propulsion systems as a function of electric power input. The presented data provide estimates of the power required for hovering flight and can be used for battery selection. As evident from Fig. 5, the pusher propulsion generates 20-23% more thrust force than the tractor for the same inputted power. It directly affects the take-off weight and flight performance of the vehicle in hover and climb. In the tractor configuration, the motor is placed right behind propellers and, therefore, creates a significant parasite drag. Hence, the shape optimization of the motor mount and fuselage is another important area of research for aerodynamic design at low Reynolds numbers.

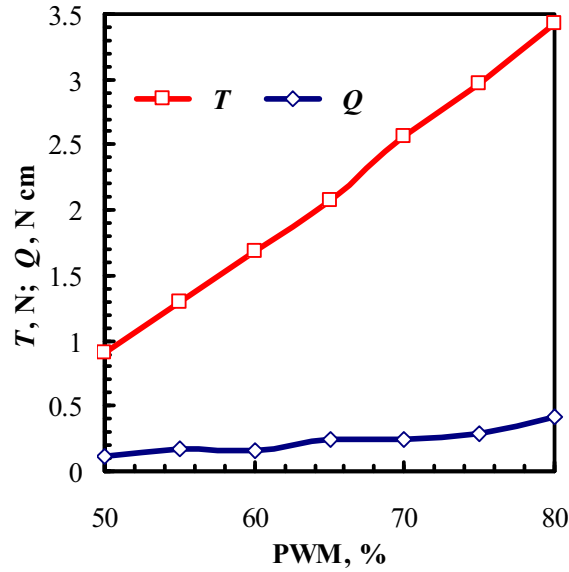


Fig. 4 Variation of thrust and torque with PWM (pulse width modulation).

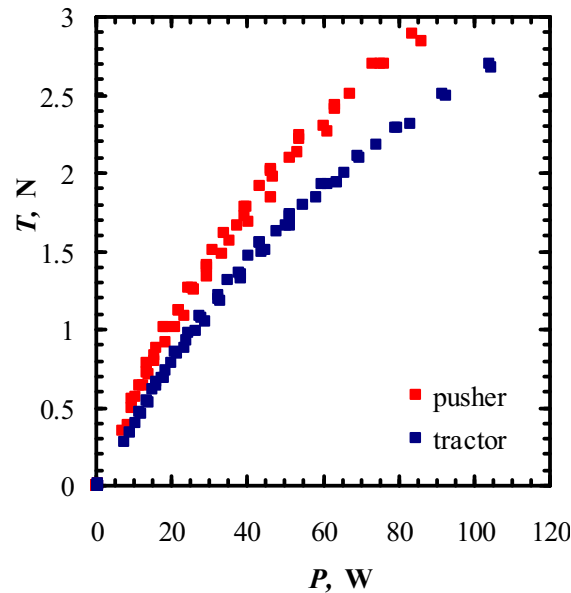


Fig. 5 Thrust of propulsion system as a function of input power.

B. Slipstream Velocity Profiles

A hot-wire system was utilized for measuring air velocity profiles in a slipstream behind the propellers. While a propulsion system was still sitting on the motor testing bench, the hot-wire probe was mounted on its top, allowing simultaneous measurements of air velocity and thrust, power input, voltage, etc. The testing was conducted at constant voltage of 8.5 V and the PWM was set to hold the thrust constant. However, in the course of the tests, a 3-5 % drift of the thrust has been observed and PWM was manually adjusted to the desired thrust.

The measurements were conducted at four sections located at distances, $s = 35, 70, 130,$ and -70 mm (Fig. 1), respectively, with the first three sections referring to the pusher arrangement, while the last section refers to the tractor. For each section, the air velocity component in the s -direction was measured at points along the z -coordinate distant from the motor-propeller axis from 0 to a maximum distance $R_m = 85$ mm, with a step of 1 mm. The propeller's radius R corresponds to $z = 75$ mm.

Air velocity distribution in the pusher propeller slipstream can be seen in Fig. 6 for two values of thrust: $T = 1.47$ N and $T = 2.45$ N. The plots exhibit a single-hump shape, with the maximum of velocity near the point $z = 0.5R$. With z increases beyond the propeller radius, the velocity asymptotically approaches zero. The local decrease of the air velocity (by about 15%) closer to the axis of rotation may be caused by the propeller's hub and the interference of the propellers with the motors. The fluctuations in velocities in terms of a standard deviation were determined and error bars plotted in Fig. 6. They are indicative of non-stationary, pulsating flow behind the propellers. The increase in size of the error bar illustrates the presence of vortices in the area near the propeller tips. Also, larger pulsations are noticed for higher thrust force.

Air velocity profiles in Fig. 7 are shown for three sections at the same thrust force. This figure shows the change in the profile: the farther they are from the propeller, the more uniform they become.

Figure 8 illustrates velocity profiles at sections placed at the same distance, $|s| = 70$ mm, from the propeller in the pusher and tractor arrangements. In fact, for the tractor arrangement, the velocity is measured right behind the aft motor. The lower average velocity and significant decrease of velocity in the core of the slipstream found in tractor arrangement are mostly due to the parasite drag caused by the motors and to some degree by the motor mount. These results also explain the overall decrease of the thrust force for the tractor arrangement in comparison with the pusher one, as evident from Fig. 5.

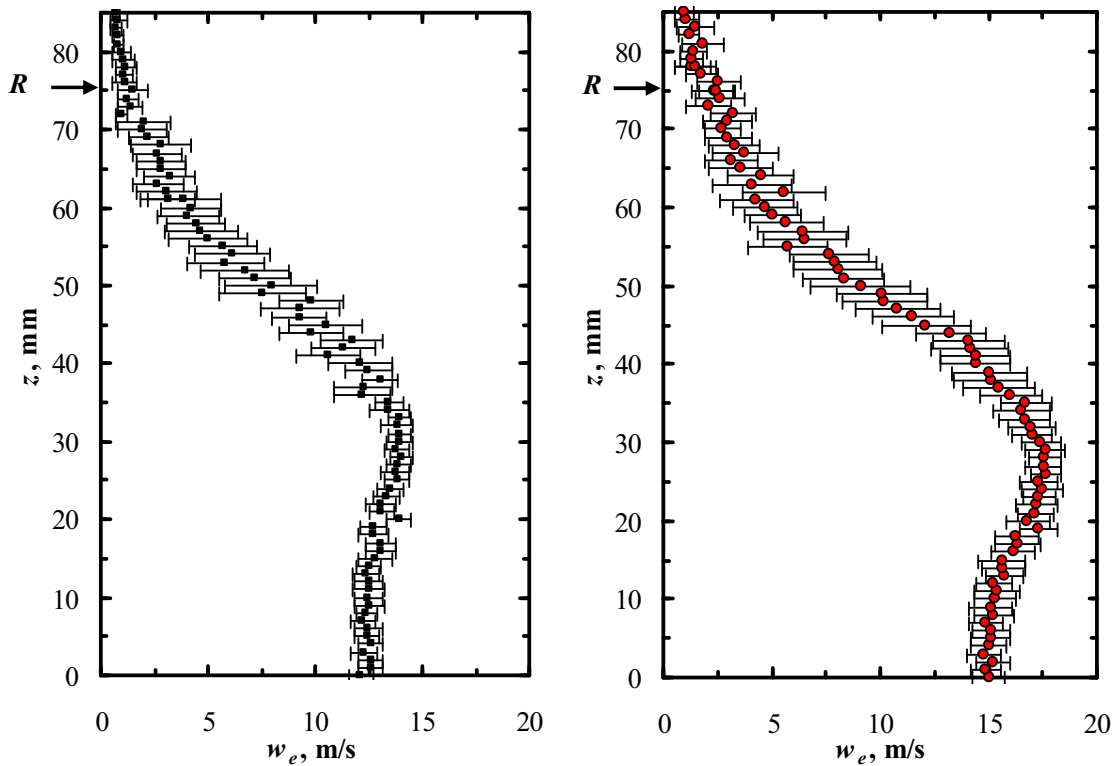


Fig. 6 Experimental velocity profiles at section $s = 130$ mm at $T = 1.47$ N (left) and $T = 2.45$ N (right) for a pusher arrangement.

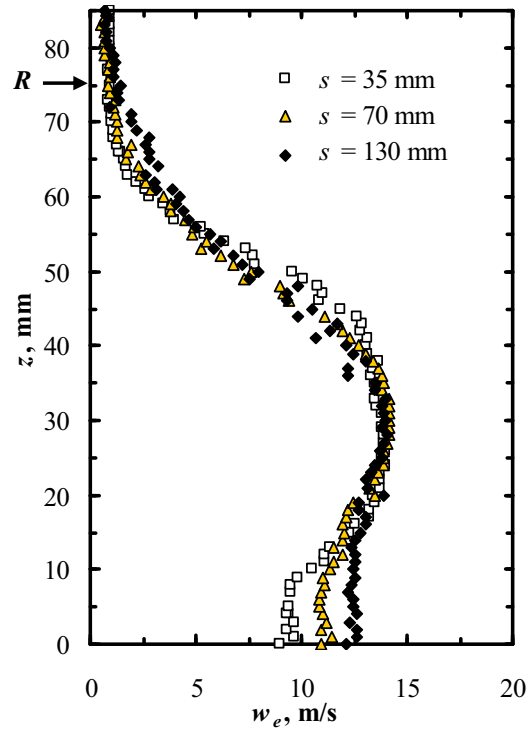


Fig. 7 Comparison of air velocity profiles for three sections in a pusher at $T = 1.47$ N.

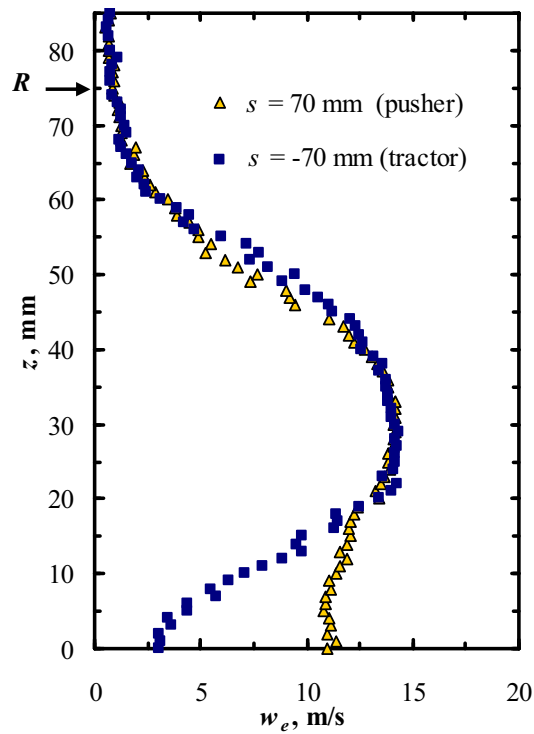


Fig. 8 Pusher vs tractor comparisons for air velocity profiles at $s = 70$ mm and -70 mm, $T = 1.47$ N.

Now, utilizing measured air velocity data, the values of thrust and induced power can be determined. Consider a cylindrical control volume around the propeller. It is assumed to be very large so that the transport of

mass and momentum through its walls is negligible, except through the side circular wall of radius $R_m = 85$ mm (of area, S_s) placed in the propeller slipstream at a distance s from the propeller. Applying the momentum and energy theorems, the static thrust is found from

$$T_s = \rho \int_{S_s} V^2 dS \quad (1)$$

while the power induced into the flow is

$$P_{ind} = \frac{\rho}{2} \int_{S_s} V^3 dS \quad (2)$$

Assuming that the air velocity remains constant in the azimuthal direction, the calculations of T_s and P_{ind} were conducted by substituting hot-wire data into Eq. (1) and (2). In addition, the figure of merit, $f_M = P_{ind} / P$, was computed.

Numerical results obtained through the use of air velocity data for sections $s = 70$ mm (for pusher) and $s = -70$ mm (for tractor) are presented in Table 1 for the nominal thrust of 1.47 N. Obtained T_s values differ from the nominal by about 5%, which is a good agreement when one takes into account the drift (mentioned above) of the thrust during these tests. As expected, for the same nominal thrust, the pusher generates higher induced power and has a higher figure of merit.

Table 1. Thrust, power, and figure of merit for propulsion systems.

Propeller Arrangement	T_s (N)	P (W)	P_{ind} (W)	f_M
Pusher	1.43	42.5	8.62	0.20
Tractor	1.55	45.0	8.20	0.18

The obtained results will be used here for verification of the propeller momentum theory for slipstream velocity predictions. By following derivations from Ref. 1, the propeller-induced velocity at the distance s from the propeller disk is given by

$$w(s) = 0.5 \left[\sqrt{V_0^2 + \frac{2T}{\rho\pi R^2} \left(1 + \frac{s/R}{\sqrt{1+(s/R)^2}} \right)} - V_0 \right] \quad (3)$$

where V_0 is a free stream velocity in front of the propeller. The radius of the stream tube induced by the propeller, r , can be found from the continuity equation

$$w(s)r^2 = w(0)R^2 \quad (4)$$

The velocity and the radius of the stream tube were calculated for the section $s = 70$ mm for two values of the static thrust. The numerical results obtained with the help of Eq. (3) are shown in Fig. 9, together with experimental data, w_e . Overall, their matching is good and, therefore, the propeller momentum theory can be recommended for air velocity predictions to be used in the aerodynamic analysis and sizing of the wing, fuselage, and control surfaces of VTOL MAVs.

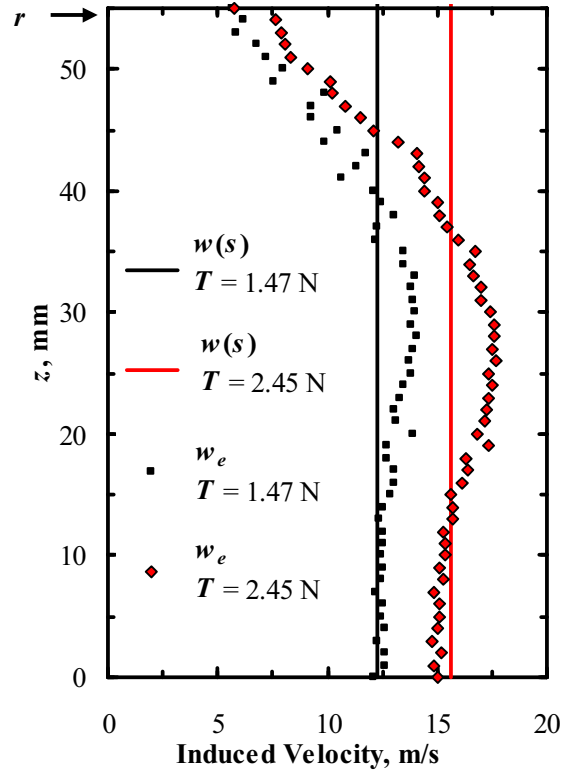


Fig. 9 Comparison of experimental results against propeller momentum theory at $s = 70$ mm.

IV. Wind Tunnel Testing

A. Wing Only Tests

Experimental measurements in wind tunnels at low Reynolds numbers become difficult because aerodynamic forces are small at low angles of attack, requiring high accuracy and sensitivity of measuring facilities. For these reasons, the validation of available aerodynamic data for wings used in the current designs is an important task itself in the development of a reliable database on MAVs.

A series of wind tunnel tests was conducted on wind tunnel models of the Zimmerman wing with 3 and 9 % camber.¹⁸ These tests were done without a motor or fuselage in order to determine the exact role that camber plays in the aerodynamics of the vehicles. In the present study, the same 3% model that was previously tested in the University of Arizona wind tunnel¹⁸ was tested in SUPAERO wind tunnel.

The tests were conducted for two values of the Reynolds numbers, 5×10^4 and 10^5 , and the results are presented in Figs. 10 and 11 for the lift and drag coefficients, respectively. It can be seen from the plots that lift coefficients are in reasonable agreement for both high and low angles of attack. For the drag coefficients, there is a reasonable agreement of the results at the moderate angles of attack, which becomes worse when α approaches angles corresponding to the maximum lift coefficient.

The zero-lift drag coefficient, C_{D_0} , is especially interesting in designing MAVs for hovering and vertical flight conditions. For the Reynolds number 10^5 , the C_{D_0} coefficient obtained in SUPAERO is 0.025, which is higher than the value of 0.02 from the UA tests. Note that for very small α , the magnitude of the measured drag becomes smaller and it has increased scatter for both testing facilities.

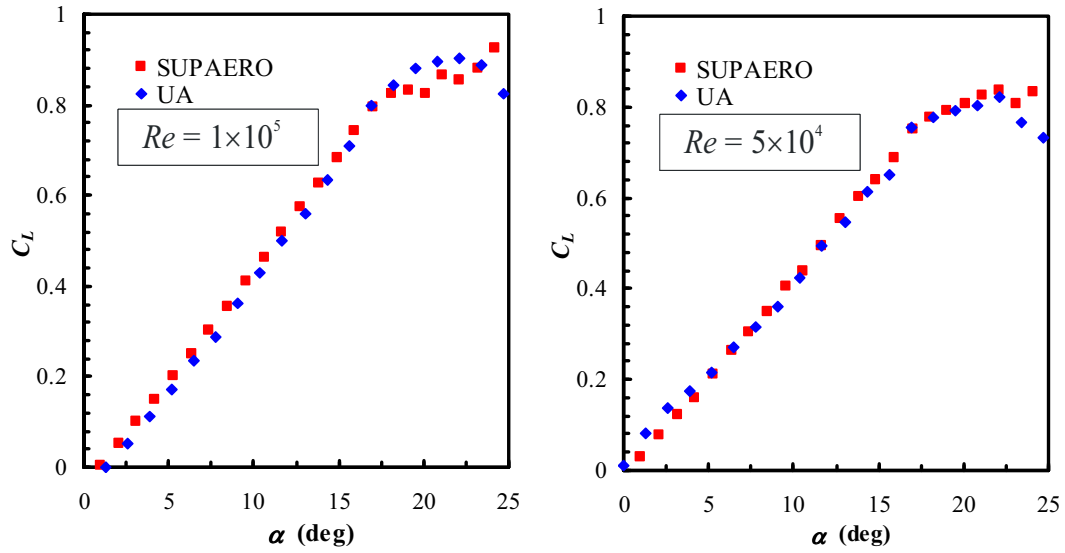


Fig. 10 Lift coefficient variation with angle of attack.

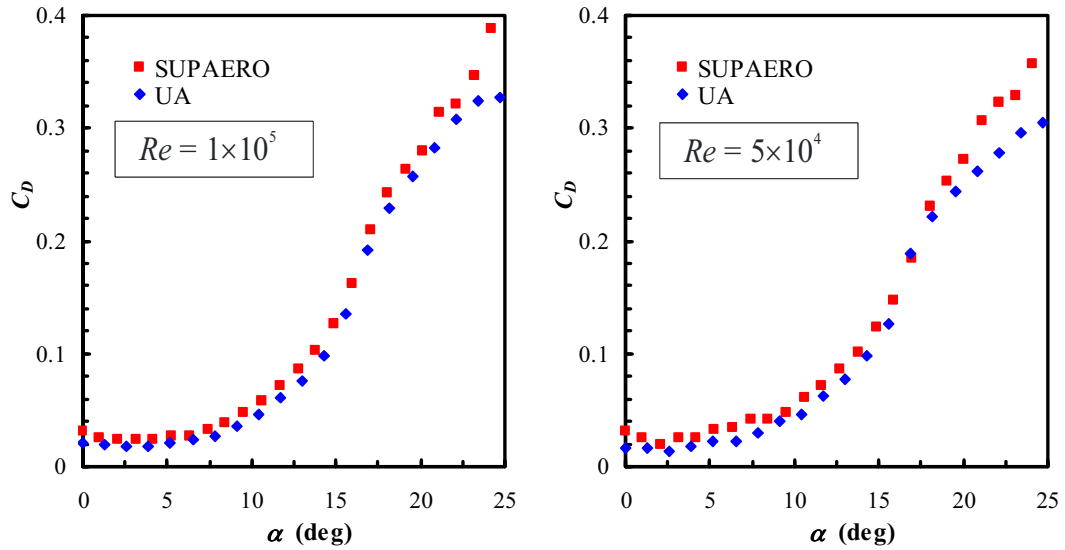


Fig. 11 Drag coefficient variation with angle of attack.

B. Motor Tests in Wind Tunnel

The contra-rotating propulsion system in a tractor arrangement was mounted to the top of the struts in the SUPAERO wind tunnel test section, and an electrical connection was established between the motor and a power supply located outside of the wind tunnel. With the power set to on and the motor running, the tunnel flow was started and thrust measurements were taken at tunnel velocities ranging from 0 to 15 m/s. The tests were conducted with 11 V supplied to the motors and with PWM varying from 55 to 70 %, so an accurate model of the thrust behavior of the propulsion was obtained. A difference between the test-bench and wind tunnel static thrust data was noticed that can be attributed to the different drags of the struts on the test-bench and in the wind tunnel.

The experimental results are presented in Fig. 12 for PWM = 55, 60, 65, and 70 %, and, as expected, the thrust decreases as free stream velocity increases.

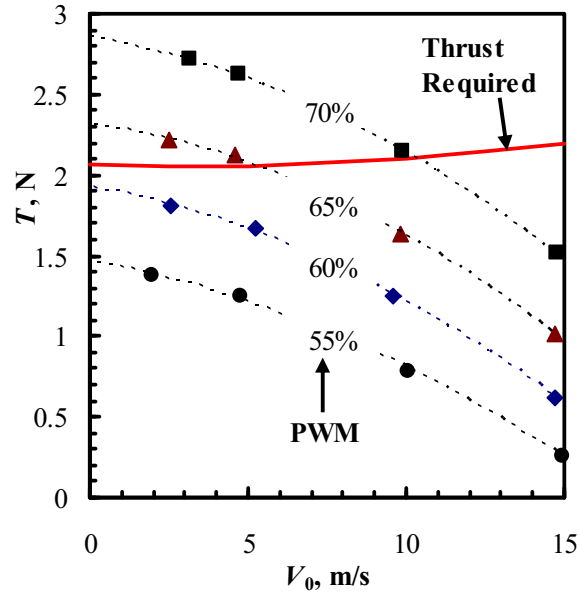


Fig. 12 Thrust available and required variations with free stream speed (symbols – experimental data points, dashed lines – quadratic approximations).

C. Determination of Wing Drag due to Free Stream and Propeller Slipstream

Hover and vertical flight efficiency is one of the single-most important qualities that VTOL MAVs must exhibit. It affects the maximum required thrust and power and determines the endurance for loitering over a target area. This part of the study will focus on the determination of drag forces at near-zero angles of attack in the presence of both free stream flow and propeller-induced flow.

This series of tests was conducted in the SUPAERO wind tunnel. The wind tunnel model shown in Fig. 3 consists of the contra-rotating propulsion and Zimmerman wing connected through a common mount fixture. The motor was installed such that the thrust line is collinear with the root chord line.

The motor was set at 11 V and PWM varied from 55 to 70%. The free stream velocity, V_0 , ranges from 0 to 15 m/sec. For a given combination of PWM and V_0 , the wind tunnel balance measures a total force, F_{total} , which is the sum of the thrust force generated by a propeller and the drag force on the wing. This force corresponds to a zero-lift angle of attack. From the motor tests described in the previous section, the amount of thrust, T , produced at each free stream velocity, V_0 , is known. The drag on the wing, D_0 , is generated from two mixing airflows: free stream and propeller slipstream. Since the motor and wing were mounted on the same fixture as in the motor only tests, the drag force can be determined as $D_0 = |F_{total} - T|$ and is presented in Fig. 13. For clarification, the total force, F_{total} , is smaller in magnitude than the propulsive thrust, T , and also because of the test procedure, the zero-lift drag force D_0 has no fixture or strut effects on it.

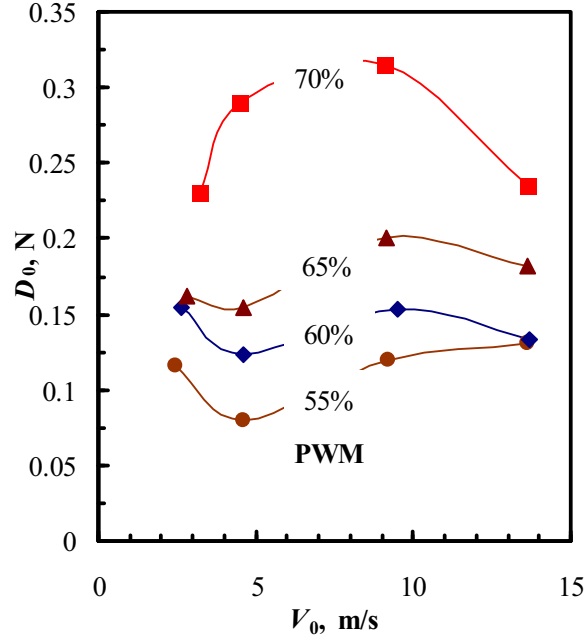


Fig. 13 Drag on the wing due to propeller slipstream and free stream.

Consider the air flow over the wing. We introduce a simplified model for the flow similar to the one used in the classical propeller momentum theory.¹ The free stream V_0 enters the propeller and wing, Fig. 14. Assume that a cylindrical stream tube is formed behind the propeller of a diameter equal to the propeller's diameter, $2R$. The second assumption is that velocity induced by a propeller is constant along the stream tube and is equal in magnitude to its ultimate value derived in the momentum theory, which is

$$w_{ult} = w(s = \infty) = \sqrt{V_0^2 + \frac{2T}{\rho\pi R^2}} - V_0 \quad (5)$$

and the velocity behind the propeller disk is a sum

$$V_0 + w_{ult} = \sqrt{V_0^2 + \frac{2T}{\rho\pi R^2}} \quad (6)$$

The zero-lift drag produced by the wing body can be presented as

$$D_0 = 0.5\rho C_{D_0} \left[S_0 (V_0 + w_{ult})^2 + (S_0 - S_p) V_0^2 \right] \quad (7)$$

where S_p is the area of a part of the wing covered by the propeller slipstream and is shown in Fig. 14. Through division, we arrive at the zero-lift drag coefficient in the presence of a free stream and slipstream

$$C_{D_0} = \frac{D_0}{0.5\rho \left[S_0 (V_0 + w_{ult})^2 + (S_0 - S_p) V_0^2 \right]} \quad (8)$$

This formula is valid also for either propeller-induced velocity or free stream velocity to be zero.

Using obtained experimental data for drag force, the drag coefficients C_{D_0} were computed from Eq. (8) as a function of the ultimate induced velocity, w_{ult} , computed by Eq. (5) and the results are presented in Fig. 15.

They clearly demonstrate that the slipstream behind the propeller has a profound negative effect on the drag of the wing.

For a low power and low w_{ult} conditions, the wing drag coefficient approaches the value for laminar flow (0.02-0.025) obtained for the wing-only test. The drag coefficient increases by about three times, with induced speed increasing from 0 to 15 m/sec. This result indicates the change of transition mechanism in the boundary layer from a laminar to turbulent state, which deserves further study.

Although the data are scattered, the correlation between drag coefficient and induced velocity is meaningful and can be approximated by the linear equation

$$C_{D_0} = 0.0305 + 0.0024w_{ult} \quad (9)$$

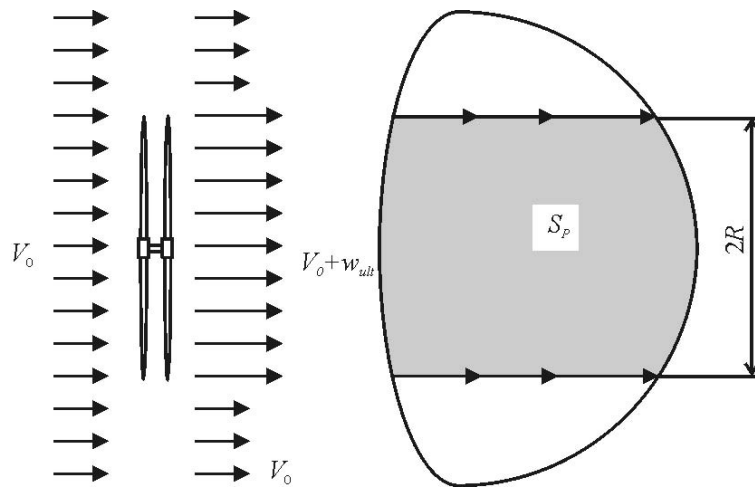


Fig. 14 Model of flow velocity over the wing.

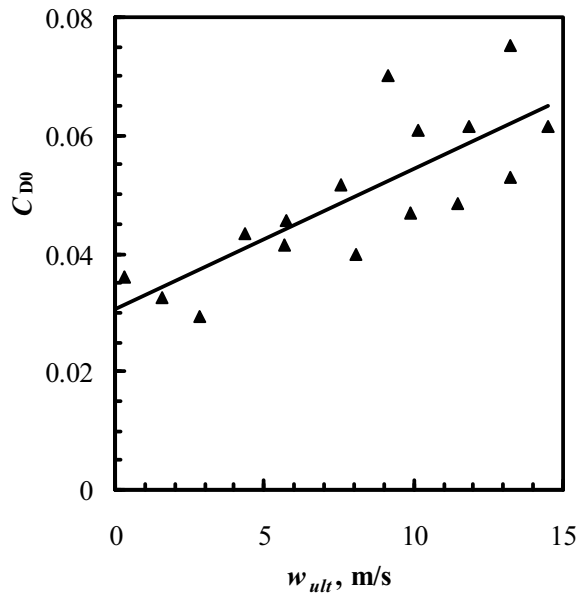


Fig. 15 Zero-lift drag coefficient variation with ultimate induced velocity.

V. Designing VTOL MAV Prototype

The obtained results can be used for designing VTOL MAVs with vertical flight requirements. Even though this procedure gives only one design point, it is an utmost important one for the selection of propulsion system and power source. For the steady vertical flight of the aircraft with a take-off weight of W , the balance of forces in a vertical direction can be written as

$$T - W - D_0 = 0 \quad (10)$$

By combining Eq. (5), (7), (9), and (10), the thrust required for the vertical flight at a speed V_0 can be found from

$$T - W + 0.5\rho \left[0.0305 + 0.0024 \left(\sqrt{V_0^2 + \frac{2T}{\rho\pi R^2}} - V_0 \right) \right] \left[S_0 \left(V_0^2 + \frac{2T}{\rho\pi R^2} \right) + (S_0 - S_p) V_0^2 \right] = 0 \quad (11)$$

The first VTOL MAV prototype (Fig. 16) has been designed based on the propulsion system described in this paper. The aircraft is equipped with a flat plate wing of Zimmerman planform. It has a take-off weight of $W = 1.76$ N, wingspan of 30 cm, wing area of $S_0 = 335$ cm², and an area of the wing portion covered by the propeller slipstream $S_p = 210$ cm². Using these data, the thrust required to climb vertically with a rate-of-climb V_0 was obtained numerically from Eq. (11) and plotted in Fig. 12. It can be seen that with the rate-of-climb increases, the required thrust is slightly increased with a maximum of 2.3 N. From comparison of thrust available and required (Fig. 12), the thrust available from the current propulsion will provide a steady vertical flight in the range of climb-rates 0-10 m/s, with PWM in the range of 62-70%.

As can be seen from Fig. 5, about 80 W of maximum power is needed to support the flight mission characterized by the maximum required thrust of 2.3 N. To satisfy this requirement, a 3-cell lithium-polymer battery, of 740 mAh capacity, was selected as an onboard power source.

Two fins with a total area of 47 cm² provide the stabilization of the aircraft in roll and yaw. A rudder consisting of two connected sections of a total area of 30 cm² is attached to fins. Two elevons of total area 60 cm² control the vehicle in pitch and yaw. Test flights were conducted with this vehicle demonstrating a hover, sustained vertical climbs, and transition to and from a level flight.



Fig. 16 VTOL MAV in flight.

VI. Conclusions

In the present study, a tilt-body, tail-sitter concept for VTOL MAVs was analyzed and a novel design was proposed based on the contra-rotating propeller-motor electric propulsion system. As evident from the discussion, this design represents a workable solution for the reduction or elimination of the negative effects of other concepts.

The evaluation of the propulsion was conducted for two propeller arrangements: pusher and tractor. Static thrust measurements, as well as RPM, power, and torque, were conducted on a motor testing bench. A small loss of thrust in the contra-rotating system was found compared to a single propeller-motor. The maximum torque for the contra-rotating system was about 10 times lower than a torque measured on a single propeller-motor system. The pusher arrangement of the propeller generates 20-23% more thrust force than the tractor for the same inputted power. In the tractor configuration, the motor is placed right behind the propellers, creating a significant parasite drag. Hence, the shape optimization of a motor mount and fuselage is another important area of research for aerodynamic design at low Reynolds numbers.

A hot-wire system was utilized for measuring air velocity profiles in a slipstream behind propellers. The fluctuations in velocities in terms of a standard deviation were determined. They are indicative of non-stationary, pulsating flow behind the propellers. For the tractor arrangement, lower average velocity and a significant decrease of velocity in the slipstream core are mostly due to the parasite drag caused by the motors' placement right behind the propellers. These results also explain the overall decrease of a thrust force for the tractor arrangement in comparison with the pusher one.

In the present study, the same 3% Zimmerman wing that was previously tested in the University of Arizona wind tunnel was tested in the SUPAERO wind tunnel. The results for the lift and drag coefficients are in reasonable agreement for both high and low angles of attack.

The aerodynamics of a wing-propeller combination was studied through wind tunnel measurements. Results clearly demonstrate that for a given range of propeller thrust, the slipstream behind the propeller has a profound negative effect on the drag of the wing for zero-lift angles of attack. The drag on the wing is generated from two mixing airflows: free stream and propeller slipstream. A simplified model for the flow similar to the one used in the classical propeller momentum theory is introduced in the present study, and a formula for the drag coefficient for the wing in the presence of a free stream and slipstream is derived.

Using obtained experimental data for drag forces, the zero-lift drag coefficients were computed as a function of the ultimate induced velocity. The drag coefficient increases three times, with induced speed increasing from 0 to 15 m/sec. This result indicates the change of transition mechanism in the boundary layer from a laminar to a turbulent state, which deserves further study.

The results obtained in the present study were realized in a design of a VTOL MAV prototype that was successfully flight tested.

Acknowledgments

This project represents collaborative efforts of the University of Arizona and SUPAERO towards the development of VTOL MAV technologies. It was sponsored by grants from the AFRL, Eglin AFB (Program Manager Dr. Gregg Abate), to the University of Arizona and by EOARD, London (Program Manager Dr. Surya Surampudi), to the SUPAERO. The authors also would like to thank the other members of the Micro Air Vehicle Project at both universities for their contributions to this work: Bill Silin, David Addai, and Chinnapat Thipyopas. S. Shkarayev would like to thank the SUPAERO team for their support of research on VTOL MAVs during his visiting appointment there.

References

- ¹McCormick, B. W. Jr., *Aerodynamics of V/STOL Flight*, Dover Publications, Inc., Mineola, NY, 1999.
- ²Kohlman, D., *Introduction to V/STOL Airplanes*, Iowa State University Press, Ames, IA, 1981.
- ³Krashanitsa, R., Platanitis, G., Silin, D., and Shkarayev, S., "Autopilot Integration into Micro Air Vehicles," Chapter 3, *Introduction to the Design of Fixed-Wing Micro Aerial Vehicles*, edited by T. J. Mueller, J. C. Kellogg, P. G. Ifju, and S. V. Shkarayev, AIAA, Reston, VA, 2007, pp. 109-149.
- ⁴Bataille, B., Poinot, D., Thipyopas, C., and Moschetta, J.M., "Fixed-Wing Micro Air Vehicles with Hovering Capabilities," NATO RTO meeting, AVT-146, Symposium on "Platform Innovations and System Integration for Unmanned Air, Land and Sea Vehicles," Florence, Italy, May 14-17, 2007.
- ⁵Prandtl, L., "Mutual Influence of Wings and Propeller," NACA TN 74, Extract from *The First Report of the Gottingen Aerodynamic Laboratory*, Chapter IV, Sec. 6, December, 1921.
- ⁶Hood, M. J., and Gaydos, M. E., "Effects of Propellers and Vibration on the Extent of Laminar Flow on the NACA 27-212 Airfoil," NACA ACR (WR L-784), 1939.

⁷Elsaadawy, E. A., and Britcher, C. P. "Effect of Propeller Slipstream on Heat-Exchanger Installations at Low Reynolds Number," *J. Aircraft*, Vol. 40, 2003, pp. 751-758.

⁸Miley, S. J., Howard, R. M., and Holmes, B. J., "Wing Laminar Boundary Layer in the Presence of a Propeller Slipstream," *J. Aircraft*, Vol. 25, 1988, pp. 606-611.

⁹Hoerner, S. F., *Fluid-Dynamic Drag*, Hoerner Fluid Dynamics, Bakersfield, CA, 1965.

¹⁰Micro Air Vehicle Design Papers, 6th International MAV Competition, Brigham Young University, Provo, UT, April 2002.

¹¹Micro Air Vehicle Design Papers, 7th International MAV Competition, University of Florida, Gainesville, FL, April 2003.

¹²Micro Air Vehicle Design Papers, 8th international MAV Competition, The University of Arizona, Tucson, AZ, April 2004.

¹³Mueller, T. J., Torres, G. E., Srull, D. W., Elements of Aerodynamics, Propulsion, and Design, Chapter 2, *Introduction to the Design of Fixed-Wing Micro Aerial Vehicles*, Edited by J. Mueller, J. C. Kellogg, P. G. Ifju, and S. V. Shkarayev, AIAA, Reston, VA, 2006, pp. 39-107.

¹⁴Null, W., Noseck, A., and Shkarayev, S., "Effects of Propulsive-Induced Flow on the Aerodynamics of Micro Air Vehicles," 23rd AIAA Applied Aerodynamics Conference, AIAA 2005-4626, Toronto, Canada, 2005.

¹⁵Moschetta J. M. and Thipyopas C., "Aerodynamic Performance of a Biplane Micro Air Vehicle," *Journal of Aircraft*, Vol. 44, 2007, pp. 291-299.

¹⁶MP Jet Electromotor AC 22/4-60 D, MP Jet, Rudolfovska 87, P.O. BOX 100, CZ -370 21 C. Budejovice, Czech Republic, 2007.

¹⁷Null, W. and Shkarayev, S., "Effect of Camber on the Aerodynamics of Adaptive Wing Micro Air Vehicles," *J. Aircraft*, Vol. 42, 2005, pp. 1537-1542.

¹⁸Aki, M., Waszak, M., and Shkarayev, S., "Development of Micro Air Vehicles with In-Flight Adaptive Wing," Chapter 6, *Introduction to the Design of Fixed-Wing Micro Aerial Vehicles*, Edited by J. Mueller, J. C. Kellogg, P. G. Ifju, and S. V. Shkarayev, AIAA, Reston, VA, 2006, pp. 241-275.

¹⁹Kline, S. J., and McClintock, F. A., "Describing Uncertainties in Single-Sample Experiments," *Mech Eng*, Vol. 75, No.1, 1953, pp. 3-8.

²⁰Barlow, J. B., Rae, W. H., Jr., and Pope, A., *Low-Speed Wind Tunnel Testing*, 3rd Ed., Wiley, New York, 1999.

Appendix 2

On Fixed-Wing Micro-Air Vehicles with Hovering Capabilities

This page intentionally left blank

On Fixed-Wing Micro-Air Vehicles with Hovering Capabilities

Jean-Marc Moschetta^{*}, Boris Bataille[†], Chinnapat Thipyopas[‡]
Institut Supérieur de l'Aéronautique et de l'Espace, Université de Toulouse, France

and

Sergey Shkarayev[§]
Department of Aerospace and Mechanical Engineering, University of Arizona, Tucson, Arizona

The present paper investigates the possibility to improve the aerodynamic performance of a fixed-wing micro air vehicle (MAV) concept so as to simultaneously allow high cruise speed for covertness and hovering flight for stable image transmission. Two fixed-wing MAV configurations were tested and compared: a tilt-wing concept powered by two non-coaxial counter-rotating propellers and a tilt-body concept based on a coaxial rotor. The different configurations were separately analyzed based on wind tunnel experiments. The tilt-wing concept, although superior to the tilt-rotor concept, does not provide a significant benefit over an equivalent tilt-body MAV configuration. Finally, two tilt-body coaxial prototypes were designed and successfully flight tested to demonstrate the capability of fixed-wing MAV configurations to lift off, sustain hover flight and perform transition between forward and hover flight. Special attention was paid to the coaxial tail-sitter concept for which the propellers slipstream guarantees aerodynamic efficiency over the whole flight envelope. Side-by-side comparison of a mini- and a micro-sized coaxial tail-sitter model was carried out and discussed.

Nomenclature

α	=	angle of attack ($^{\circ}$)
A	=	wing aspect ratio
AC	=	aerodynamic center location (cm)
c	=	chord
C_D	=	drag coefficient
C_F	=	mean friction drag coefficient
C_L	=	lift coefficient
$C_{m(AC)}$	=	pitching moment coefficient at the aerodynamic center
D	=	drag force (N)
D_{rotor}	=	rotor diameter (mm)
DL	=	rotor disk loading (N/m^2)
f_M	=	rotor figure of merit
k	=	coefficient of induced drag: $C_D = C_{D0} + k C_L^2$
L	=	lift force (N)

^{*}Professor, Department of Aerodynamics, Energetics and Propulsion, ISAE BP54032, 31055 Toulouse Cedex 4, France, jean-marc.moschetta@isae.fr, member AIAA.

[†]PhD candidate, Department of Aerodynamics, Energetics and Propulsion, ISAE BP54032, 31055 Toulouse Cedex 4, France, boris.bataille@isae.fr.

[‡]Research assistant, Department of Aerodynamics, Energetics and Propulsion, ISAE BP54032, 31055 Toulouse Cedex 4, France, chinnapat.thipyopas@isae.fr.

[§]Associate Professor, Department of Aerospace and Mechanical Engineering, The University of Arizona, PO Box 210119, Tucson AZ 85721-00119, svs@u.arizona.edu.

P_{ind}	=	rotor induced power (Watts)
PL	=	rotor power loading (Watts/kg)
q_0	=	free stream dynamic pressure (N/m ²)
S	=	wing surface (m ²)
T	=	thrust force (N)
W	=	weight (N)

I. Introduction

RECENT developments of micro air vehicle systems (MAVS) have revealed that a new generation of multiple-tasking MAVS is coming up¹. The classical distinction between forward-flight airframe and VTOL platform is now being reconsidered in view of giving rise to vehicles capable of both dashing to escape enemy fire and slowly loitering over a target. Fixed-wing micro air vehicles are considered to be very attractive for outdoor surveillance missions since they usually offer better payload and endurance capabilities than rotorcraft or flapping-wing vehicles of equal size. They are generally less challenging to control than rotorcraft in outdoor environment and allow for a dash capability to escape enemy attention. On the other hand, they usually fail miserably to perform vertical take-off and landing (VTOL) and sustain stable hover flight which proves to be crucial for urban surveillance missions including building intrusion. The present paper investigates the possibility to improve the aerodynamic performance of a fixed-wing MAV concept so as to allow for hovering capabilities and still maintain high cruise speed for covertness.

In a typical MAV recon mission, both capabilities are needed since long-endurance to reach a remote area is as important as the capability of sustaining hover flight over the target. Furthermore, the efficient use of MAVS in an urban environment supposes a threefold flight plan which includes both outdoor flights and indoor flights. During a first outdoor phase, the MAV will typically endeavor to select and identify a place of interest: a street, a roof or a building facade. The MAV should then be able to perform rapid translations over a large zone and loiter over the selected area during a certain period of time. That first part of the mission requires long-endurance performances and the ability to flight against windy conditions, promoting classical fixed-wing, low-drag configurations. During a second phase of the mission, when the area of interest has been selected, the MAV should be in a position to reduce its speed at a minimum level so as to transmit clear images back to the ground station. It is also required to be able to maneuver through narrow streets and withstand wind gusts. The second phase of the mission clearly requires high maximum lift coefficients and the capability to transition from horizontal to vertical flight so as to perform high angle of attack maneuvers and near prop-hang attitudes. At that point, stationary flight is not strictly needed to capture clear images, provided that the MAV is equipped with an efficient gyro-stabilized camera system. Finally, during a third flight phase, building intrusion can be considered through an opening such as an open window for instance. That last part of the mission is by far the most challenging part since it simultaneously involves the capability to perform a stable outdoor transition from slow flight to hover flight in a way that can authorize building

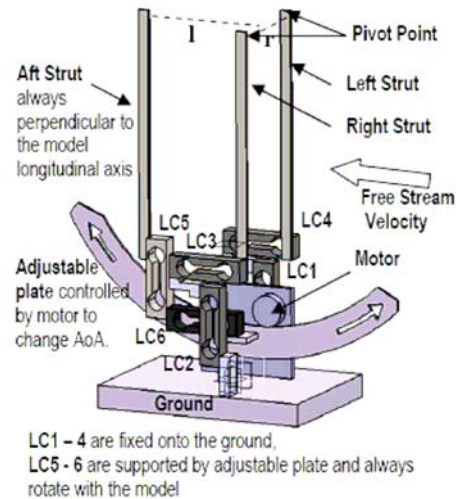


Figure 1. Low-speed wind tunnel (left) and the 5-component micro-balance (right).

configuration such as in the *TYTO* concept. In the present section, a bimotor tilt-body configuration has been compared to a tilt-wing bimotor configuration. The tilt-wing configuration has been preferred to the tilt-rotor concept in which the propellers are rotated at the wing tips while the wing and fuselage remains horizontal. Yet, for MAVs, the tilt-rotor concept is difficult to implement for at least two reasons: 1. the severe dimension constraint imposed on MAVs is not consistent with the use of propellers which extend beyond the wing tips since the outer maximum dimension would be the sum of the full wing span and a propeller diameter as in the MITE concept¹⁰, 2. the downward force induced by the rotor when perpendicular to the wing is very important on low-aspect ratio wings and dramatically degrades the thrust generated by the tilted rotors. Therefore, it has been proposed to carry out an experimental side-by-side comparison between a tilt-body bimotor MAV and a tilt-wing bimotor MAV using the same monoplane Zimmerman wing as designed at the University of Arizona¹¹.

A. Tilt-wing powered models

The Zimmerman planform wing is formed by joining two half-ellipses at the quarter-chord, with a 200-mm wing span, 136-mm root chord, and aspect ratio of 1.9 (Fig. 3). The S5010-TOP24C-REF airfoil¹¹ was utilized in designing the wing, with a maximum camber of 3% located at $0.24c$ and an inverse camber of 1% at $0.85c$. The wing geometry, generated using *SolidWorks*TM (Fig. 3, left), has been designed so that the maximum camber points follow a straight line at $0.24c$. That straight line was actually used to place the axis of rotation for the tilt-wing configuration. The outer portions of the wing could then be rotated up to 90° with respect to the central part. Ten layers of carbon fiber resin were applied so that the model has constant thickness of 2 mm, with a leading edge radius of 1 mm. The tilt-wing cutting line location was selected so as to allow sufficient fuselage volume and to reduce the downward forces induced by the propellers in upright position. Finally, a 40 mm-span was chosen for the central part which stays horizontal and carries the fuselage (Fig. 3, right).

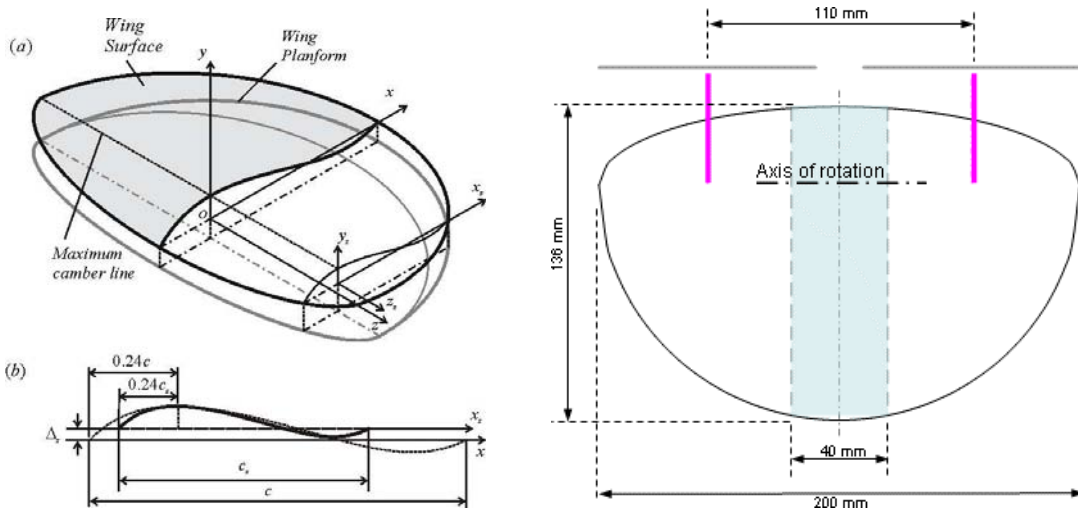


Figure 3. Schematic views of the Zimmerman wing (left) and the bimotor tilt-wing model (right).

The propulsion system consists of two 4-blade contra-rotating propellers which diameter is 92 mm. Each propeller weights 2 grams and is attached to a brushless micro-motor *LRK-13-4-15Y* which stator diameter is 13 mm. Each motor weights 5.8 grams and is regulated by a single MOS-FET RISC *YGE4-BL* speed controller, which provides the same RPM to both motors. In the present study, no differential throttle effects were investigated since the emphasis was put on the comparison between a tilt-wing and a tilt-body bimotor concept. The propulsion sets were then attached to the model through a motor rib which was glued on the windward side of the wing model at 55 mm from the root chord. Each propeller disk was located at 20 mm ahead the leading edge and the motor axis were aligned with the wing root chord. It should be noticed that the propellers were placed so that the maximum overall dimension is still 200 mm. Since the test was done in a close test section, a slipstream correction was calculated but it was found to be less than 1% of the free stream velocity.

B. Experimental procedure

The model support was connected to three struts of the external balance. The motor power was adjusted via a PWM signal (Pulse Width Modulation) ranging from 30% to 100%, and controlled from a *LabView*TM interface via the acquisition system. The thrust force (both vertical and horizontal components) and the torque were measured as a function of the angle of attack at a fixed value of the tilt angle. During each test, the electric consumption was read manually from an external DC power supplier display. The RPM was not been measured in this work. The drag of the propulsive support and the struts was carefully determined at different wind speeds and angles of attack to correct the force and moment measurements.

The Zimmerman wing used in this study was first tested in the wind tunnel without motors in order to verify the measurement system and to compare with the previous measurements done both at ISAE and the University of Arizona¹². Because previous experiments showed that there is little interaction between the model and the struts, the

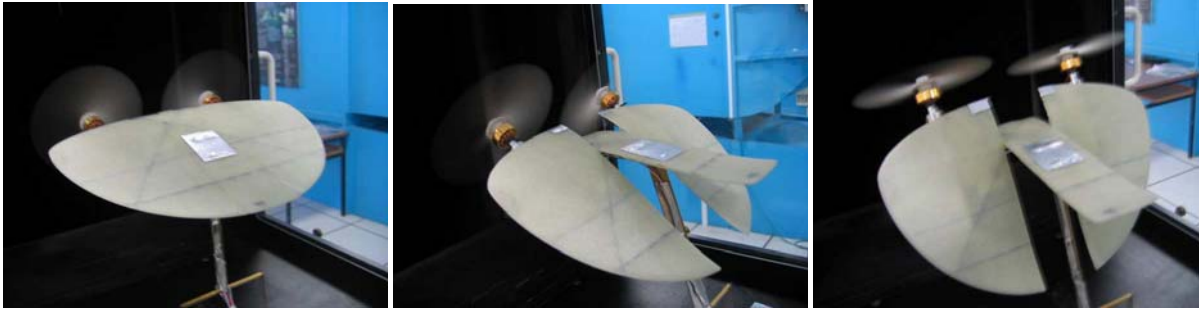


Figure 4. Experimental setup: tilt-body configuration (left), tilt-wing at 30° (center), tilt-wing at 60° (right).

struts drag was measured as function of the angle of attack and velocity and subtracted from the powered model measurements following Eq. (1).

$$F_{(model)} = F_{(model+struts)} - q_{0(model+struts)} \times S C_{F(struts)} \quad (1)$$

where $C_{F(struts)}$ was obtained from the struts-alone drag tests. Wind tunnel tests were carried out in two steps. The wing model was first measured without propellers at three different flow speeds: 5, 10 and 15 m/s. A second series of measurements was done with powered models with a constant supply voltage of 11 Volts and flow speeds ranging from 0 to 15 m/s with an interval of 2.5 m/s. For each speed, 4 different PWM percentage values were compared: 40%, 60%, 80% and 100%. The tilt-body configuration can actually be considered as a tilt-wing configuration with a tilt angle of 0°. A series of 3 tilt-wing configurations were measured with tilt angles of 30°, 60° and 90° (Fig. 4).

C. Results and discussion

The tilt-wing and tilt-body configurations were compared at different flow speeds. At each speed, the tilt-body angle of attack and the PWM signal were adjusted so that a constant lift force of 80 grams was produced with no drag force. Since the models tested had no horizontal tail or any control surface, the pitching moment could not be balanced. For the tilt-wing configuration, the wing central part was constantly aligned with the free stream direction while the outer parts of the wing were tilted. Again, the tilt angle and the PWM signal sent to the motor were adjusted so as to produce a constant lift force of 80 grams and no drag force.

The results obtained at different flight speeds in equilibrium are presented for both configurations in Fig. 5. The equilibrium tilt angle for the tilt-wing configuration, or the equilibrium angle of attack for the tilt-body configuration, are compared at different flight speeds (Fig. 5, left), ranging from hover (0 m/s) to cruise speed (15 m/s). It appears that due to the relatively small untitled wing portion, the tilt-angle distribution is almost identical to the angle of attack distribution. This suggests that the overall aerodynamic efficiency of the tilt-wing configuration is not significantly affected by the decrease of the aspect ratio associated to the tilted wing portions. On the contrary, at 5 m/s, since the aspect ratio of the tilted portions is smaller than the aspect ratio of the untitled wing, the stall angle is increased because of the vertical lift effect. Therefore, the same lift force can be obtained with the tilt-wing configuration for a tilt angle of 30° while the tilt-body configuration requires an angle of attack of 35°. The PWM signal (Fig. 5, right) is also almost identical in both tilt-body and tilt-wing configuration which indicates that the tilt-wing concept is not significantly more demanding in terms of power to sustain low-speed and hover flights. The maximum speed for both powered models is greater than 16 m/s since at that speed, both models only require 55%

of the PWM signal. However, the present powered models do not include additional sources of parasite drag such as the fuselage, antenna, servos and other equipments which might stick out. It should be noticed that both configurations use about 50% throttle to travel in the speed range of 4 to 15 m/s, which allow for the additional power necessary to climb and maneuver.

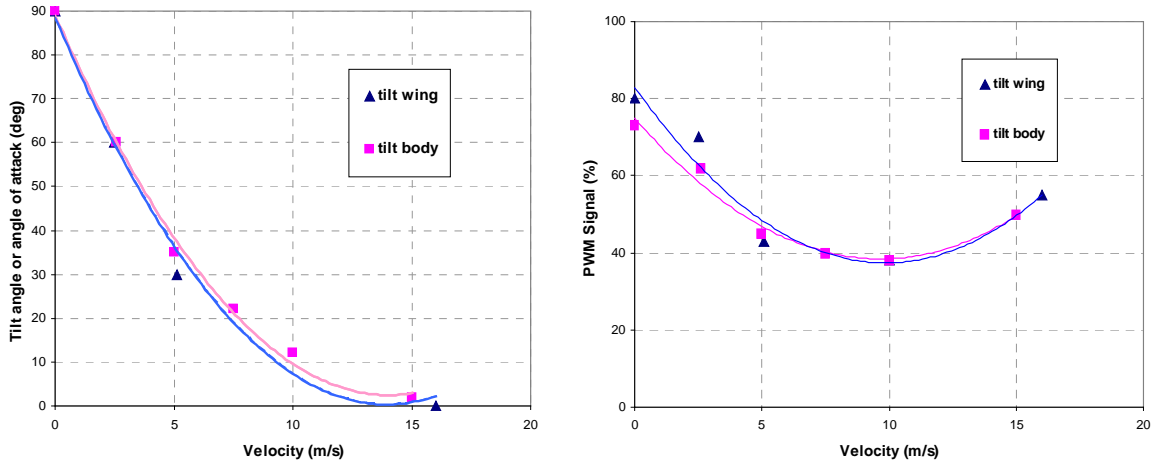


Figure 5. Tilt-wing vs. tilt-body during transition: tilt angle or angle of attack (left), PWM signal (right)

The major difference between the two concepts appears at very high angles of attack (or tilt angles) and at very low speeds, namely lower than 2 m/s, i.e. during transition flight and in hover mode. The tilt-wing configuration requires 80% of the PWM signal while the tilt-body configuration requires 73% of the PWM signal, which corresponds to an additional 4.4 watts for the tilt-wing configuration to sustain hover flight. The additional force can be interpreted as a consequence of the downward force due to the central part of the wing. The tilt-wing MAV configuration would achieve about 13% lower endurance than that of an equivalent tilt-body MAV configuration equipped with batteries of identical capacity. This last result suggests that an augmented central portion of the wing would further degrade the hovering performance of a tilt-wing configuration.

Finally, a series of tests were carried out to evaluate the pitching moment of both MAV configurations during transition when lift and drag are balanced.

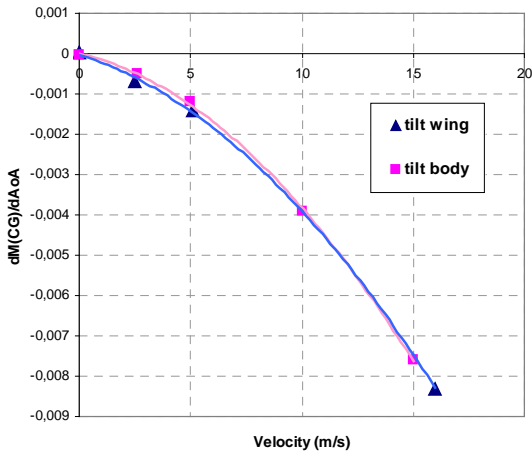


Figure 6. Pitching moment of balanced tilt-wing and tilt-body MAV configurations at different flight speeds.

The reference point to calculate the pitching moment is the point which is located ahead of the aerodynamic center with a static margin of 10% at 16 m/s. Although the center of gravity is moving when the wings are tilted, the reference point will be designated by CG in the following. It would actually coincide with the expected center of gravity of the horizontal flight. The gradient of pitching moment with respect to the angle of attack is plotted in Fig. 6 as a function of the free stream speed. Each value of that gradient is calculated from a series of measurements of the pitching moment around each balanced flight point (lift force of 80 grams and no drag force) with a range of 15 degrees around the equilibrium angle of attack or tilt angle. During transition, as the free stream speed is reduced, the propellers slipstream gradually dominates the flowfield about the wing. Therefore, the wing effective angle of attack, that is the angle between the relative wind and the wing's chord line, remains moderate and always lower than the wing stall angle. Therefore, the variation of pitching moment remains linear even at high angles and the derivation of the

pitching moment gradient is straightforward in all flight situations. Actually, a Zimmerman wing without propwash effect stalls at 20 degrees in the present free stream conditions, confirming that the effective wing angle of attack is less than 20 degrees during transition. The results presented in Fig. 6 show that for both configurations, the slope of the pitching moment at equilibrium conditions dramatically decreases when the flight speed is reduced. For the tilt-body configuration, the reduction in flight speed is associated with an increase in angle of attack while for the tilt-wing configuration, it is associated with an increase in tilt angle. In hover mode, the pitching moment slope almost vanishes which is consistent with an aerodynamic efficiency totally due to the propwash effect.

As a conclusion, it appears that the tilt-wing concept is not beneficial in terms of performances to the prospect of transition from horizontal to vertical flight with the MAV constraints. The downward force induced by the presence of a central part of the wing suggests that a tilt-body configuration is preferable for an unmanned vehicle of small size for which a tilting device would impair its payload capacity with no decisive argument in favor of a horizontal fuselage. A tilting gimbaled camera mounted on a tilt-body configuration seems preferable¹³.

IV. A tail-sitter VTOL MAV

As an alternative to the tandem-rotor pusher or tractor configuration, a coaxial tail-sitter has been considered in both the mini- and micro-UAV size range. Although other authors have recently considered to apply the tilt-body concept to the design of VTOL UAVs¹⁴⁻¹⁶, the combination of coaxial rotor and a fixed-wing tilt-body airframe has not yet been applied to the mini-UAV field. The mini-UAV *Vertigo* is a VTOL mini-UAV prototype developed at ISAE in order to demonstrate the capacity to achieve autonomous transition between hover and fast forward flight. It was designed and built at the Aircraft Design Department of ISAE based on a successful early prototype which

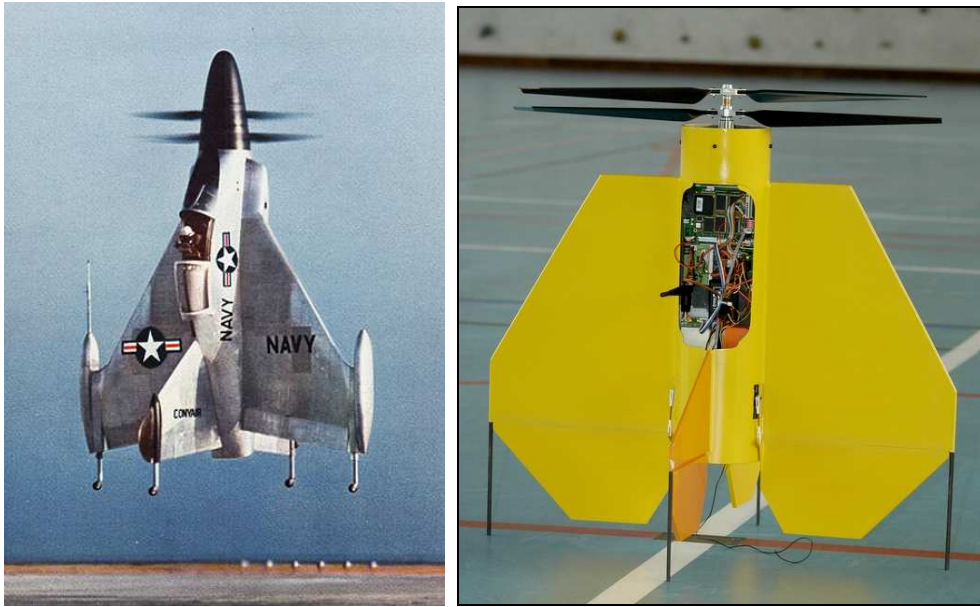


Figure 7. Full-scale Convair XFY-1 “Pogo” (left) and the mini-UAV “Vertigo” (right)

could perform transition and stable flight in RC manual mode. The source of inspiration for the *Vertigo* is the *Convair XFY-1 “Pogo”* prototype¹⁷ (Fig. 7, left*). The airframe consists of two flat plate wings which polygonal planform approximate the inverse Zimmerman wing and two vertical fins that are symmetrically placed on either side of fuselage. The wingspan is 650 mm and the aspect ratio is 1.8. The wings are made of carbon fiber and lightweight Depron foam with a constant thickness of 7 mm. A pair of two-blade coaxial contra-rotating propellers of 500-mm diameter is mounted in tractor configuration. Two large flaps are fitted on each wing to ensure enough efficiency to control the vehicle in pitch and roll when hovering. Although each propeller is powered by its own electric motor, the choice has been made to control yaw by the rudder rather than by differential throttle. Therefore,

* From <http://www.militaryimages.net/photopost/data/526/24.jpeg>

the same throttle is constantly applied to both motors. All electronic equipments are fitted into the cylindrical fuselage. The total take-off mass is 1.6 kg fully equipped and its center of gravity lies 145 mm behind the wing leading edge. More details about the autopilot architecture can be found in Ref. 18.

A. Experimental setup

Two series of tests were carried out on the *Vertigo* model. In the first series, no wind effect was considered to analyze the hovering flight. Ground effects were also investigated to better understand the take-off and landing flight phases. In the second series of tests, the *Vertigo* model was sting-mounted in the S4 wind tunnel through a 6-component balance on a piloted arm called "DEUKAPI" which is able to combine pitch, roll and yaw angles. The

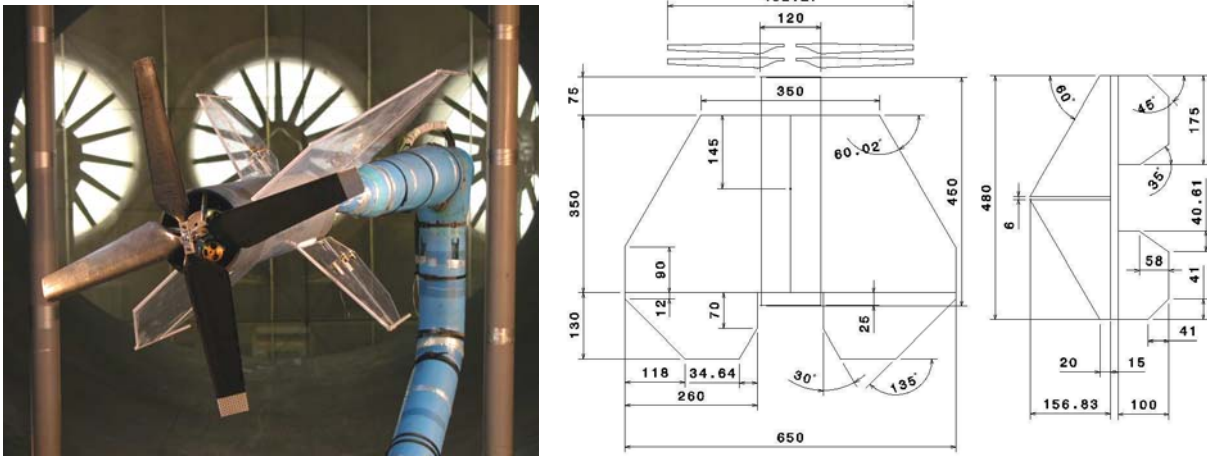


Figure 8. Wind tunnel setup for the *Vertigo* model (left), schematic views of the *Vertigo* (right)

present paper will only detail wind tunnel measurements although some tests were done in the test section without wind. Electric power was supplied with power cables running along the DEUKAPI arm and connected to a stabilized power generator. It delivered a constant voltage of 11 Volts representative of the 3-cell Lithium battery powering the *Vertigo*. Special care was taken to ensure that no magnetic interaction between power cables and load cells would affect the measurements. Also, special attention was paid to the spurious mechanical tensions that might impact forces measurements through the power cables. Figure 8 (left) illustrates the *Vertigo* model mounted on the DEUKAPI arm in the test section of S4 wind tunnel. Also a schematic view of the wind tunnel model is given in Fig. 8 (right). In the following, the choice has been made to use 500 mm as a reference length and a reference area corresponding to the 500 mm-diameter propeller disk as it is both representative of the propeller disk and the wing dimensions. However it will lead to aerodynamic coefficients 22% bigger than if they were obtained by using the actual wing area which is equal to 0.24 m².

B. Wing alone tests

Preliminary tests have consisted of a wing alone configuration. This was achieved by removing propellers from the propulsion unit. Both lateral and longitudinal tests were run for several speeds: 5, 10, 15 and 20 m/s. Then flap efficiency was assessed for flight speeds of 10 and 20 m/s. Lift at zero degree angle of attack is zero as expected. The wing lift coefficient reaches its maximum value at 1.1 and from then gradually decreases of lift until 90° where the lift is zero (Fig. 9). A progressive separation starts at 15° where the lift slope begins to decrease. A sharp stall

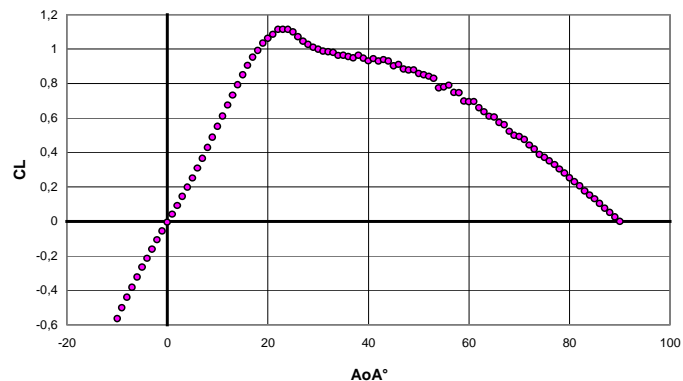


Figure 9. *Vertigo* lift coefficient from -10° to 90° angle of attack

occurs at 23° angle of attack where the lift slope sign becomes negative. Yet, it should be noticed that the lift coefficient remains greater than 0.8 up to 55° angle of attack. In the low angle of attack portion of the diagram, the lift slope shows noticeable non-linearity typical of small aspect-ratio wings and especially delta wings. This non-linearity attributed to vertical structures can be taken into account using Polhamus formulation¹⁹ of the lift coefficient:

$$C_L = K_p \sin \alpha \cos^2 \alpha + K_v \cos \alpha \sin^2 \alpha \quad (1)$$

where K_p depends on the aspect ratio, sweep angle and leading edge shape of the wing. It represents the potential lift contribution. Coefficient K_v is a constant factor usually equal to π which represents the vortex lift contribution. With $K_p = 2.6$ and $K_v = 1.25$, Eq. (1) is in good agreement with the experimental data up to 14°, confirming the existence of vortical lift on the leeward side of the wing.

A fairly high value of the minimum drag coefficient $CD_0 = 0.054$, reached at 0° angle of attack can be mainly attributed to the base drag and the nose drag of the cylindrical unstreamlined fuselage. The lift-to-drag ratio reaches its maximum value at 8° angle of attack with a moderate lift-to-drag value of 4.

The pitching moment coefficient at the expected center of gravity CG, located 145mm behind the wing leading edge, has been measured over the range -10° to 90° angle of attack (Fig. 10). Three parts can be pointed out on this curve: the first part that goes from -5° to +5° indicates a linear behavior for low angles of attack where the aerodynamic center stands ahead of the CG. This suggests that the center of gravity should be slightly shifted upstream in order to remove instability around 0°. The second part starts at 10° when the slope becomes negative, due to the onset of separation on the leeward side of the wing. Note that the pitching moment vanishes with a stable slope around 15°, that is 8° before the wing stall angle (23°). This suggests that the wing stall is dominated by vortical lift that shifts the center of lift further downstream. The third part begins right after the stall angle with a pitching moment slope which tends to decrease and to become constant up to 90° angle of attack.

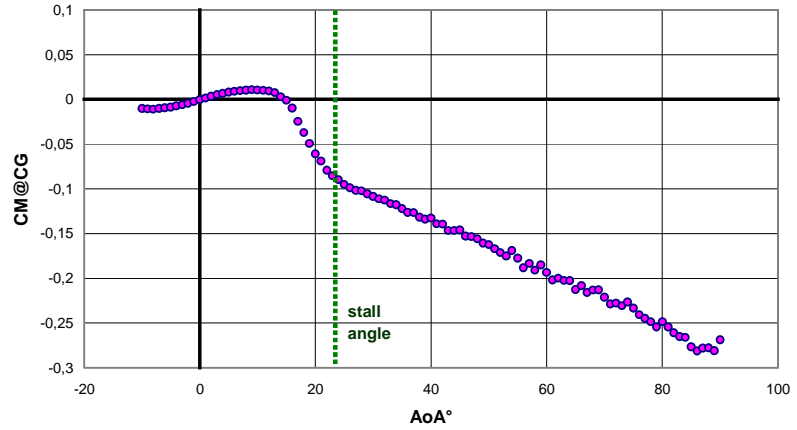


Figure 10. Pitching moment at CG as a function of the angle of attack

C. Powered model analysis

In order to study the behavior of the *Vertigo* in transition flight, specific wind tunnel tests were conducted in conditions representative of level flights. A minimum speed of 3 m/s could be set in the wind tunnel without too many fluctuations and no steady state could be reached at 14 m/s and beyond, because of power limitation.

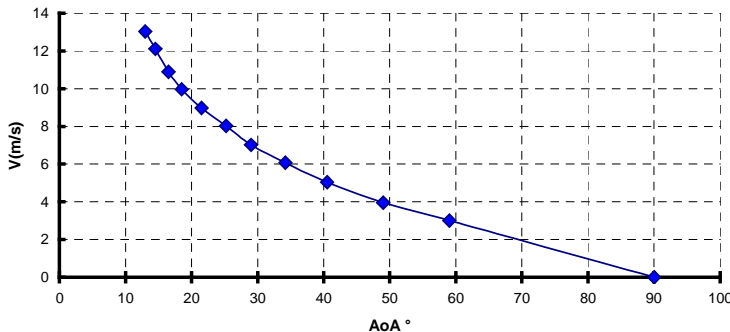


Figure 11. Flight conditions at equilibrium.

Therefore equilibrium states starting from hover (0 m/s) up to 13 m/s were simulated in the wind tunnel with a speed interval of 1 m/s, except for wind speeds of 1 and 2 m/s, for which the free stream flow becomes unsteady. The following data acquisition procedure was applied:

1. A given wind speed chosen in the range 0 to 14 m/s was set in the wind tunnel.
2. Throttle and angle of attack were iteratively set so as to obtain equilibrium values of vertical and horizontal forces

corresponding to a steady flight: no drag force and a lift force of 1.6 kg.

- At that particular combination of free stream speed, throttle and angle of attack, aerodynamic forces and moments were measured.

The resulting equilibrium values of velocity and angle of attack are shown in Fig. 11. The maximum allowable speed is slightly lower than 14 m/s a set of low-pitch blades not suitable for high speeds were initially chosen.

As the flaps could not be set in real time, it was chosen to set them at 0° for the whole test and to measure the resulting pitching moment. Once these tests were done, a second series of tests at equilibrium conditions were done with the wings removed. Assuming that there was little influence from the wing onto the propellers, it was then possible to separately quantify the propellers contribution and the airframe contribution during transition. Figure 12 displays the evolution during transition of the horizontal and vertical components of the aerodynamic forces acting on the propellers on the one hand, and on the whole aircraft on the other hand. It also shows the evolution of pitching moments as a function of the angle of attack up to the prop-hang position (90°), both for the whole aircraft and for the propellers alone. The aircraft vertical force is almost constant and equal to the total weight, while the aircraft horizontal force constantly balances the aerodynamic drag. Figure 11 indicates that steady states do exist over the whole transition regime which is important in case of lateral wind. Indeed, in a dynamic transition simulated through a flight simulator in which all measured aerodynamic coefficients were used, the angle of attack was found to remain in the range 0° to 20° . However, in an outdoor flight, hovering in crosswind requires the existence of steady states at any angle of attack. The propellers vertical force varies linearly over the whole range of angle of attack and the pitching moment induced by the propeller around the center of gravity is positive with a value that is greater than the aircraft pitching moment. As a consequence, the airframe produces a nose-down pitching moment which tends to reduce the positive pitching moment induced by the propellers. It can be observed that the absolute value of the aircraft pitching moment remains almost constant up to 60° with a free stream velocity greatly reduced as the angle of attack is increased (Fig. 12). Therefore, the flaps aerodynamic efficiency at low speeds is an important issue in the design of the wing geometry.

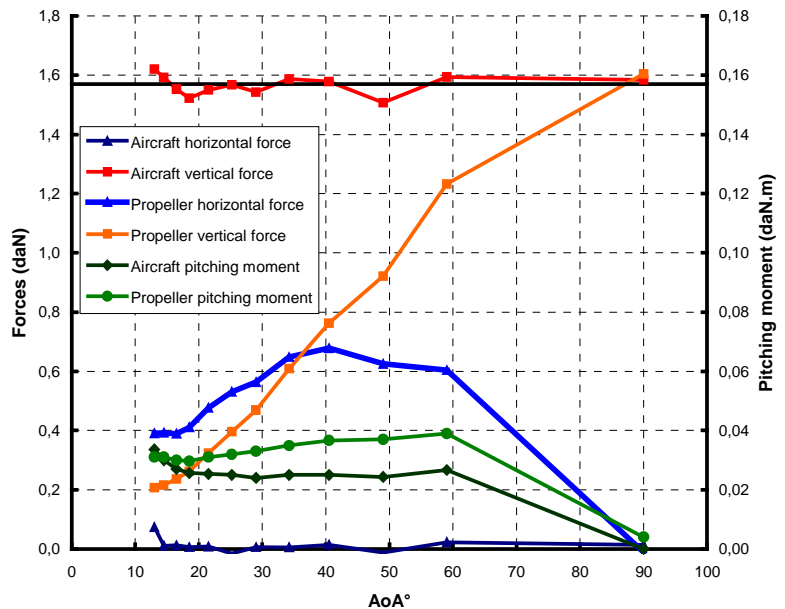


Figure 12. Contributions of propellers during transition: horizontal and vertical force components, pitching moment

D. Scaling effects: the *Mini-Vertigo*

The *Vertigo* was initially built in order to assess the benefit of a coaxial tail-sitter concept for transition flights. It was designed in the mini-UAV size range so as to be able to carry a 200-gram payload. Yet, the ultimate goal is to design and build a smaller version, referred to as the *Mini-Vertigo* in the following. The *Mini-Vertigo* is based on a 300 mm-span flat-plate Zimmerman wing rather than a polygonal wing, since the Zimmerman wing has been shown to allow for better aerodynamic performances at low-Reynolds numbers. Table 1 compares the geometrical properties of

MAV	A	S (dm ²)	m (g)	m/S (g/dm ²)
<i>Vertigo</i>	1.80	24	1600	67
<i>Mini-Vertigo</i>	1.91	5	160	32

Table 1. Comparison of *Vertigo* and *Mini-Vertigo*: wing area, mass and wing loading.

the *Vertigo* and the *Mini-Vertigo*. It appears that while the size is approximately reduced by a factor of 2, the same factor applies for the wing loading, although the present version of the *Mini-Vertigo* does not carry the autopilot yet. The propulsion system was assembled by utilizing two off-the-shelf brushless outrunner motors, *MP Jet AC 22/4-60D*. The motors are joined at their stator backplates with a sufficient space inside the stators to allow a cross shaft through both motors. The motors have a diameter of 27 mm, the total length of the propulsion is 60 mm and the

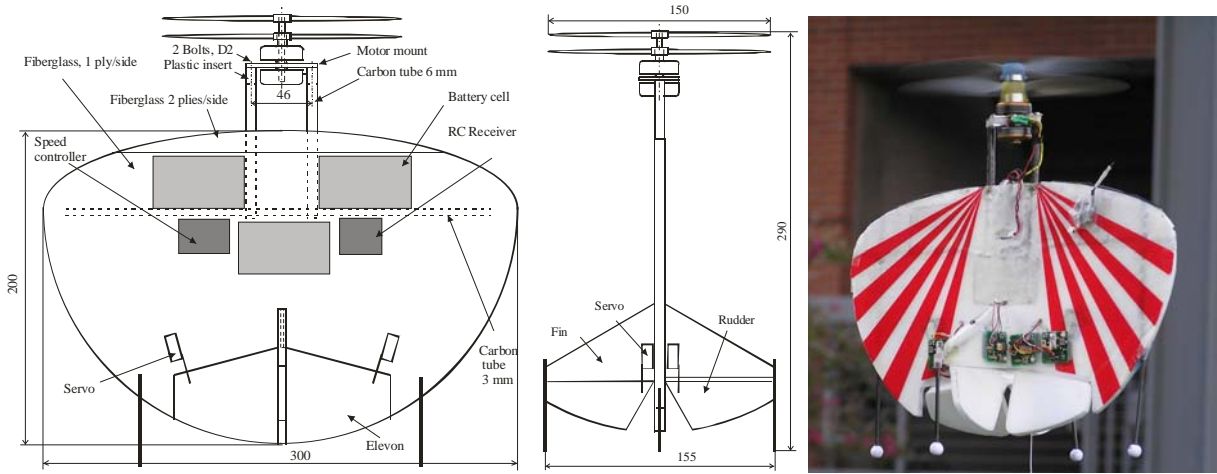


Figure 13. The Mini-Vertigo: schematic views (left, center) and the prototype in hover flight (right).

diameter of the APC counter-rotating propellers is 140 mm with a pitch of 114 mm. The total weight of the motors and the propellers is 50 grams. Both motors are regulated by a single electric speed controller, *Castle Creations Phoenix-25*, providing the same RPM to both motors. The vehicle attitude is controlled through servos by flaps located in the propellers slipstream so as to remain efficient throughout the whole flight domain (Fig. 13). A 3-cell Lithium Polymer battery of 60 grams with a capacity of 740 mAh was integrated in the wing. The wing structure is made of 6-mm thick Depron foam stiffened by resin and by 3-mm carbon rods. The center of gravity is located 30 mm downstream the wing apex.

A series of specific small-scale wind tunnel tests²⁰ were carried out to measure values of thrust, torque, power, and efficiency of the propulsion system. Both pusher and tractor arrangements of propellers were measured and compared against a single motor-propeller propulsion. Hot-wire measurements were conducted to investigate the velocity profile in slipstream. The lower average velocity and significant decrease of velocity in the core of the slipstream as found in the tractor arrangement were attributed to the parasite drag caused by the motors. It causes the decrease of the thrust force observed for the tractor arrangement in comparison with the pusher one. A second series of wind tunnel tests were conducted for a combination of a wing with a motor. It was observed that the drag force on the wing is produced by two mixing airflows: free stream and propeller-induced pulsating slipstream. The zero-lift drag coefficient increases by about three times with propeller-induced speed increase from 0 to 15 m/s indicating the change of transition mechanism in the boundary layer from a laminar to turbulent state.

MAV	D_{rotor} (mm)	T (N)	DL (N/m^2)	P (W)	PL (W/N)	P_{ind} (W)	f_M
<i>Vertigo</i>	500	15.7	80	165	10.5	90	0.545
<i>Mini-Vertigo</i>	140	1.55	101	45	29.0	8.2	0.182

Table 2. Comparison of *Vertigo* and *Mini-Vertigo*: disk loading, power loading and figure of merit.

Table 2 illustrates the differences in hovering performances for the *Vertigo* and the *Mini-Vertigo*. The figure of merit given in Table 2 is not defined in the usual way since it includes the efficiency of the motor. In the present definition, f_M is the ratio of the actual power needed for hovering P_{ind} and the electric power P supplied to the motor. The overall figure of merit measured for the *Vertigo* suggests that the motor efficiency and the propellers efficiency

are both greater than 0.7 which is adequate. By comparison, the poor figure of merit and power loading associated to the *Mini-Vertigo* can be attributed to the off-design use of both motor and propellers. Independent motor efficiency measurements showed that the actual propulsion set has an efficiency factor of 0.4 which means that it does not rotate at its maximum efficiency regime. It also indicates that the propeller efficiency factor is less than 0.5 which can be attributed to low-Reynolds effects but primarily to the fact that the high-pitch counter-rotating propellers used in the present study were adapted to high forward speed and not designed for good hovering performances. This suggests the design and fabrication of specific counter-rotating propellers to allow for lower consumption in hover and to enhance endurance.

Flight tests in RC manual mode have been conducted both in indoor and in outdoor, showing that the present configuration has intrinsic capabilities of both fast horizontal flights and hovering. Current developments include the design and implementation of control laws to autonomously perform transition flights.

V. Conclusion

Hovering capabilities of fixed-wing MAV configurations were investigated through the comparison of three different concepts. First, the adaptation of a tilt-wing configuration for MAVs was investigated. An experimental side-by-side comparison of two bimotor tilt-wing and tilt-body configurations showed that there is little interest in developing a tilt-wing concept for MAVs, except for very high tilt angles where the reduction in equivalent aspect ratio is beneficial to the lift force. However, the additional weight due to the tilting mechanism would ruin the benefit of a tilt-wing configuration. Furthermore, for an unmanned vehicle, the horizontal attitude of the fuselage is not as essential as for transport aircraft. Second, based on that conclusion, the tilt-body configuration was preferred and further investigated under the form of a coaxial tail-sitter. A first 700-mm mini-UAV prototype, the *Vertigo*, was designed and fabricated. A wind tunnel model was tested with a wind speed ranging from 0 to 15 m/s to assess its ability to perform transition in equilibrium. Scaling effects were considered through the design and fabrication of a smaller 300-mm version based on a Zimmerman wing, the *Mini-Vertigo*, for which a series of detailed propulsion tests were carried out. Although the hovering performances of both coaxial tail-sitter are not optimized, both prototypes could actually achieve transition from hovering to horizontal flight. Finally, the present study indicates that tilt-body fixed-wing coaxial configurations are promising concepts for vertical and horizontal flights.

Acknowledgments

This research project represents a transatlantic collaborative effort of the “Institut Supérieur de l’Aéronautique et de l’Espace” (ISAE) and the University of Arizona towards the development of VTOL MAV technologies. It was partly funded by the European Office for Aerospace Research and Development under grant FA8655-07-M-4010, program manager Dr. Surya Surampudi, for ISAE and by the Air Force Research Laboratory, program manager Dr. Gregg Abate, for the University of Arizona. The tilt-body part was also partly sponsored by the French Armament Procurement agency (DGA), program manager Mr. Loïc Boudet (DGA/MRIS). The authors would like to thank Dominique Bernard for the design and fabrication of the *Vertigo* prototype and the following members of the Micro Air Vehicle Project at both universities for their contributions to this work: Bill Silin, David Addai, and Damien Poinot. S. Shkarayev would like to thank the SUPAERO team for their support of research on VTOL MAVs during his visiting appointment there.

References

- ¹Moschetta, J.-M., “New Trends and Capabilities for Micro Air Vehicle Systems,” *Proceedings of the UAV World Conference 2007*, October 24-25, 2007, Frankfurt, Germany.
- ²Johnson, B., Stanford B., Jagdale V., Ifju P., “Development of a Composite Bendable-Wing Micro Air Vehicle,” *45th AIAA Aerospace Sciences Meeting and Exhibit, 8-11 January 2007, Reno Nevada*, AIAA Paper 2007-1044, January 2007.
- ³Henry, J. I., Schwartz, D. R., Soukup, M. A., Altman, A., “Design, Construction, and Testing of a Folding-Wing, Tube-Launched Micro Air Vehicle,” *43th AIAA Aerospace Sciences Meeting and Exhibit, 10-13 January 2005, Reno Nevada*, AIAA Paper 2007-1451, January 2005.
- ⁴Moschetta, J.-M., Thipyopas, C., “Aerodynamic Performance of a Biplane Micro Air Vehicle,” *Journal of Aircraft*, vol. 44, No. 1, 2007, pp. 291-299.
- ⁵Suhariyono, A., Kim, J. H., Goo, N. S., Park, H. C. and Yoon, K. J., “Design of precision balance and aerodynamic characteristic measurement system for micro air vehicles”, *Aerospace Science and Technology*, Vol. 10, 2006, pp. 92-99.
- ⁶Kochersberger, K., Abe, C., “A Novel, Low Reynolds Number Moment Balance Design for Micro Air Vehicle Research,” *23rd AIAA Applied Aerodynamics Conference, June 6-9, 2005, Toronto, Ontario, Canada*, AIAA paper 2005-4759, June 2005.

- ⁷Pelletier, A. and Mueller, T.J., "Low Reynolds Number Aerodynamics of Low-Aspect-Ratio, Thin/Flat/Cambered-Plate Wings," *Journal of Aircraft*, Vol. 37, No. 5, 2000, pp. 825-832.
- ⁸Kline, S. J., and McClintock, F. A., "Describing Uncertainties in Single-Sample Experiments," *Mechanical Engineering*, Vol. 75, No.1, 1953, pp. 3-8.
- ⁹Barlow, J. B., Rae, W. H., Jr., and Pope, A., *Low-Speed Wind Tunnel Testing*, 3rd Ed., Wiley, New York, 1999, Chap. 10.
- ¹⁰Kellogg, J.C., "Case Study: Micro Tactical Expendable Rigid-Wing Micro Air Vehicle", *Introduction to the Design of Fixed-Wing Micro Aerial Vehicles*, edited by J. Mueller, J. C. Kellogg, P. G. Ifju, and S. V. Shkarayev, AIAA, Reston, VA, 2006, pp. 151-184.
- ¹¹Aki, M., Waszak, M., and Shkarayev, S., "Development of Micro Air Vehicles with In-Flight Adaptive Wing," Chapter 6, *Introduction to the Design of Fixed-Wing Micro Aerial Vehicles*, edited by J. Mueller, J. C. Kellogg, P. G. Ifju, and S. V. Shkarayev, AIAA, Reston, VA, 2006, *Journal of Aircraft*, Vol. 42, 2005, pp. pp. 241-275.
- ¹²Shkarayev, S., Moschetta, J.-M., Bataillé, B., "Aerodynamic Design of VTOL Micro Air Vehicles", *Proceedings of the 3rd US-European Competition and Workshop on Micro Air Vehicle Systems (MAV'07)*, September 17-21, 2007, Toulouse, France.
- ¹³Müller M., Schröter A., Lindenberg C., "The M.A.C.'07 MAV," *Proceedings of the 3rd US-European Workshop and Flight Competition on Micro Air Vehicle Systems (MAV07)*, September 17-21, 2007, Toulouse, France.
- ¹⁴Green, W. E., Oh, P. Y., "A MAV That Flies Like an Airplane and Hovers Like a Helicopter," *Proceedings of the 2005 IEEE/ASME International Conference on Advanced Intelligent Mechatronics*, July 24-28, 2005, Monterey, California.
- ¹⁵Kubo, D., "Study on Design and Transitional Flight of Tail-Sitting UAV," *Proceedings of the 25th International Congress of the Aeronautical Sciences (ICAS 2006)*, September 3-8, 2006, Hamburg, Germany.
- ¹⁶Marek, P., Smrcek, L., "Development of DART MAV- Fixed Wing Hover-capable Micro Aerial Vehicle," *Proceedings of the 5th International Conference on Advanced Engineering Design (AED 2006)*, June 11-14, 2006, Prague, Czech Republic.
- ¹⁷Chana, W. F., Coleman, J. F., "World's First VTOL Airplane Convair/Navy XFY-1 Pogo", *Proceedings of the International Powered Lift Conference*, November 1996, Jupiter, Florida, p. 99-104.
- ¹⁸Bataille, B., Poinso, D., Thipyopas, C., and Moschetta, J.M., "Fixed-Wing Micro Air Vehicles with Hovering Capabilities," *NATO RTO meeting, AVT-146, Symposium on "Platform Innovations and System Integration for Unmanned Air, Land and Sea Vehicles"*, Florence, Italy, May 14-17, 2007.
- ¹⁹Mueller, T. J., Torres, G. E., Strull D. W., "Elements of Aerodynamics, Propulsion, and Design", in *Introduction to the Design of Fixed-Wing Micro Air Vehicles*, Eds. Mueller T. J., Kellogg, J. C., Ifju, P. G., Shkarayev, S. V., AIAA Education Series, AIAA, 2007, p. 52.
- ²⁰Shkarayev, S., Moschetta, J.-M., Bataillé, B., "Aerodynamic Design of Micro Air Vehicles for Vertical Flight", *Journal of Aircraft* (submitted for publication), November, 2007.

This page intentionally left blank

Appendix 3

Investigation of Flight Dynamics and Automatic Controls for Hovering Micro Air Vehicles

This page intentionally left blank

Investigation of Flight Dynamics and Automatic Controls for Hovering Micro Air Vehicles

Damien Poinso¹ and Caroline Bérard²

ONERA and Institut Supérieur de l'Aéronautique et de l'Espace, Université de Toulouse, France

Roman Krashanitsa³ and Sergey Shkarayev⁴

The University of Arizona, Tucson, AZ, USA

The present work describes the development of an automatic control system and the investigation of the flight dynamics of fixed-wing micro air vehicles (MAVs) with vertical take-off and landing (VTOL) capabilities. Specifically, the hovering phase of the flight was studied in detail. A state-space model was formulated and used in a control law design. The effects of propeller slip stream impinging on the airframe are discussed in the context of control design. Feedback control laws based on a proportional, integral, and derivative (PID) control design were developed and programmed into the autopilot. The development and evaluation of two VTOL MAVs with wingspans of 65 and 31 cm are presented. A number of test flights of vehicles with attitude stabilization and altitude hold were conducted with telemetry acquisition. Despite the difference in size, similarities were noted in the dynamic response for both aircraft. The actuation delays in the propulsion systems caused a systematic error in an altitude. Average amplitudes of rotational oscillations in all three axes were also about the same for both aircraft. Higher roll rates can be explained by lower inertia in roll axis.

Nomenclature

\mathbf{A} , \mathbf{B}	= state-space model operators
C_{D_0}	= zero-lift drag coefficient
D	= drag force
G_x	= transfer function
I_{xx}	= moment of inertia about x -axis
I_{yy}	= moment of inertia about y -axis
I_{zz}	= moment of inertia about z -axis
K_p	= proportional gain coefficient
K_d	= derivative gain coefficient
K_i	= integral gain coefficient
m	= take-off mass of an aircraft

¹ PhD candidate, Department of Flight Dynamics and Systems Control, ONERA-DCSD BP 74025 and Department of Mathematics, Computer Science and Control Theory, ISAE BP54032, FR-31055 Toulouse Cedex 4, France, Damien.Poinso@cert.fr.

² Professor, Department of Flight Dynamics and Systems Control, ONERA-DCSD BP 74025 and Department of Mathematics, Computer Science and Control Theory, ISAE BP54032, FR-31055 Toulouse Cedex 4, France, caroline.berard@isae.fr.

³ Research Assistant Professor, Department of Aerospace and Mechanical Engineering, The University of Arizona, P.O. Box 210119, Tucson AZ, USA, 85721-00119, ryk@email.arizona.edu.

⁴ Associate Professor, Department of Aerospace and Mechanical Engineering, The University of Arizona, P.O. Box 210119, Tucson AZ, USA, 85721-00119, svs@email.arizona.edu, Senior Member AIAA.

p	= roll rate
q	= pitch rate
R_p	= propeller radius
r	= yaw rate
S_p	= part of area of the wing covered by propeller slipstream
T	= thrust force
w_p	= air velocity induced by a propeller
\mathbf{x}	= state vector
Z	= altitude, vertical coordinate in the Earth-fixed frame
ζ	= damping ratio
δ_t	= throttle command

I. Introduction

The development of the automatic controls for micro air vehicles (MAVs) is a very challenging engineering problem due to the low inertia and damping properties of these vehicles. The situation worsens for the fixed-wing MAVs with vertical take-off and landing capabilities (VTOL) being developed.¹⁻³ Hovering MAVs are open-loop unstable and an autopilot's ability to handle them has not been established. Thus, enhanced automatic flight control systems are vital for the progress of VTOL MAV technology.

Design methods and general theoretical control principles for large VTOL aircraft are well developed and have been summarized in the literature.^{4,5} As the field of VTOL evolved, much attention was paid to propulsion system considerations and development of an aerodynamic theory for the propeller and rotor. Other subjects included control issues during hover and transition. Overall, there is a sufficient amount of relevant data and knowledge to begin exploring autonomous flight concepts with applications to VTOL MAVs.

The flying qualities of a MAV will have to provide adequate mission performance. In a study by Foster and Bowman,⁶ the dynamic stability of several small air vehicles was analyzed using predictive software. It was found that use of the flying qualities criteria established for large airplanes (e.g., military specifications⁷) is not acceptable for small unmanned air vehicles. Flying quality guidelines were proposed for small aircraft by scaling down the standards used for larger aircraft. Note that the standards for flying qualities of piloted aircraft are based on evaluations of handling qualities made by many pilots for multiple aircraft under different flight conditions. Contrary to requirements for manned aircraft, design requirements for the flying quality of unmanned MAVs may be governed by some other requirements, for example, video stream quality, while the safety of passengers and pilots is not an issue. Although this problem has been addressed in the recent technical literature, more studies are needed.

The stability of conventional MAVs has been investigated by Waszak et al.⁸ and Ifju et al.⁹ The authors found that higher angles of attack may be achieved without stalling using a flexible wing that deforms under varying aerodynamic loads, including gust conditions, allowing the wing to see a lower angle of attack at higher pitch attitudes. An analysis of the static stability derivatives showed the aircraft to be stable in all axes.

Available off-the-shelf autopilots and micro avionics components, especially micro sensors, are very expensive, heavy, and of poor quality. In industry, proprietary systems are created, preventing a dissemination of knowledge on the development of autonomous MAVs. Alternatives to this situation are projects (e.g., in Ref. 10) that are founded on the principle of free software and hardware schematics.¹¹ Even though documentation and schematics for these autopilots are free, a lack of technical support makes these alternatives unattractive as well.

Several MAVs equipped with automatic control systems have been developed to date. A study by Platanitis and Shkarayev¹² focused on the integration of the MP2028⁸ autopilot system into a 90-cm (36-inch) Zagi MAV. The aircraft provides a useful platform for evaluating autopilot integration into MAVs of comparable size. The autopilot uses various feedback loops for navigation and control during autonomous flight. While one may use empirical approaches (i.e., pick gains, validate in-flight tests, then adjust gains) to determine appropriate gains, the motivation of this research was to provide a more systematic approach to determining feedback loop gains. The approach involves determining an analytical model of the aircraft from its structural and aerodynamic characteristics that can then be validated through wind tunnel experiments, and developing the feedback control loops using standard design methods. Failures of the expensive autopilot components during ground tests prevented autonomous flight from taking place.

Taylor et al.¹³ developed an attitude stabilization system based on thermal horizon detection. The system is reliable in daytime or nighttime flight, consumes little power, and operates quickly from a cold start. Such a control system even allows an unskilled pilot to fly a UAV.

Arning and Sassen¹⁴ presented a 42-cm (16.5 in) autonomous MAV developed at EADS Dornier. The potential of using MEMS technology to provide size and weight savings, along with reduced power consumption for autopilot hardware mounted on the MAV, was realized. The study provided an overview of the application of sensors for the development of micro flight controls. Despite the current progress in sensor technologies, available micro sensors and controllers suffer inaccuracies and instabilities. An alternative solution is hybridization that combines different sensors into one system.

International Micro Air Vehicle Competitions have showcased MAVs that demonstrated aircraft flight via an autopilot. Brigham Young University¹⁵ used a Kestrel autopilot. A similar system utilizing a Kestrel autopilot was developed at the University of Florida.¹⁶

A control system for autonomous flight of an MAV for a surveillance mission was developed at RWTH Aachen University.¹⁷ The aircraft had a 40-cm wingspan and a total mass of 250 g. An existing autopilot system was modified by the augmentation of a GPS receiver and telemetry system, which uses a waypoint navigation algorithm. The existing system consisted of three piezoelectric gyros, two pressure sensors (static and dynamic), and a microcontroller to run the control algorithms and invoke control commands. Waypoint navigation algorithms, which included altitude and velocity hold, azimuth control, and flight-quality algorithms, were added to the control system. Proportional control is used to command heading, and PI control is used for altitude and speed hold. Newly developed control laws were integrated into a ground station, allowing gain factors and waypoints to be modified during flight.

Konkuk University¹⁸ improved the flight ability of their MAV entry. A micro-scale inertial measurement system, the MR01, was developed for the micro-scale autopilot system. The MR01 consists of a one-axis gyroscope sensor, and a two-axis accelerometer. When attitude data measured by the MR01 were used as a feedback for the servomotor control, longitudinal and lateral stabilities improved. Successful missions have been flown using 13-15-cm wingspan MAVs for surveillance in 5 m/s headwinds.

A comprehensive control design and modeling of a vertical-horizontal and horizontal-vertical flight transition maneuver for the T-Wing tail-sitter aircraft is done by R. H. Stone et al.¹⁹ The concept aircraft with a wingspan of 2.2 m can be qualified as an unmanned air vehicle (UAV). The authors present a complete set of dynamic equations of motion available elsewhere and customized for their project. Numerical simulations of the closed-loop controller are done using quaternion attitude representation. The custom autopilot utilizes linear control laws based on a mixed approach of the attitude descriptor, whereas vertical, horizontal, and transition modes of flight are implemented. Euler angles are used for the horizontal flight mode, while a 90-deg-tilted frame is used for the hovering mode, and the quaternion-based frame is used in transition. In vertical mode, the controller uses proportional-integral (PI) laws to control heading, or aircraft belly direction using elevator and ailerons, and also PI laws to control throttle. In transition mode, the controller gain is scheduled with speed and throttle. Flight testing was done using a tether rope setup to reduce the number of crashes. In addition to tether testing, the vehicle has also been flown freely to perform autonomous take-off and transitions. While there were no serious problems in any of the modes, the aircraft has had some difficulties with reverse horizontal to vertical transition when angle of attack exceeded 60 deg.

Simulations and control laws developed by Knobel et al.²⁰ for tail-sitter UAVs feature quaternion-based attitude estimation. Results of simulation using commanded pitch and thrust produced satisfactory results in terms of positional error along horizontal and vertical axes. Future research will focus on implementing the control laws using a Kestrel autopilot and tail-sitter RC model airplane, Pogo.

The University of Arizona MAV project^{21,22} has been focusing on the development of fully autonomous MAVs since 2003. Several research and development studies conducted at the University of Arizona on the aerodynamics, airframe, and control design of MAVs have been completed, resulting in two exceptional fully autonomous MAVs: 59-cm Zagi and 30-cm Dragonfly. Both aircraft are equipped with a Paparazzi autopilot.¹⁰ The Zagi is a relatively large but stable (yet very maneuverable) and rugged platform and, therefore, is well suited for experimental investigations of the flight control systems. The Dragonfly is about half the size of the Zagi, but possesses unique flight characteristics, including high maneuverability.

Conventional design of large aircraft is a two-step process, in which the aerodynamic design of an airframe focuses on satisfying performance requirements and then control laws are designed for required stability and controllability. For MAVs, a strong coupling between the airframe and control system design has been found.²⁰⁻²³

The purpose of this paper is to investigate size effects and to provide closed-loop control laws for autonomous MAVs capable of hovering. Two VTOL MAVs were evaluated: Vertigo and Min-Vertigo. The Mini-Vertigo is two times smaller than the Vertigo, thus the two aircraft present a workable experimental setup for the investigation of

size effects on flight dynamics and designing control laws for VTOL MAVs. The approach utilized in this study includes the simulation of flight dynamics and closed-loop control design. In a series of flight tests of the two aircraft, telemetry data on control actuation, altitude, and attitude of the aircraft were collected and analyzed and used in the validation of predicted designs.

II. Autonomous VTOL MAV Designs and Specifications

In the present study, the Vertigo (Fig. 1) and the Mini-Vertigo (Fig. 2) MAVs were evaluated. Geometrical and mass data for the MAVs and their components are presented in Tables 1 and 2. Both aircraft are of a tail-sitter configuration capable of vertical take-off, hover, transition, and level flight. The 31-cm-wing-span Mini-Vertigo is two times smaller than 65-cm-wing-span Vertigo and, therefore, is better qualified as an MAV category airplane. The Vertigo was designed in the mini-UAV size range and is able to carry a payload up to 200 g, while the Mini-Vertigo has 50-g payload capability. Both airplanes can be equipped with video cameras that capture and transmit video to a ground station for analysis, making them very effective for surveillance missions. With an autopilot integrated into the airplanes, they currently are capable of automatic hovering.

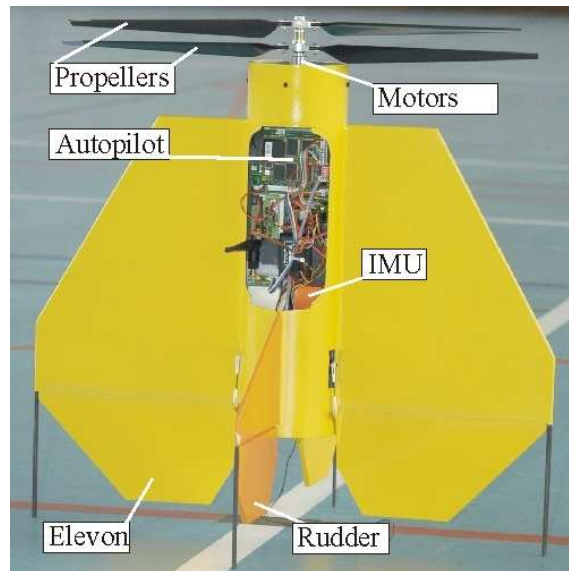


Fig. 1 The 65-cm Vertigo.

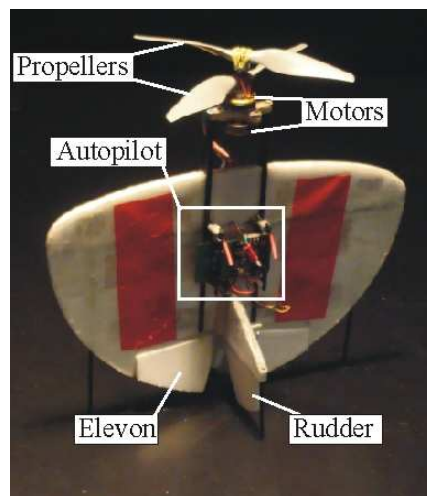


Fig. 2 The 31-cm Mini-Vertigo.

The propulsion system of the Vertigo consists of two coaxial contra-rotating propellers driven by two side-by-side motors via a gear box. The airframe is constructed of two flat plate wings of polygonal planform and two vertical fins symmetrically placed on either side of the 12-cm-diameter fuselage. The total mass of the airplane is 1.675 kg. The wings and fins are attached to the fuselage, which also serves as a compartment for the autopilot, radio transmitter, and batteries.

The Mini-Vertigo is a flying wing airplane with dorsal and ventral fins added for lateral stability. The total mass of the airplane is 243 g. It has a tractor propulsion system consisting of two coaxial contra-rotating motors-propellers.

The controls for both aircraft include elevons in the longitudinal direction and elevons and a rudder in the lateral direction.

Table 1 MAV specifications and properties.

Parameter	Vertigo	Mini-Vertigo
Wingspan (cm)	65	31
Length (cm)	70	21
Height (cm)	48	16
Wing area (cm ²)	2200	486
Elevon area (cm ²)	830	60
Elevator area (cm ²)	512	-
Fin area (cm ²)	735	40
Rudder area (cm ²)	318	35
Propeller diameter (cm)	50	14
CG location from apex (cm)	14.5	4.16
I_{xx} , kg m ²	0.0051	0.00046
I_{yy} , kg m ²	0.0204	0.00109
I_{zz} , kg m ²	0.0229	0.00133

Table 2 Components of MAVs.

Vertigo		Mini-Vertigo		
Component	Description	Mass (g)	Description	Mass (g)
Airframe	Composite structure	1100	Composite structure	60
Motor, propeller	Axi 22 12/26, ISAE 500 mm	80	MP Jet AC 22/4-60D APC 7"-5"	50
Lithium-Polymer Battery	3 cells, 11.1V, 4000 mAh	340	3 cell, 11.1V, 910mAh	65
Autopilot	ISAE autopilot	80	Paparazzi autopilot	54
Modem	MaxStream XbeePro	5	MaxStream XBee Pro	5
Servos	Futaba S3150	70	Blue Arrow BA-TS-2.5	9
Total		1675		243

The xyz -coordinate system is a body-fixed frame with the origin in the center of gravity. The wingspan of the Vertigo is about two times greater than that of the Mini-Vertigo, and the Vertigo's weight is 6.9 times greater. Moments of inertia for both airplanes are presented in Table 2. While the moments of inertia in the pitch, I_{yy} , and yaw, I_{zz} , directions differ by about 20 times, the roll, I_{xx} , differs by 10 times. Low roll inertia is one major factor affecting the relatively poor stability of MAVs in the lateral direction.²²

Both MAVs were outfitted with autopilots, but at this stage of the project, the automatic controls have been developed for hovering mode only.

An ISAE autopilot was integrated into the Vertigo. It features AT91SAM7A3 microprocessors, the functions of which are uploading the flight plan, reading sensor feedback signals, and generating control signals to the motor speed controller and rudder and elevons servos. The sensor block consists of a Ublox GPS unit, Xsens MTX IMU, ultrasonic sensor (SRF10), and static pressure sensor (MPX 6115-A).

The Mini-Vertigo aircraft is outfitted with a Paparazzi autopilot.¹⁰ The autopilot includes an autopilot board, two double-axis MEMS gyroscopes (IDG300), an infrared attitude sensor (FMA Co-Pilot) and ultrasonic range sensor (Maxbotix LV-EZ1). The autopilot board reads sensor feedback signals and generates control signals to the motor speed controller, rudder, elevator, and elevon servos. The autopilot board features an ARM7 processor running at 60 MHz. This single processor performs control loops, navigation, data acquisition, and telemetry communications.

In flight, the autopilots send telemetry data back to the ground station using the XbeePro modems. Currently, the telemetry data include: GPS-based location coordinates; ground speed, altitude, and climb rate of the airplane; attitude of the airplane provided by infrared sensors; autopilot status data; and position of the control surfaces. The telemetry data are used to display up-to-date information about the location of the airplane on a map, the attitude of the airplane, and its altitude.

III. Control Law Design

In order to evaluate the effectiveness of control laws for a VTOL micro air vehicle, a design process that makes use of the linearized equations of motion of the aircraft is followed herein.

A. Dynamic Equations of Motion for VTOL MAV

The equations of motion are developed from an evaluation of stability and control derivatives in both the longitudinal and lateral-directional motions subsequently assembled into state-space matrices. The MATLAB/SIMULINK program is used to evaluate the stability of the airplane, as well as to determine control laws for closed-loop stability. Once the stability and control derivatives are determined, they are then integrated with the mass, geometric, and inertial properties to obtain the equations of motion in state-space form for each of the longitudinal and lateral motions

$$\dot{\mathbf{x}} = \mathbf{A}\mathbf{x} + \mathbf{B}\mathbf{u} \quad (1)$$

where the state vector is $\mathbf{x} = [u, v, w, p, q, r, q_0, q_1, q_2, q_3, x, y, z]^T$. The state-space form as described in²⁴ was used for matrices \mathbf{A} and \mathbf{B} . Matrix \mathbf{A} contains the variables for mass, moment of inertia, and dimensional stability derivatives for the motion variables. Matrix \mathbf{B} is the control influence matrix containing derivatives for all control surfaces, thrust coefficients, as well as aircraft mass and inertia variables. Matrix variables for the Vertigo airplane are reported in Ref. 23.

Unlike conventional aircraft, the effect of the propeller slipstream impinging on the wing may be dominant for VTOL aircraft. For the MAVs studied, the thrust line is assumed to pass through the center of gravity of the aircraft. As such, the thrust force, T , will not create any moments about the aircraft center of gravity. However, for these airframes, the propeller slipstream may develop a drag force, D , that needs to be accounted for.

Consider a hovering rigid aircraft with a take-off mass of m . It is oriented along the vertical Z -axis in the Earth-fixed frame of reference. The equation of motion of the aircraft in the Z -direction can be written as

$$m\ddot{Z} = T - D - mg \quad (2)$$

Assuming that velocity induced by a propeller is constant along the stream tube and is equal in magnitude to its ultimate value as derived in the propeller momentum theory,⁴ it is given for hover as

$$w_p = \sqrt{\frac{2mg}{\rho\pi R_p^2}} \quad (3)$$

The disk loading parameter is defined as a ratio of the thrust force (which is equal to the weight for hovering) to the propeller disk area, $mg/\pi R_p^2$. The disk loading for the Vertigo is 83.65 N/m², which is lower than the value of 154.7 N/m² for the Mini-Vertigo. These results explain the overall very small value of the drag for the Vertigo in comparison with the Mini-Vertigo.

The drag-to-thrust ratio is derived as

$$\frac{D}{T} = \frac{C_{D_0} S_p}{\pi R_p^2} \quad (4)$$

where C_{D_0} is the zero-lift drag coefficient, and S_p is the area of the part of the airframe covered by the propeller slipstream. From Eq. (4), it follows that the drag-to-thrust ratio does not depend on the thrust value explicitly.

The drag and thrust forces for both MAVs were measured in a series of tests. Details of the experiments are reported in Refs. 2 and 25. The tests were conducted with a pulse width modulation (PWM) varying from 55 to 70%. Drag-to-thrust ratios obtained for the Vertigo are negligible (less than 0.001). The range of values for the Mini-Vertigo is higher, 0.073-0.085, but is rather narrow. Based on these results, the drag term was excluded from the simulations of dynamic motion and control design for both MAVs.

B. Control Law Design

In the latest stage of the project, control laws were developed and evaluated for the attitude stabilization and altitude hold in hover. An inertia measurement unit (IMU) and an acoustic range sensor were utilized for attitude and altitude measurements. Specifically, the altitude, Z , was measured by ultrasonic sensor and linear accelerometers. In each control loop, the same PID design was used; however, only the altitude control will be presented in this section.

A classical approach is realized for the stabilization of the aircraft, in which the motion along the aircraft flight path axes is uncoupled. This way a mono-input design synthesis can be applied.

The closed-loop stability of the altitude-to-throttle transfer function was determined and a PID controller was designed, as shown in Fig. 3. Proportional and derivative feedbacks are related to the altitude, Z , and vertical velocity, \dot{Z} . The desired altitude, Z_{des} , is the input to the control and the output of the control loop is the throttle command, δ_t . Saturations 2 and 3 are added in order to limit the overshoot generated by the integral effect and to provide the desired performance. Saturations 1 and 4 in the input and output of the controller assure safety operations. Initial control loop parameters (gains and saturation cut-off limits) were selected based on results of numerical simulations for both aircraft.

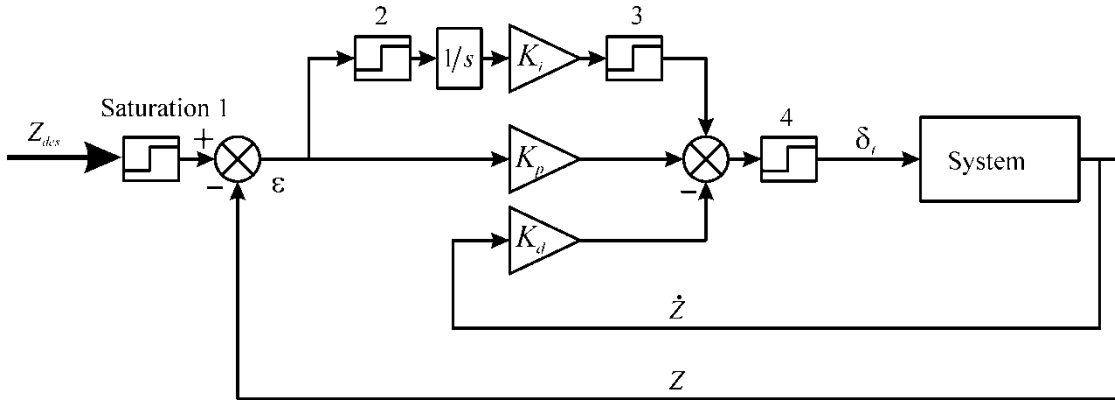


Fig. 3 Schematics of PID controller.

For the Vertigo aircraft, the optimal control was developed based on the root locus diagram and Bode plot. As discussed in the previous section, the system control is greatly affected by propulsion's reaction time. In order to effectively model the reaction time of the speed controller-motor-propeller, a classical first-order system is defined. The transfer function of the system is given by

$$G(s) = \frac{mg}{(\tau s + 1)s^2} \quad (5)$$

where τ is the time constant.

Initially, the altitude control was modeled as a PD controller, $G_c(s)$, represented by a transfer function

$$G_c(s) = K_p \left(1 + \frac{K_d}{K_p} s \right) \quad (6)$$

Optimal gains were augmented by addition of the integral control and saturation functions in order to reduce the permanent error and at the same time reduce the time constant of the controller.

The open-loop global transfer function, G_0 is a product of $G(s)$ and $G_c(s)$. The altitude-to-throttle closed-loop transfer function is

$$G_{CL}(s) = \frac{G_o(s)}{1 + G_o(s)} \quad (7)$$

First, for the gain synthesis, proportional, K_p , and derivative, K_d , gains were tuned using a modal approach²⁴ for closed-loop poles. The poles were chosen to satisfy performance constraints, damping, and time response. In the second step, the integral effects were introduced via integral gain, K_i , obtained by the Ziegler-Nichols method.²⁵ Saturations 2 and 3 (Fig. 3) were tuned based on numerical simulations and further flight tests.

The proposed control design is validated by time response simulations, observations of the root locus diagram, and several robustness margins. Figure 4 shows the root locus diagram for altitude hold. Figure 5 illustrates a transient roll response of the Vertigo to the step function of the closed-loop altitude control. In addition, a compromise between the pass-band and delay margin was found. Finally the set of gains was determined as $K_p = 0.1, K_d = 1.5, K_i = 0.02$. With these gains, the closed-loop poles placed at -0.82 and $-1 \pm 1.56i$ ($\zeta = 0.55$) and the delay margin of 0.55 s provided robustness of the control.

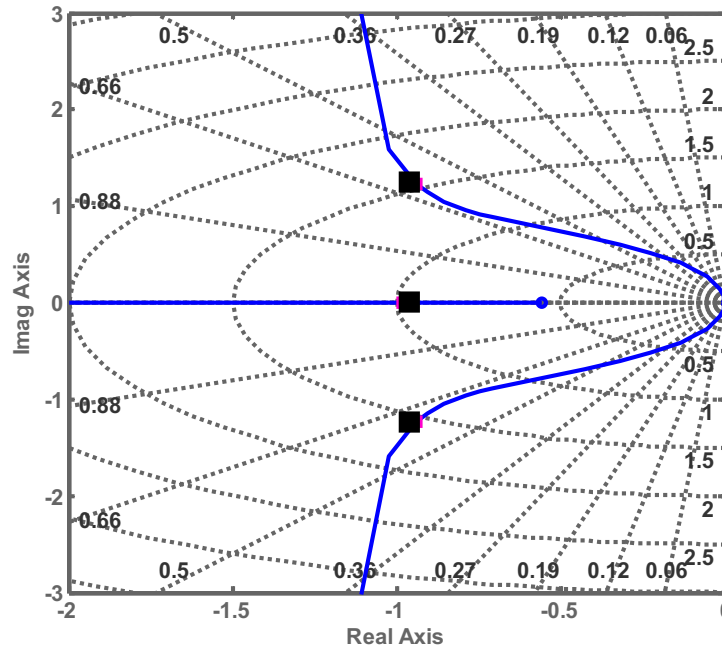


Fig. 4 Root locus for altitude hold PD (square symbols represent the optimal gains).

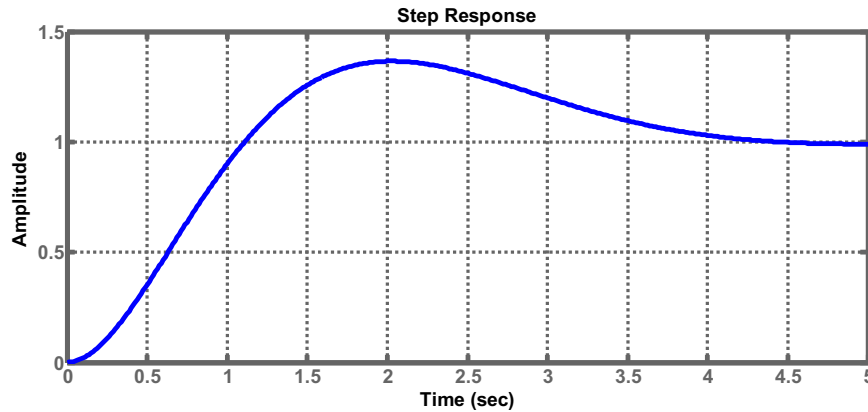


Fig. 5 Time response of the Vertigo to the throttle command in the form of a step function.

IV. Flight Testing

In a series of flight tests, the response of the Vertigo and Mini-Vertigo to prescribed altitude control commands was investigated and reported. During these tests, control gains were tuned to achieve the most effective and stable response. Telemetry data on altitude response, angular velocities, and servo signals were acquired in two autonomous flights (flight 1 and flight 2) for both Vertigo and Mini-Vertigo. Two different sets for the control gain coefficients (set 1 and set 2) were used in flight 1 and 2, respectively, where the set 1 was an initial set of coefficients and set 2 coefficients are the results of fine-tuning in flight tests.

A. Vertigo

The telemetry data for the altitude and its desired value are presented in Figs. 6 and 7 for flight 1 and 2, respectively, and corresponding throttle command time histories are shown in Figs. 8 and 9.

At 20 s of flight 1 (Fig. 6), the aircraft had slowly reached the desired altitude. The oscillations observed are due to the delay in the speed-controller-motor-propeller chain. The delay of the altitude response was estimated at 0.2 s and 0.35 time constant, a problem for efficient feedback. It can be seen in Fig. 6 that with further changes in the desired value, the measured altitude followed a desired value.

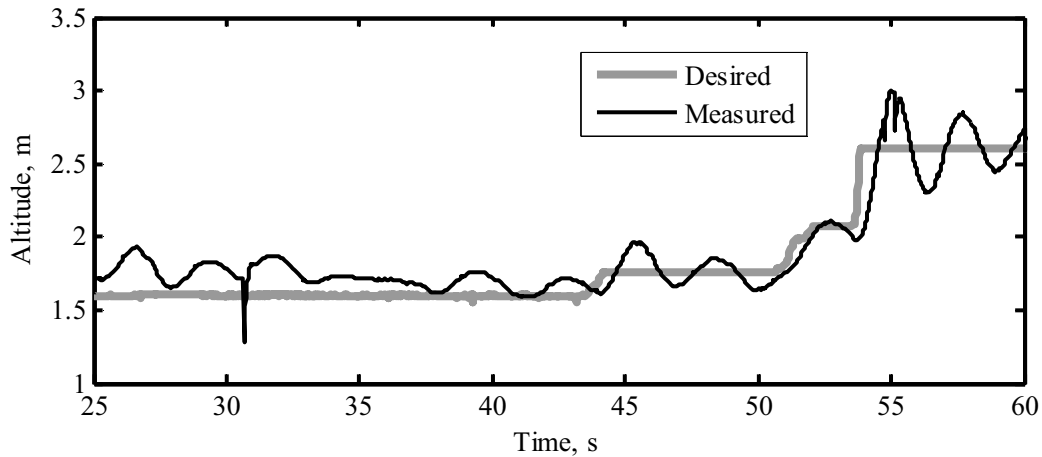


Fig. 6 Measured and desired altitudes for the Vertigo during flight 1.

For the second flight, the general trends in the altitude hold are the same as in the first flight. The difference is in the longer time period and increases and decreases of the desired altitude. This is similar to a previously observed lag between desired and real altitudes at the beginning of the flight, which slowly decreases to the end of the flight.

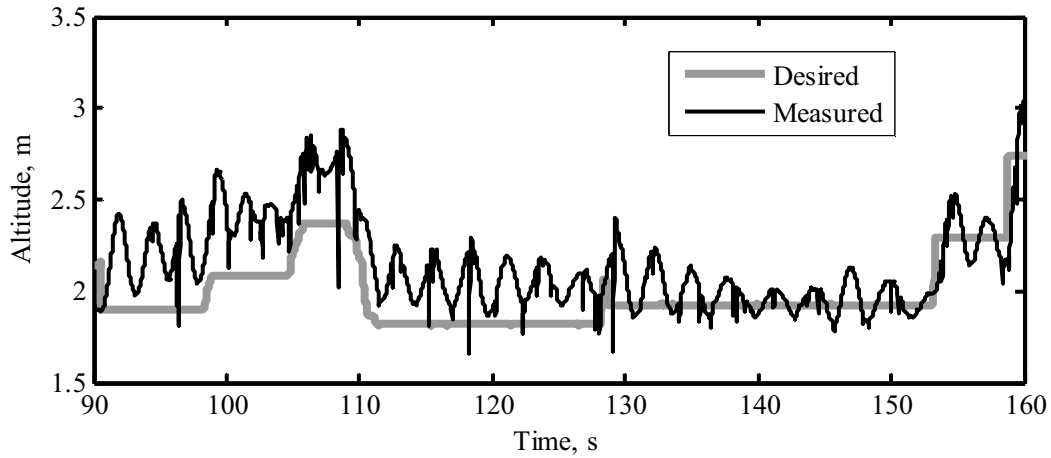


Fig. 7 Measured and desired altitudes for the Vertigo during flight 2.

The plots in Figs. 8 and 9 illustrate the throttle variation for flights 1 and 2, respectively. The range of the throttle is set in terms of PWM varied from 0 to 1, where the former corresponds to 1 ms and the latter to 2 ms. Overall, the throttle variations are smooth, except for one peak at the 31st second of flight 1, and three peaks in flight 2, causing a rapid change in the altitude. The peaks observed in the throttle time histories could be a result of interference between the ultrasonic sensor and the antenna of the radio receiver – the antenna’s movements created an echo in the ultrasonic sensor.

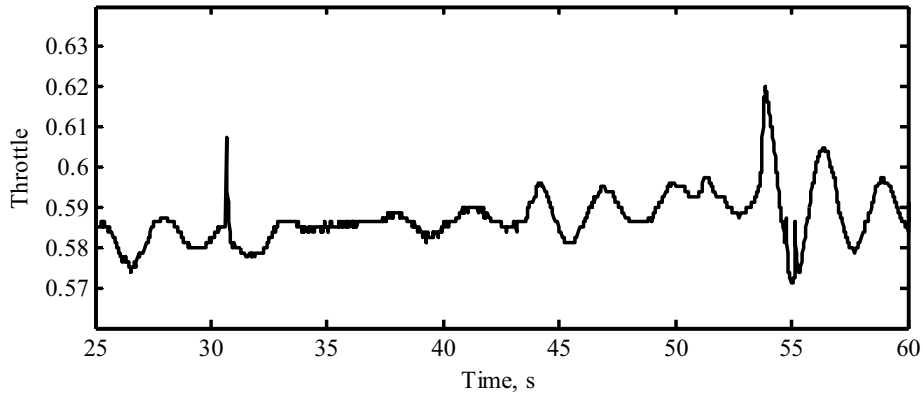


Fig. 8 Throttle time history for flight 1.

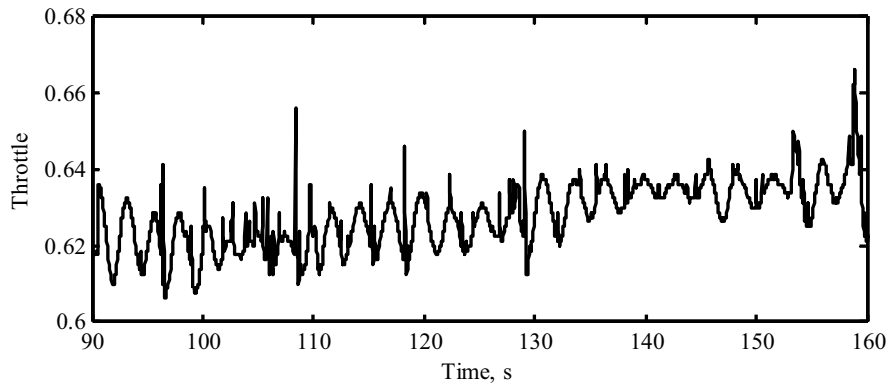


Fig. 9 Throttle time history for flight 2.

In the present test flights, the pilot was in the loop, controlling the attitude of the aircraft. Observed noise in the pitch, yaw, and roll gyros is shown in Figs. 10-12 for flight 1. The average amplitude of oscillation in the pitch and yaw axis is about 0.1 rad/s. For the roll, it is about 0.2 rad/s. Higher oscillations in roll can be explained by lower inertia, I_{xx} (see Table 2).

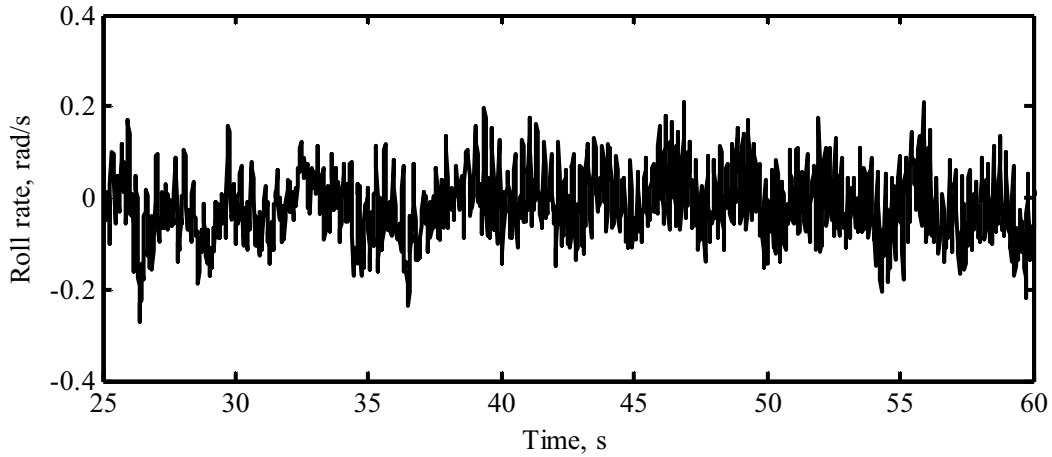


Fig. 10 Roll rate vs. time.

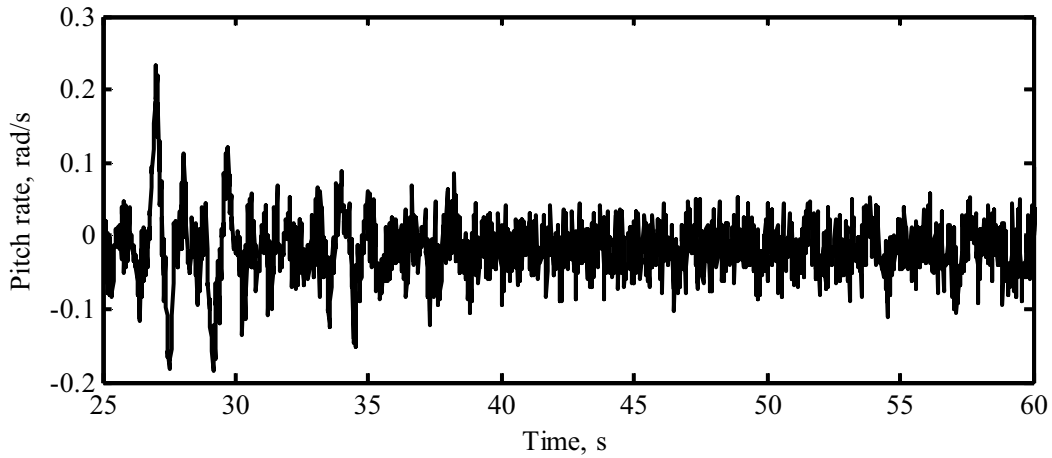


Fig. 11 Pitch rate vs. time.

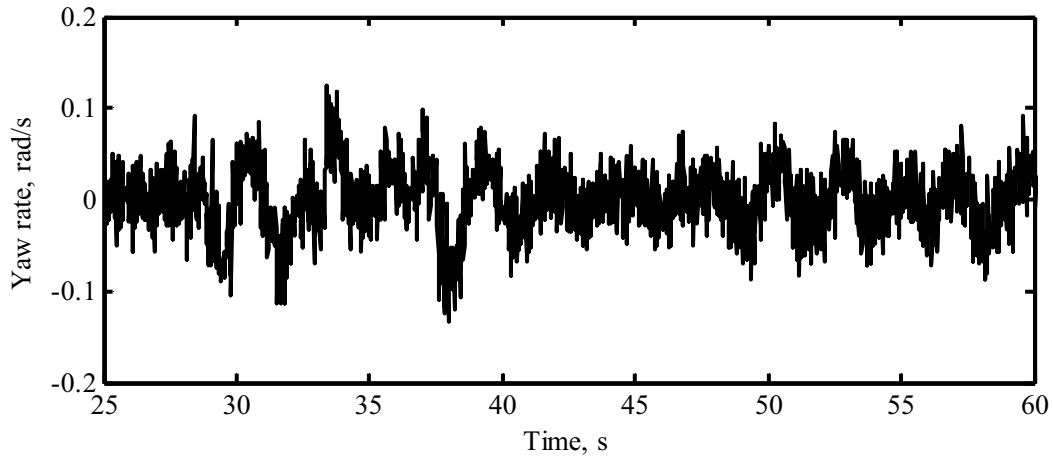


Fig. 12 Yaw rate vs. time.

Recorded data on roll, pitch, and yaw rates were analyzed using the fast Fourier transform algorithm in Matlab[®]. Plots of frequency spectra are presented in Figs. 13-15. A low frequency peak at 1-3 Hz corresponds to the bandwidth of the feedback dynamics. Other peaks can be seen in the 2-25 Hz range of the pitch and yaw rates. At this time, the source of vibrations remains unknown, but it warrants future related studies.

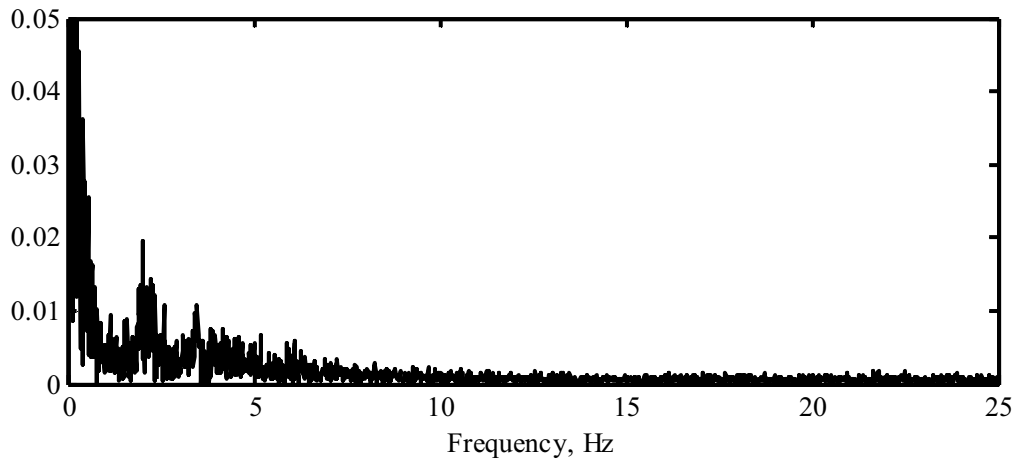


Fig. 13 Frequency spectrum for roll rate.

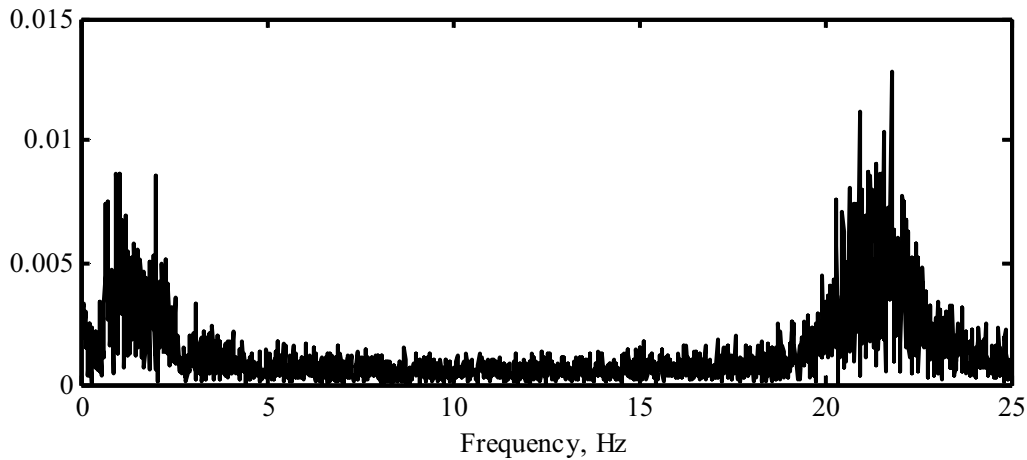


Fig. 14 Frequency spectrum for pitch rate.

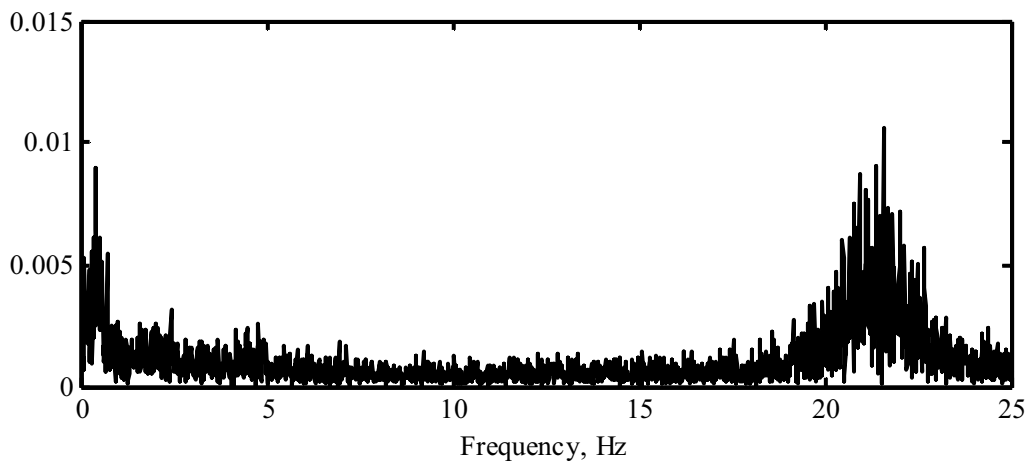


Fig. 15 Frequency spectrum of yaw rate.

B. Mini-Vertigo

The stability augmentation mode of the autopilot was employed in the flight testing of the Mini-Vertigo. In this mode, the pilot can accurately introduce the desired value of attitude, then the autopilot generates control commands for the control surfaces to hold the airplane at the desired altitude. The two gain sets used in altitude controls correspond to initial (set 1) and final tuning (set 2). The time series of the altitude of the aircraft measured during the flights for the two sets of control gain coefficients are shown in Figs. 16 and 17, and the corresponding throttle histories are shown in Figs. 18 and 19.

The low value of the hovering throttle gain in set 1 produced a slow response in altitude, which resulted in a low climb rate of the aircraft until it reached the commanded altitude. Also in set 1, the proportional and derivative gains were higher than in set 2 and as a result, the amplitude of the oscillations of the aircraft in altitude were about 0.2 m compared to 0.1 m for set 2. The response of the aircraft to changes of desired altitude for set 2 is also faster than that for set 1. When desired altitude was changed by about 0.1 m, the measured altitude changed in about 2 s, at times of 6-8 s and 16-18 s. This test could not be performed for set 1 due to sluggish response of the aircraft.

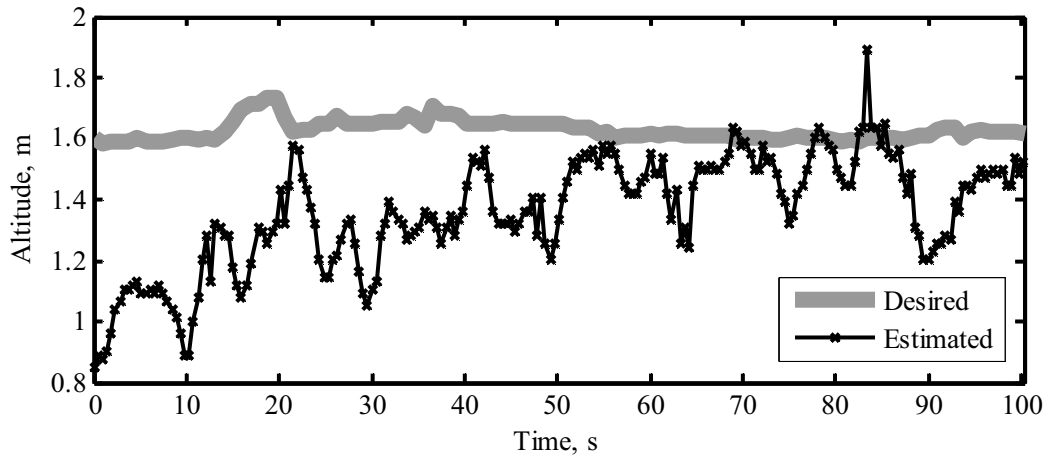


Fig. 16 Measured and desired altitudes of the Mini-Vertigo for flight 1.

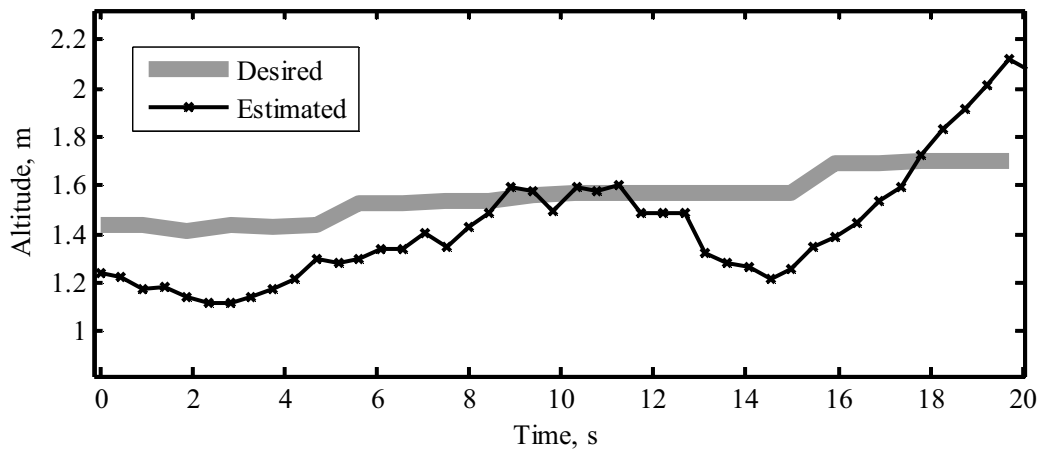


Fig. 17 Measured and desired altitudes of the Mini-Vertigo for flight 2.

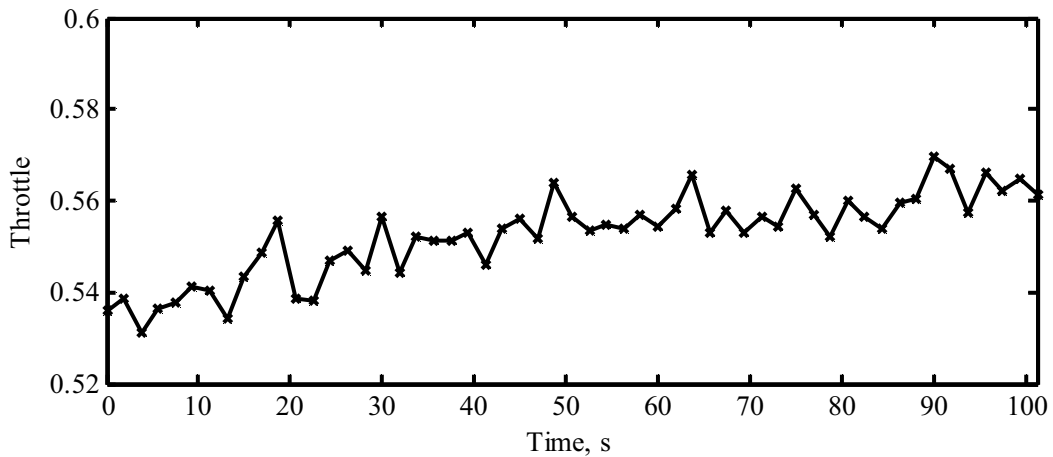


Fig. 18 Throttle command for flight 1.

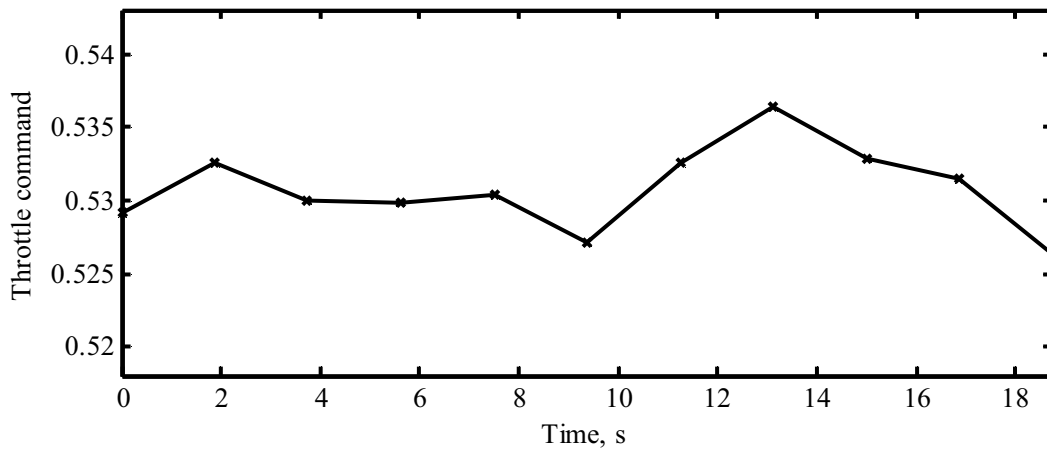


Fig. 19 Throttle command for flight 2.

Angular velocities of the Mini-Vertigo aircraft, estimated using on-board gyroscopes, are shown in Figs. 20-22 for control gain set 1. Average amplitudes of oscillation were found: 0.2 rad/s for roll and less than 0.1 for pitch and yaw. It is interesting to note that these values are very close, both qualitatively and quantitatively, to those obtained for the Vertigo.

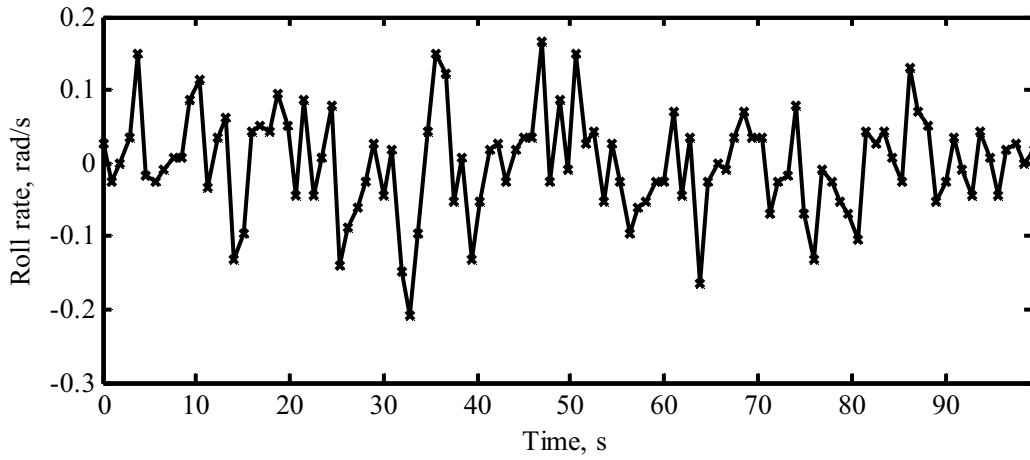


Fig. 20 Roll rate vs. time.

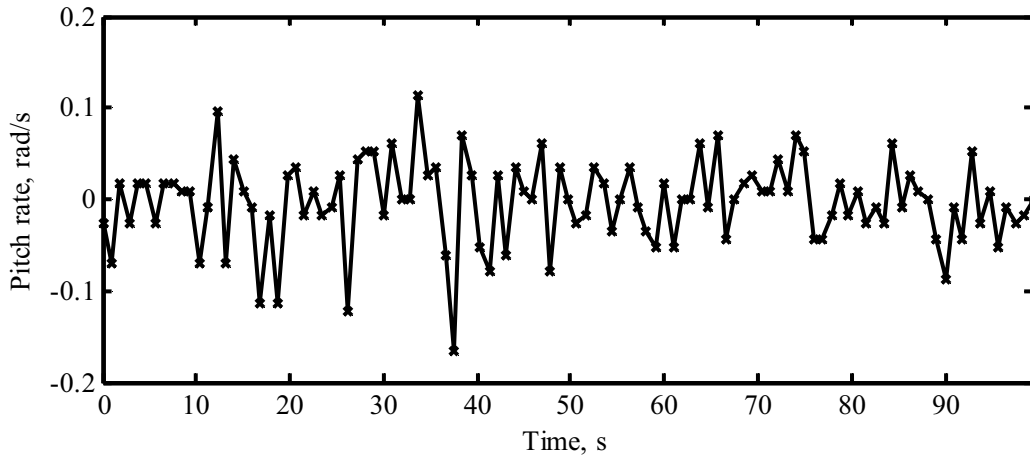


Fig. 21 Pitch rate vs. time.

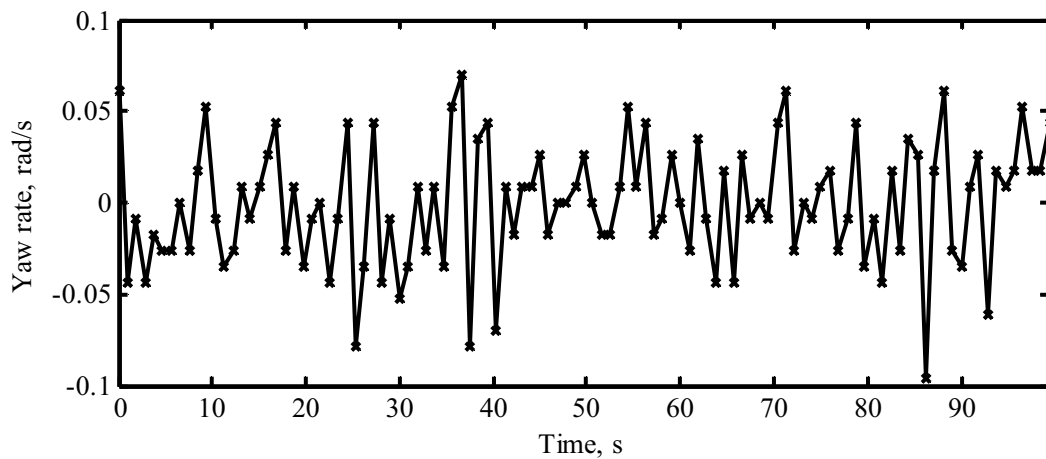


Fig. 22 Yaw rate vs. time.

V. Concluding Remarks

Recent studies have demonstrated the high flying qualities of VTOL MAVs. The present work describes the development of an automatic control system and the investigation of the flight dynamics of these aerial vehicles, specifically, for the hovering phase of the flight.

The design approach presented in this paper includes the integration of an autopilot into an aircraft, development of equations of motion, simulation of flight dynamics, and a closed-loop control design. Effects of propeller slipstream impinging on the airframe are discussed in the context of control design. PID control laws were developed and programmed into the autopilot.

The development and evaluation of two autonomous micro air vehicles, the Vertigo and Mini-Vertigo, are presented. In a series of flight tests, the PID controls were adjusted and telemetry data on control actuation, altitude, and attitude were collected for the analysis and validation of predicted designs. Significant similarities were noted in the dynamic responses of both aircraft. Obtained results revealed a negative feature of the altitude hold - the lag between desired and measured altitudes caused by the delay in the propulsion system (speed controller-motor-propeller). Average amplitudes of oscillations in all three axes were also about the same for both aircraft. Higher roll rates can be explained by lower inertia in roll axis.

VI. Acknowledgments

This project represents collaborative efforts of the University of Arizona and ISAE towards the development of VTOL MAV technologies. It was sponsored by grants from the AFRL, Eglin AFB (Program Manager Dr. Gregg Abate), to the University of Arizona and by EOARD, London (Program Manager Dr. Surya Surampudi), to the ISAE. The authors also would like to thank Prof. Jean-Marc Moschetta of ISAE for his contributions to the aerodynamic design of the aircraft and Dominique Bernard for the construction of the Vertigo aircraft.

References

- ¹ Poinot, D., Lamaison, J., Hostallier, A., and Bérard, C., "Conception of an UAV Generic Mission System," *25th ICAS Congress*, 3-8 September 2006, Hamburg, Germany.
- ² Shkarayev, S., Moschetta, J.-M., and Bataillé, B., "Aerodynamic Design of VTOL Micro Air Vehicles," *Proceedings of the 3rd US-European Competition and Workshop on Micro Air Vehicle Systems, (MAV'07)*, September 17-21, 2007, Toulouse, France.
- ³ Moschetta, J.-M., Bataillé, B., Thipyopas, C., and Shkarayev, S., "On Fixed-Wing Micro-Air Vehicles with Hovering Capabilities," *46th Aerospace Sciences Meeting and Exhibit*, Reno, NV, January 7-10, 2008, AIAA-2008-0221.
- ⁴ McCormick, B. W. Jr., *Aerodynamics of V/STOL Flight*, Dover Publications, Inc., Mineola, NY, 1999.
- ⁵ Kohlman, D., *Introduction to V/STOL Airplanes*, Iowa State University Press, Ames, IA, 1981.
- ⁶ Foster, T. M., and Bowman, W. J., "Dynamic Stability and Handling Qualities of Small Unmanned-Aerial-Vehicles," *43rd AIAA Aerospace Sciences Meeting and Exhibit*, January 10-13, 2005, Reno, NV, AIAA-2005-1023.
- ⁷ Military Specification, Flying Qualities of Piloted Airplanes, MIL-F-8785C, Department of Defense Military Specifications and Standards, U.S. Department of Defense, Philadelphia, PA, 1980.
- ⁸ Waszak, M. R., Jenkins, L. N., and Ifju, P., "Stability and Control Properties of an Aeroelastic Fixed Wing Micro Aerial Vehicle," *AIAA Atmospheric Flight Mechanics Conference*, August 6-9, 2001, Montreal, Canada. AIAA-2001-4005.
- ⁹ Ifju, P. G., Jenkins, D. A., Ettinger, S., Lian, Y., Shyy, W., and Waszak, M. R., "Flexible-Wing-Based Micro Aerial Vehicles," *40th AIAA Aerospace Sciences Meeting and Exhibit*, January 14-17, 2002, Reno, NV. AIAA-2002-0705.
- ¹⁰ Drouin, A., and Brisset, P., "Paparaziy: DoItYourself UAV," *4th European Micro-UAV Meeting*, Toulouse, France, Sept. 15-17, 2004.
- ¹¹ Dixon, R., *Open Source Software Law*, Artech House, Boston, MA, 2004, pp. 287-288.
- ¹² Platanitis, G. and Shkarayev, S., "Integration of an Autopilot for a Micro Air Vehicle," *Infotech@Aerospace*, September 26-29, 2005, Arlington, VA, AIAA-2005-7066.
- ¹³ Taylor, B., Bil, C., Watkins, S., "Horizon Sensing Attitude Stabilisation: A VMC Autopilot," *18th International UAV Systems Conference*, Bristol, UK, 2003.
- ¹⁴ Arning, R.K., and Sassen, S., "Flight Control of Micro Aerial Vehicles," *AIAA Guidance, Navigation, and Control Conference and Exhibit*, August 16-19, 2004, Providence, RI, AIAA 2004-4911.

¹⁵ Millet, T., Yates, J., Millar, B., and Johnson, N., “Brigham Young University MAV Team,” *3rd US-European Micro Air Vehicle Competition*, Toulouse, France, September 2007.

¹⁶ “Development of Flexible Wing Autonomous MAV,” University of Florida Micro Air Vehicle Laboratory, *3rd US-European Micro Air Vehicle Competition*, Toulouse, France, September 2007.

¹⁷ Quix, H., Alles, W., “Design and Automation of Micro Air Vehicles,” *1st European Micro Air Vehicle Conference and Flight Competition*, EMAV 2004, 13-14 July 2004, Braunschweig, Germany.

¹⁸ Chung, D.K., Ryu, J.H., Nam, I.C., Jo, K.Y., Yoon, K.J., Huang, H.C., and Kim, J.H., “Development of Fixed Wing MAV Batwing at Konkuk University,” *9th International Micro Air Vehicle Competition*, 2005, Konkuk University, Seoul, South Korea.

¹⁹ Stone, R. H., Anderson, P., Hutchison, C., Tsai, A., Gibbens, P. and Wong, K. C. , “Flight Testing of the T-Wing Tail-Sitter Unmanned Air Vehicle”, *Journal of Aircraft*, Vol. 45, No. 2, March–April 2008.

²⁰ N. B. Knoebel, S. R. Osborne, D. O. Snyder, T. W. McLain, R. W. Beard, A. M. Eldredge “Preliminary Modeling, Control, and Trajectory Design for Miniature Autonomous Tailsitters,” *AIAA Guidance, Navigation, and Control Conference Proceedings*, 2006.

²¹ Krashanitsa, R., Platanitis, G., Silin, D., and Shkarayev, S., “Autopilot Integration into Micro Air Vehicles,” *Introduction to the Design of Fixed-Wing Micro Aerial Vehicles*, edited by T. J. Mueller, J. C. Kellogg, P. G. Ifju and S. Shkarayev, AIAA, Reston, VA, 2006.

²² Krashanitsa, R., Platanitis, G., Silin, B., and Shkarayev, S., “Aerodynamics and Controls Design for Autonomous Micro Air Vehicles,” *AIAA Atmospheric Flight Mechanics Conference and Exhibit*, 21-24 August 2006, Keystone, Colorado, AIAA 2006-6639.

²³ Kajiwara, I., and Haftka, R. T., “Simultaneous Optimum Design of Shape and Control System for Micro Air Vehicles,” *30th Plasmadynamics and Lasers Conference*, June-July 1999, Norfolk, AIAA 99-1391.

²⁴ Poinot, D., Bataille, B., Piquereau, A., and Berard, C., “Fixed wings MAV controlled by deflection of airflow in a hover flight phase,” EMAV 2006. Braunschweig, Germany, 25 - 26 July 2006.

²⁵ Bataille, B., Poinot, D., Moschetta, J-M., and Piquereau, A., “Development of a Fixed Wing VTOL Mini UAV,” AIAA IPLC-2008, 22-24 July 2008, London.

²⁶ Özbay, H., *Introduction to Feedback Control Theory*, CRC Press LLC, Boca Raton FL , 2000.

²⁷ Ziegler, J.G., and Nichols, N.B., “Optimum Settings for Automatic Controllers,” *Trans. ASME*, 64, 1942, 759-768.

Appendix 4

Dynamic Model and System Identification Procedure for Autonomous Ornithopter

This page intentionally left blank

Dynamic Model and System Identification Procedure for Autonomous Ornithopter

Bharani P. Malladi,¹ Roman Y. Krashanitsa,² Dmitry Silin,³ and Sergey V. Shkarayev⁴
University of Arizona, Tucson, Arizona, 85721, USA

The study presented in this paper focuses on the development of a dynamic model for the flapping-wing air vehicle (ornithopter) and on the model parameters identification for this vehicle using in-flight data. The proposed dynamic model combines the flapping wings motion with the motion of the ornithopter's center of mass. A set of six equations in the integral form was obtained for the motion of the center of mass of the ornithopter. The aerodynamic forces acting on the wing during one full stroke are presented as a sum of stroke-averaged forces, acting during upstroke and downstroke. The dynamic model is linearized with respect to the state variables and the equations of motion are obtained for longitudinal mode in state-space form. Parameters of the linearized model are conventional stability and control derivatives. The system identification procedure is proposed based on a value of a scalar objective function in the least square sense. A 100-cm ornithopter was built and equipped with the autopilot. The ornithopter was used to gather experimental data in-flight. Preliminary experimental results on flight dynamics of the ornithopter are presented and discussed.

Keywords: ornithopter, stability, control, model, experiment, system identification.

Nomenclature

A, B, C, D	= state-space model operators
\bar{a}	= acceleration vector
b	= wingspan
b_T	= span of tail
C_D	= drag coefficient
C_L	= lift coefficient
C_{m^*}	= pitching moment coefficient derivatives
C_m	= pitching moment coefficient
\bar{c}	= wing mean geometric chord
\bar{c}_T	= tail mean geometric chord
c_R	= root chord
f	= flapping frequency
F_a	= aerodynamic force
F_g	= gravitational force
\bar{F}	= force vector
f_i	= internal force
G	= inertia matrix of the wing

¹ Research Assistant, Dept. of Aerospace and Mechanical Engineering, 1130 N. Mountain Ave.

² Research Assistant Professor, Dept. of Aerospace and Mechanical Engineering, 1130 N. Mountain Ave.

³ Research Assistant, Dept. of Aerospace and Mechanical Engineering, 1130 N. Mountain Ave.

⁴ Associate Professor, Dept. of Aerospace and Mechanical Engineering, 1130 N. Mountain Ave.

L_W, L_B, L_T	= lift force of wing, body, and tail, respectively
M	= pitching moment
M_A	= aerodynamic pitching moment
\bar{M}	= moment of force vector
m	= mass
q	= pitch rate
\bar{q}	= mean dynamic pressure
\bar{r}	= radius-vector
\mathbf{R}	= rotation matrix
Re	= Reynolds number
S	= wing planform area
S_T	= tail planform area
T	= flapping period
u	= perturbed horizontal velocity
\mathbf{u}	= control vector
\bar{U}	= instantaneous velocity of the blade element
\bar{v}	= velocity vector
w	= perturbed vertical velocity
\mathbf{x}	= state vector
α	= angle of attack
$\dot{\alpha}$	= angle of attack rate of change
β	= wing elevation angle
β_T	= tail installation angle
δ_e	= elevator deflection
φ	= roll angle
γ	= wing rotation angle
θ	= pitch angle
θ_T	= tail installation angle
ζ_W	= wing lead-lag angle
ψ	= yaw angle
$\bar{\omega}$	= angular velocity vector

Superscripts

B	= with respect to the body
T	= with respect to the tail
TO	= total
W	= with respect to the wing

Subscripts

a	= aerodynamic
B	= with respect to the body
E	= with respect to the earth-fixed coordinate frame
g	= gravitational
T	= with respect to the tail
TO	= total
tr	= reaction
W	= with respect to the wing

I. Introduction

Studies on biological flight employ complex data acquisition equipment, both stationary, such as high-speed video cameras, and mounted on the subjects, including sensors acquiring data about trajectories, air pressure, and velocity fields during the flapping flight. Some of notable works in this field were completed by Willmott and Ellington¹ on the kinematics of the flight of hawkmoth *Manduca Sexta* using two high-speed video cameras. The study revealed the mechanics of the body motion and the range of wing flapping and feathering angles during flight.

Pennycuick and Lock² studied energy storage in pigeon wings during upstroke and downstroke for hovering and slow forward flights. The authors estimated the stored energy and its effect on the shape of the wake.

Azuma et al.³ employed the blade theory to model and quantify the aerodynamics of wings of such insects as dragonflies and damselflies and to investigate the effect of increased lift during the downstroke due to dynamic stall. Comparison of the results of the study with experimental data was done qualitatively.

Larijani et al.⁴ obtained experimental data on a static flapping and taxiing of a full-scale ornithopter and two quarter-scale models. No real flight data were provided. The ornithopter models featured a thick airfoil wing composed of a rigid and a flapping part. The numerical study was conducted featuring both structural and aerodynamic analysis. The finite element discretization broke the wing structure into elements with torsional and bending degree of freedom and a classical Galerkin method was applied using a set of linear interpolation functions to form a system of dynamic equations. A modified strip theory was used, whereas vortex wake effects were accounted for, as well as partial leading edge suction and post-stall behavior. This model was used for the calculation of average lift, thrust, power required, and propulsive efficiency of a flapping wing in a steady flight. The maximum error in the results of modeling compared to the experimental results associated with bending moment data was 15% and that for twisting moment data was about 20%. These predictions are interesting, considering the low quality of the experimental data and simple numerical models used.

Frampton et al.⁵ experimentally investigated an articulation of one degree of freedom wing and the effect of translational and rotational motion of the wing on the generated thrust. Translational and rotational motions of the wing were achieved through elastic bending and twisting of the wing in phase or out of phase, depending on the excitation frequency. Thrust-to-power ratios and efficiency parameters were determined. Initial results indicated that a wing, exhibiting bending and torsional motion in phase, generates the larger thrust, whereas a wing with torsional motion lagging the bending motion by 90 degrees results in a better power efficiency.

The primary objective of the present study is to develop a dynamic model of a flapping-wing air vehicle and to estimate parameters of the model using in-flight telemetry data.

II. Statement of Problem and Assumptions

As with any other flying machine the ornithopter obeys the same set of physics laws, so the classical approach to derive and solve the equations of motion may be applied. At the same time, there are some important features, arising from the wing's flapping motion, to be taken into account. For simplicity, the following assumptions are made in the development of the dynamic model:

- The ornithopter is made of several moving solid bodies of constant mass.
- Only flight in the vertical plane is considered.

The wings have a planform area, S , and wingspan, b . The wings are fixed to the fuselage at the leading edge symmetrically with respect to the fuselage plane (see Fig. 1). They perform flapping or up-and down motion by changing the flapping or elevation angle, β , the rotation or wing pitching angle, γ , and the lead-lag or forward-backward angle, ζ , as shown in Fig. 1. The v-tail consists of two parts, and the orientation of each part is defined with respect to the fuselage axis by two angles: β_T and θ_T . The v-tail has a triangular planform with area S_T and span b_T . Orientation of the fuselage with the tail is fully defined by the roll, ϕ , pitch, θ , and yaw, ψ angles, as described by Roskam⁶ and Etkin and Reid.⁷

The geometrical relationships between the coordinate frames used in this study are explained below. The inertial orthogonal frame (X_E, Y_E, Z_E) , with the origin O_E is fixed to the Earth. An orthogonal frame (X, Y, Z) with origin G at the center of mass of the aircraft is a body-fixed system (Fig. 1). The following expression holds:

$$\begin{pmatrix} X_E \\ Y_E \\ Z_E \end{pmatrix} = \mathbf{R}_1 \begin{pmatrix} X \\ Y \\ Z \end{pmatrix} + \bar{r}_G$$

where \mathbf{R}_1 is the body-fixed orthogonal rotation matrix by Euler angles ϕ , θ , and ψ .

The wing-fixed coordinate system (x_w, y_w, z_w) is defined using vector transformation

$$\begin{pmatrix} X \\ Y \\ Z \end{pmatrix} = \mathbf{R}_w \begin{pmatrix} x_w \\ y_w \\ z_w \end{pmatrix} + \bar{r}_{O_w, G}$$

where \mathbf{R}_w is the body-fixed orthogonal rotation matrix by elevation, lead-lag, and rotation angles.

We define the coordinate system for the tail in a similar way. Define the radius-vector from the center of mass to the point of fixture of the tail as $\bar{r}_{O_r, G}$. Then, transformation of the tail coordinate system (x_T, y_T, z_T) with respect to the coordinate system (X, Y, Z) is defined by

$$\begin{pmatrix} X \\ Y \\ Z \end{pmatrix} = \mathbf{R}_T \begin{pmatrix} x_T \\ y_T \\ z_T \end{pmatrix} + \bar{r}_{O_r, G}$$

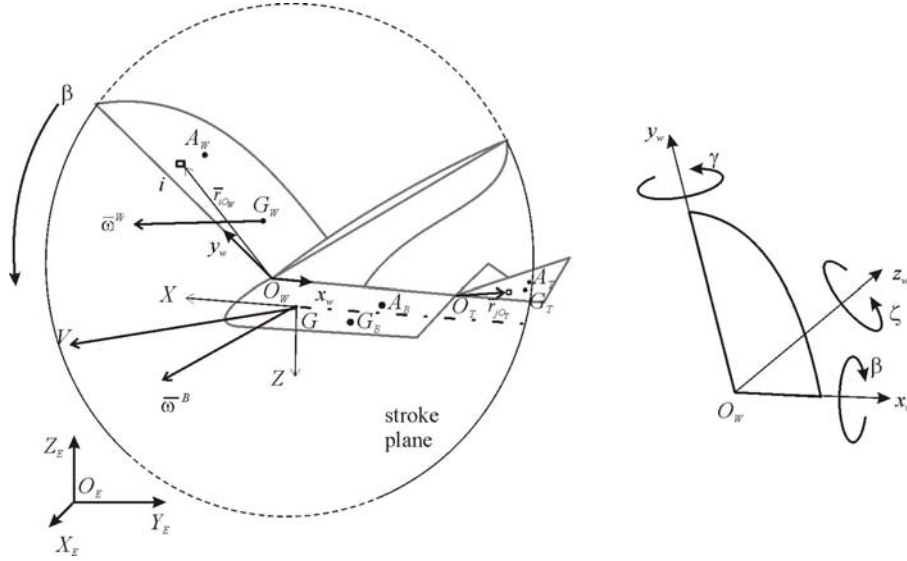


Fig. 1. Ornithopter geometry.

The following forces act on the ornithopter: wing lift, L_w , drag, D_w , and pitching moment, M_w ; tail lift, L_T , drag, D_T , and pitching moment, M_T . Define the aerodynamic forces in terms of aerodynamic coefficients, dynamic pressure, \bar{q} , and wing area, S as:

$$L_w = \bar{C}_L^w \bar{q} S, \quad D_w = \bar{C}_D^w \bar{q} S, \quad M_w = \bar{C}_m^w \bar{q} S \bar{c}, \quad L_T = C_L^T \bar{q} S_T, \quad D_T = C_D^T \bar{q} S_T, \quad M_T = C_m^T \bar{q} S \bar{c}$$

Derive the dynamic equations of motion for the center of mass of the ornithopter. Consider a small element of the wing, i (Fig. 1). Define the position vector of the wing element, i , as

$$\bar{r}_i = \bar{r}_G + \bar{r}_{O_w, G} + \bar{r}_{i, O_w} \quad (1)$$

or using the coordinate system transformation

$$\bar{r}_i = \bar{r}_G + \mathbf{R}_1 (\bar{r}_{O_w})_{XYZ} + \mathbf{R}_1 \mathbf{R}_w (\bar{r}_{i, O_w})_{x_w y_w z_w} \quad (2)$$

Differentiating twice and multiplying Eq. (2) by the mass of the element, dm , to write the equation of motion

$$dm_w \ddot{\bar{r}}_G + dm_w \ddot{\mathbf{R}}_1 (\bar{r}_{O_w})_{XYZ} + dm_w \frac{d^2}{dt^2} (\mathbf{R}_1 \mathbf{R}_w) (\bar{r}_{i, O_w})_{x_w y_w z_w} = \Delta F_a^w + \Delta F_g^w + f_i^w \quad (3)$$

where ΔF_a^W is aerodynamic force, f_i^W is internal force, and ΔF_g^W is gravitational force acting on one element of the wing. Integrate over the total area of the half-wing and multiply by two, since there is two halves of the wing

$$m_W \ddot{\bar{r}}_G = 2\bar{F}_a^W + 2\bar{F}_{ir}^W + 2\bar{F}_g^W - 2 \int_W \left(\ddot{\mathbf{R}}_1(\bar{r}_{O_w})_{XYZ} + \frac{d^2}{dt^2}(\mathbf{R}_1 \mathbf{R}_W)(\bar{r}_{iO_w})_{x_w y_w z_w} \right) dm_W \quad (4)$$

where $\Delta F_{ir,W}$ are reaction forces.

Obtain the equation of motion for the tail in a similar manner

$$m_T \ddot{\bar{r}}_G = 2\bar{F}_a^T + 2\bar{F}_{ir}^T + 2\bar{F}_g^T - 2 \int_T \left(\ddot{\mathbf{R}}_1(\bar{r}_{O_T})_{XYZ} + \frac{d^2}{dt^2}(\mathbf{R}_1 \mathbf{R}_T)(\bar{r}_{iO_T})_{x_T y_T z_T} \right) dm_T \quad (5)$$

The external forces acting on the fuselage are the aerodynamic force, gravitational force, reaction force from the wings, and reaction force from the tail. Then the dynamic equation of motion for the fuselage body is

$$m_B \ddot{\bar{r}}_G = \bar{F}_a^B - 2\bar{F}_{ir}^T - 2\bar{F}_{ir}^W + \bar{F}_g^B \quad (6)$$

Assume that the aerodynamic forces generated by the fuselage of the ornithopter are small compared to that generated by the wing and tail, and can therefore be disregarded. Summing Eqs. (4), (5), (6) gives the equations of translational motion for the center of mass of the ornithopter

$$\begin{aligned} m_{TO} \ddot{\bar{r}}_G &= 2\bar{F}_a^T + 2\bar{F}_a^W + \bar{F}_g^{TO} - 2 \int_W \left(\ddot{\mathbf{R}}_1(\bar{r}_{O_w})_{XYZ} + \frac{d^2}{dt^2}(\mathbf{R}_1 \mathbf{R}_W)(\bar{r}_{iO_w})_{x_w y_w z_w} \right) dm_W \\ &- 2 \int_T \left(\ddot{\mathbf{R}}_1(\bar{r}_{O_T})_{XYZ} + \frac{d^2}{dt^2}(\mathbf{R}_1 \mathbf{R}_T)(\bar{r}_{iO_T})_{x_T y_T z_T} \right) dm_T \end{aligned} \quad (7)$$

Next, form the moment of forces about the center of mass of the ornithopter. Derive expressions for moments of each part of the ornithopter about its center of mass and sum them. The general form of the sum of moments acting on the element of the wing, i , about the center of mass of the ornithopter is

$$\left(\bar{M}_G^W \right)_i = \bar{r}_{iG} \times \left[\bar{F}_i + \sum_{\substack{i=1 \\ i \neq j}}^N \bar{f}_{ij} \right] = \bar{r}_{iG} \times m_i \bar{a}_i \quad (8)$$

where \bar{F}_i are external, and \bar{f}_{ij} are internal forces acting on the element. Acceleration of the wing element is

$$\bar{a}_i = \bar{a}_G + \bar{a}_{iG} = \bar{a}_G + \frac{d\bar{v}_{iG}}{dt} \quad (9)$$

defined in the (X_E, Y_E, Z_E) coordinate system. Summation over all wing elements gives

$$\bar{M}_G^W = \sum_N \bar{r}_{iG} \times m_i \bar{a}_i = m_W \bar{r}_{G_w,G} \times \bar{a}_G + \dot{\bar{H}}_G^W \quad (10)$$

where

$$\dot{\bar{H}}_G^W(t) \equiv \frac{d}{dt}(\mathbf{G}(t)\bar{\omega}(t)) = \dot{\mathbf{G}}(t)\bar{\omega}(t) + \mathbf{G}(t)\dot{\bar{\omega}}(t) + \bar{\omega}(t) \times \mathbf{G}(t)\bar{\omega}(t) \quad (11)$$

and $\mathbf{G}(t)$ is the inertia matrix of the wing with respect to the center of mass of the aircraft.

In a similar manner, the moment equation for the tail is a summation over M elements of the tail

$$\bar{M}_G^T = \sum_M \bar{r}_{jG} \times m_j \bar{a}_j = m_T \bar{r}_{G_T G} \times \bar{a}_G + \dot{\bar{H}}_G^T \quad (12)$$

And, finally, for the fuselage

$$\bar{M}_G^B = \bar{r}_{A_B G} \times \bar{F}_a^B = m_B \bar{r}_{G_B G} \times \bar{a}_G + \dot{\bar{H}}_G^B \quad (13)$$

where \bar{F}_a^B is the aerodynamic force acting on the fuselage applied at the aerodynamic center of the body, A_B .

The sum of the moments about the center of mass of the ornithopter yields

$$\bar{M}_G^W + \bar{M}_G^T + \bar{M}_G^B = m_w \bar{r}_{G_w G} \times \bar{a}_G + \dot{\bar{H}}_G^W + \bar{r}_{G_T G} \times \bar{a}_G + \dot{\bar{H}}_G^T + \bar{r}_{G_B G} \times \bar{a}_G + \dot{\bar{H}}_G^B \quad (14)$$

where

$$\bar{M}_G^W = \bar{r}_{A_w G} \times \bar{F}_a^W + \bar{r}_{G_w G} \times \bar{F}_g^W + \bar{M}_{A_w}^W \quad (15)$$

$$\bar{M}_G^T = \bar{r}_{A_T G} \times \bar{F}_a^T + \bar{r}_{G_T G} \times \bar{F}_g^T + \bar{M}_{A_T}^T \quad (16)$$

$$\bar{M}_G^B = \bar{r}_{A_B G} \times \bar{F}_a^B + \bar{r}_{G_B G} \times \bar{F}_g^B + \bar{M}_{A_B}^B \quad (17)$$

and $\bar{M}_{A_w}^W$, $\bar{M}_{A_T}^T$, and $\bar{M}_{A_B}^B$ are aerodynamic moments, and \bar{F}_a^W , \bar{F}_a^T , and \bar{F}_a^B are aerodynamic forces applied at the aerodynamic centers of wing, fuselage, and tail of the ornithopter, respectively (see Fig. 1).

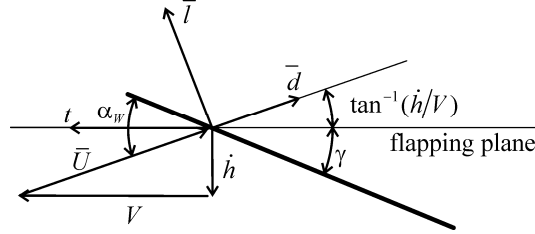


Fig. 2. Components of the aerodynamic forces.

Note that accelerations of the local coordinate systems (x_w, y_w, z_w) and (x_T, y_T, z_T) with respect to the (X, Y, Z) coordinate system are non-zero, since the position of the center of mass depends on the current orientation of the wing.

Present the total aerodynamic force acting on the right wing, \bar{F}_a^W , in a vector form

$$\bar{F}_a^W = \left(\int_0^{b/2} C_L(t, y) \frac{1}{2} \rho V(t, y)^2 c(y) dy \right) \bar{l} - \left(\int_0^{b/2} C_D(t, y) \frac{1}{2} \rho V(t, y)^2 c(y) dy \right) \bar{d} \quad (18)$$

where \bar{l} and \bar{d} are unit vectors of the coordinate system momentary fixed to the wing, such that \bar{d} coincides with the instantaneous velocity vector for the current wing cross-section, and \bar{l} is perpendicular to the velocity vector (Fig. 2).

In order to employ better control over the wing geometry during the flapping motion, define average lift, \bar{C}_L , and average drag, \bar{C}_D , coefficients for upstroke and downstroke. According to the blade theory, the mean lift, and drag coefficients for upstroke and downstroke are obtained as a solution of the system of linear equations, where each equation is formed for each of the experimental values of the aerodynamic force averaged for the flapping period

$$\bar{F}_a^W T = \bar{C}_L^u \int_0^{1/2} q(t) \bar{l} dt + \bar{C}_L^d \frac{1}{2} \rho \int_{1/2}^1 q(t) \bar{l} dt - \bar{C}_D^u \frac{1}{2} \rho \int_0^{1/2} q(t) \bar{d} dt - \bar{C}_D^d \frac{1}{2} \rho \int_{1/2}^1 q(t) \bar{d} dt \quad (19)$$

where the u superscript stands for upstroke and the d superscript stands for downstroke, T is a stroke period, and

$$q(t) = \frac{1}{2} \rho \int_0^{b/2} V(t, y)^2 c(y) dy$$

is the instantaneous dynamic pressure.

Define an average angle of attack, $\bar{\alpha}$ for the wing of the ornithopter as an angle between the fuselage centerline and the air stream velocity vector incident to the fuselage. Assume that the average lift and drag are functions of average angle of attack and rate of change of the angle of attack. Then, expand those values in Taylor series as

$$\bar{C}_L^u = \bar{C}_{L_\alpha}^u \bar{\alpha} + \bar{C}_{L_{\dot{\alpha}}}^u \dot{\bar{\alpha}} + \bar{C}_{L_{\delta_e}}^u \delta_e + \bar{C}_{L_E}^u E \quad (20)$$

$$\bar{C}_L^d = \bar{C}_{L_\alpha}^d \bar{\alpha} + \bar{C}_{L_{\dot{\alpha}}}^d \dot{\bar{\alpha}} + \bar{C}_{L_{\delta_e}}^d \delta_e + \bar{C}_E^d E \quad (21)$$

$$\bar{C}_D^u = \bar{C}_{D_{\min}}^u + K(\bar{C}_L^u)^2 \quad (22)$$

$$\bar{C}_D^d = \bar{C}_{D_{\min}}^d + K(\bar{C}_L^d)^2 \quad (23)$$

where E is the stiffness of the wing spar and K is a coefficient. In this way, wing lift coefficients for the up- and downstroke are additionally controlled through wing stiffness, effectively changing lift and drag forces to allow, in turn, longitudinal control of the aircraft.

The aircraft aerodynamic pitching moment, M_A , is defined as

$$M_A = C_m \bar{q} S \bar{c} \quad (24)$$

where C_m is the total aircraft aerodynamic pitching moment coefficient and M_A is a projection of the total moment $\bar{M}_G^W + \bar{M}_G^T + \bar{M}_G^B$ onto the Y -axis of the aircraft coordinate system. For an ornithopter with an elevator, the pitching moment coefficient is expressed in the form of a first-order Taylor series

$$C_m = C_{m_0} + C_{m_\alpha} \bar{\alpha} + C_{m_{\dot{\alpha}}} \dot{\bar{\alpha}} + C_{m_{\delta_e}} \delta_e \quad (25)$$

In order to study the dynamics of the ornithopter, a perturbed model for steady-state flight is needed, which will also be the nominal model used for controls design and analysis. From the aerodynamic forces and moments, the stability derivatives are obtained and the longitudinal equations of motion are cast into the following linear state-space model:

$$C_0 \dot{\mathbf{x}} = \mathbf{A} \mathbf{x} + \mathbf{B} \mathbf{u} \quad (26)$$

$$\dot{\mathbf{x}} = C_0^{-1} \mathbf{A} \mathbf{x} + C_0^{-1} \mathbf{B} \mathbf{u} \quad (27)$$

$$\dot{\mathbf{x}} = \mathbf{A}' \mathbf{x} + \mathbf{B}' \mathbf{u} \quad (28)$$

where \mathbf{x} is a state vector, \mathbf{u} is a control vector, and \mathbf{A} and \mathbf{B} are system matrices. The state vector for the longitudinal mode is $\mathbf{x} \equiv [u, w, q, \theta]^T$.

III. System identification

The solution to the inverse problem of dynamic system identification is found in a least-squares sense by minimizing the real-valued scalar objective function

$$\eta(s) = \int_{t_1}^{t_2} |x(s, \tau) - \tilde{x}(\tau)|^2 d\tau \quad (29)$$

where s is the current set of parameters for the state-space model (26), $x(s, \tau)$ is a state vector obtained as a solution of the direct problem for the current set of parameters, $\tilde{x}(\tau)$ represents the experimental data, and t_1 and t_2 are the time domain of integration. The algorithm proposed by Nelder and Mead⁸ is used for minimizing the objective function, $\eta(s)$, for $s \in \mathfrak{R}^n$. At the beginning of k^{th} iteration (where $k > 0$), a non-degenerate simplex, Δ_k , is given along with its $n+1$ vertices; each of the vertices is a point in \mathfrak{R}^n space. Each iteration generates a simplex that is different from the one generated during the previous iteration. Iterations continue until the characteristic size of the simplex is less than the threshold value. The Nelder-Mead algorithm is characterized by a rapid convergence at the first iteration and the Jacobian of the objective function is not required for the method.

IV. Experimental results and discussion

In order to be able to record in-flight telemetry data, and to control the ornithopter automatically, the ornithopter was equipped with a Paparazzi autopilot and software.⁹ Only a time history analysis and parameter estimation based on the telemetry data are presented here.

A. Autopilot integration into the 100-cm ornithopter

Utilizing previous experience in the autopilot integration,^{10,11} the Paparazzi autopilot was integrated into a 100-cm ornithopter in the present project. The ornithopter geometry data are listed in Table 1. For this project, a thin 0.8-mm autopilot controller printed circuit board with no connectors was manufactured. The ready-to-install autopilot board has dimensions of $7 \times 31.5 \times 63.5$ mm and 16.9 gram of weight.

Table 1. Ornithopter geometric data.

Parameter	Value
Wingspan	1 m
Wing Area	0.1571 m ²
Mass	369g
Wing root chord	200 mm

The Paparazzi autopilot and ground station are a set of software and hardware assets, flexible enough to work with various types of flying vehicles. The custom controller uses a Phillips ARM7 microprocessor, a built-in U-Blox GPS processor with an 18-mm patch antenna mounted on the controller PCB, and an infrared sensor board to determine the current attitude of the vehicle. A pair of X-Bee Pro wireless modems by Maxstream, Inc. provides a communication between the vehicle and the ground station.

The flight control software consists of several subsystems - configuration files, flight plan, map, autopilot, and GPS tools—and two major parts—the autopilot software on-board the airplane and the ground station software. In flight, the autopilot sends telemetry data back to the ground station. Currently, the telemetry data include: GPS-based data; speed, altitude, and climb rate of the airplane; attitude of the aircraft provided by infrared sensors; autopilot status data; and position of the control surfaces. These data play a major role in performance analyses during the flight tests and adjustments of gains.

Longitudinal control of the ornithopter is accomplished by proportional control for altitude hold, with an inner pitch attitude loop. Similarly, lateral-directional control is accomplished by an outer heading hold loop and the inner bank angle control loop, both using proportional control.

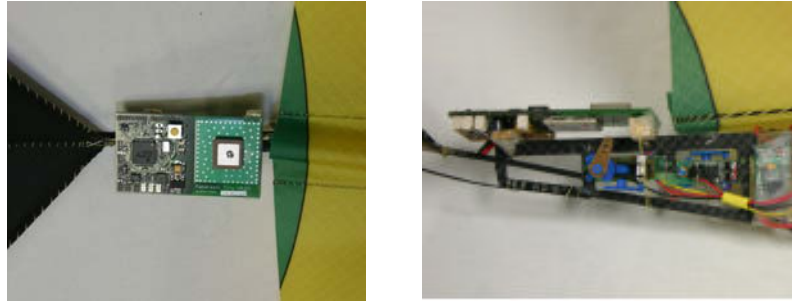


Fig. 3. Autopilot hardware integration in the 100-cm ornithopter.

The autopilot board was installed on the top of the frame right behind the wing (Fig. 3). In order to protect the board from vibrations, it was installed using two T-shaped mounts with soft rubber foam pads. All the radio control components are located right under the board in the frame cutouts, thus the weight of the wiring is also minimized.

Taking into account results of the flight tests for our previous ornithopters,¹² the current prototype has an increased area for the elevator, for better pitch control, and a smaller opening angle of the v-tail, for more efficient roll control. After necessary adjustments of the center of mass position, the ornithopter is able to withstand up to 3 m/sec wind, can do a series of sharp turns while maintaining altitude, and has a flight time at moderate throttle in excess of 7 min.

Flight tests using an autopilot showed good stability of the aircraft and enough maneuverability to do basic waypoint navigation in-plane and maintaining commanded altitude. Telemetry data were gathered by an in-flight data logging system built into the autopilot and transmitted to the ground station via a wireless link at the rate of 30-35 messages per second and stored in the ground station computer.

The flapping frequency of the ornithopter was estimated from the static measurements and presented in Table 2. The flapping frequency is measured using a digital tachometer HCAP0401.

Table 2. Static flapping frequencies.

Throttle setting	f (Hz)
25%	2-2.5
50%	4.5-5
75%	5.5-6
100%	7-7.5

B. Flight data analysis for longitudinal mode

The following is an example of the longitudinal flight parameter estimation carried out with actual flight data of the ornithopter. The time history data used in this analysis are the position of the ornithopter in terms of its trajectory points measured by the GPS unit and given as a set of three-dimensional vector components $\{X_E, Y_E, Z_E\}$. Orientation of the ornithopter in terms of pitch and roll angles were measured with respect to the horizontal plane. The trajectory followed by the ornithopter during the test flight is shown in Fig. 4.

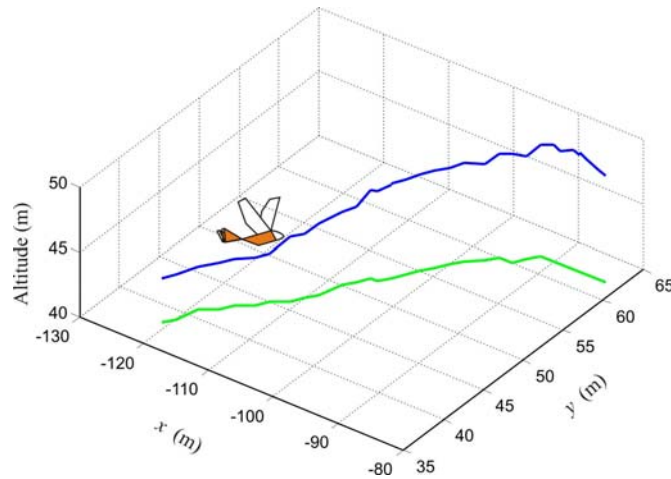


Fig. 4. Trajectory of the ornithopter.

The oscillatory response of the aircraft was analyzed during the “hands-off” flight tests. A typical response of the ornithopter during such a flight was recorded for 10 sec. There was no pilot input on the elevator and aileron controls during this time. The throttle was held constant at a cruise flight setting of 35%. Variation of the altitude during the flight is shown in Fig. 5. The flight altitude data were smoothed for the purpose of velocity calculations (Fig. 5). Measured climb rate for the duration of the test flight was no higher than 0.4 m/s. Variation of the airspeed, V , is shown in Fig. 6. Angle of attack variation was calculated from measured pitch, trajectory, and velocity, and presented in Fig. 7. Even though velocity and altitude of flight change slowly, the angle of attack (Fig. 7) and pitch values (Fig. 8) show significant oscillations.

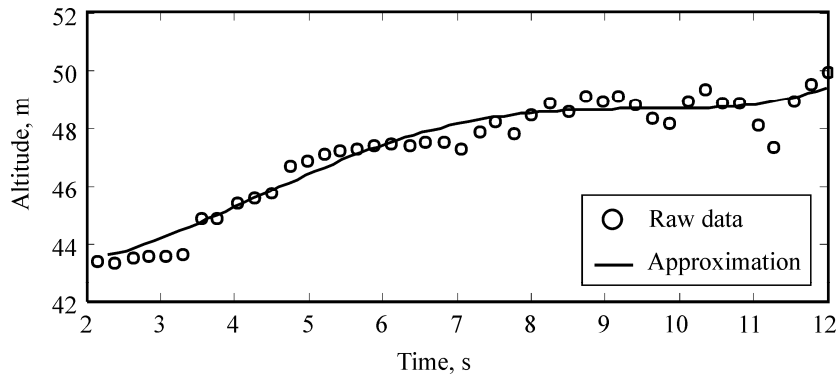


Fig. 5. Variation of altitude with time.

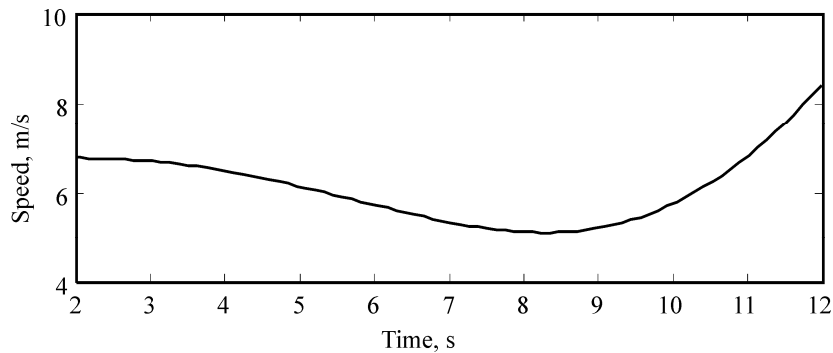


Fig. 6. Variation of speed with time.

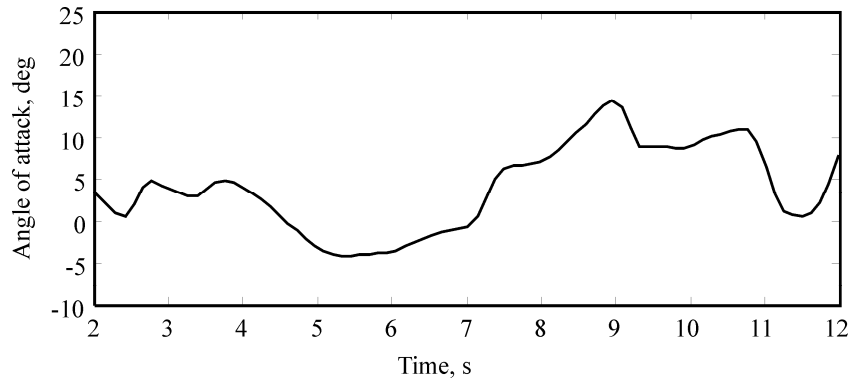


Fig. 7. Variation of angle of attack with time.

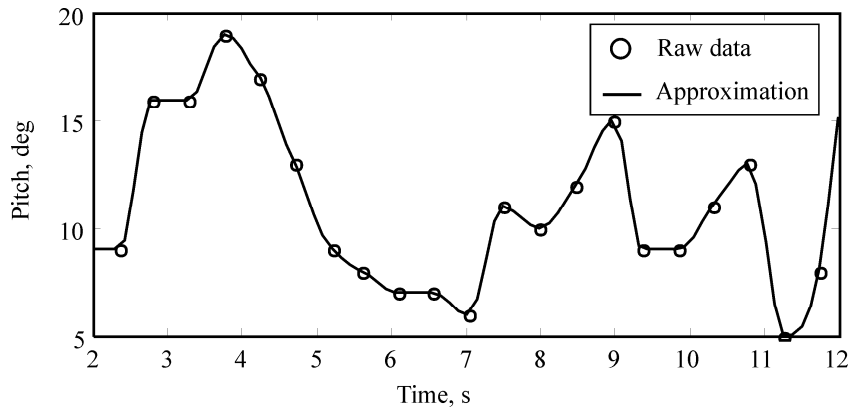


Fig. 8. Time history of the pitch angle.

A dynamic behavior of the ornithopter similar to the short-period oscillatory motion was observed with a time period of about 1 sec and time required for the oscillations in angle of attack and pitch to decay to one-half of initial amplitude of about 2 sec (2 – 5 sec time period in Figs. 7 and 8). After the oscillations decayed, response in angle of attack and pitch was non-oscillatory for about 2 sec, and after that oscillation started again with approximately same period. Even though this dynamic effect was established qualitatively and oscillation parameters can not be accurately estimated based on the available data, this dynamic mode can be regarded as similar to short period oscillations. Long period oscillations, which could be treated as a phugoid mode, were not observed during the test flights.

Spectral analysis is applied to the recorded pitch history. The data corresponding to the variation of pitch angle, θ , (Fig. 8), with respect to time are considered in the spectrum analysis. The recorded data are analyzed using the fast Fourier transform algorithm in Matlab.[®] The frequencies of the pitch angle in Fig. 9 show how much of the signal lies with each frequency band over a range of frequencies. The data depict the fundamental frequency of the pitching angle in the major peak at 0.23 Hz. Another peak can be seen in the range of 1-1.25 Hz that corresponds to the noticed short period oscillations.

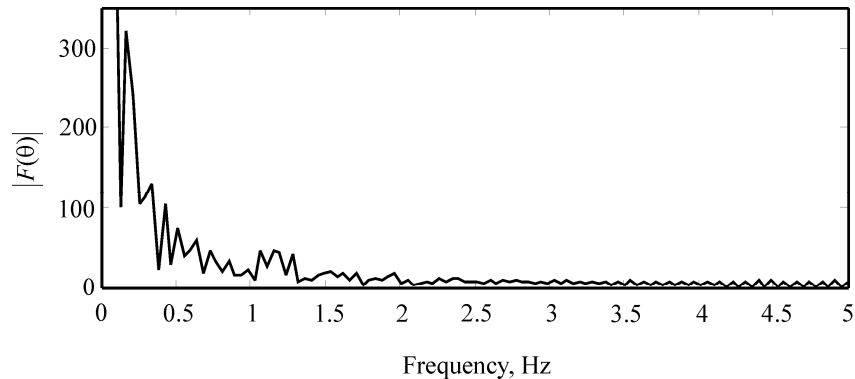


Fig. 9. Frequency corresponding to the pitch angle data.

V. Conclusions

A multi-body dynamic model of the ornithopter was developed in this study and a procedure for the estimation of the parameters of this model was proposed. The experimental ornithopter was built and the autopilot controller was integrated into the vehicle. Flight tests showed that the ornithopter is capable of a controlled sustained flight in the autonomous mode. In-flight real-time telemetry data were collected and an initial analysis was conducted on this set of data. Preliminary analysis shows that the ornithopter exhibits a dynamic behavior that is similar to short period oscillations.

Acknowledgments

This work has been sponsored by a grant from the AFRL, Eglin AFB (Program Manager Dr. Gregg Abate).

References

- ¹Willmott, A. P., Ellington, C. P., “The Mechanics of Flight in the Hawkmoth *Manduca Sexta*, II. Aerodynamic Consequences of Kinematic and Morphological Variation,” *The Journal of Experimental Biology*, 200, 1997, pp. 2723 – 2745.
- ²Pennycuik, C. J., Lock, A., “Elastic Energy Storage in Primary Feather Shafts,” *The Journal of Experimental Biology*, 64, 1976, pp. 677 – 689.
- ³Azuma, A., Okamoto, O., Yasuda, K., “Aerodynamic Characteristics of Wings at Low Reynolds Number,” *Fixed and Flapping Wing Aerodynamics for Micro Air Vehicle Applications*, edited by T. J. Mueller, Vol. 195, AIAA, Reston, Virginia 2001, pp. 341–398.
- ⁴Larijani, R. F., DeLaurier, J. D., “A Nonlinear Aeroelastic Model for the Study of the Flapping Flight,” *Fixed and Flapping Wing Aerodynamics for Micro Air Vehicle Applications*, edited by T. J. Mueller, Vol. 195, AIAA, Reston, Virginia 2001, pp. 399–428.
- ⁵Frampton, K. D., Goldfarb, M., Monopoli, D., Cveticanin, D., “Passive Aeroelastic Tailoring for Optimal Flapping Wings,” *Fixed and Flapping Wing Aerodynamics for Micro Air Vehicle Applications*, edited by T. J. Mueller, Vol. 195, AIAA, Reston, Virginia 2001, pp. 473–482.
- ⁶Roskam, J., *Airplane Flight Dynamics and Automatic Flight Controls. Part I*, Design, Analysis and Research Corporation, Lawrence, KS, 2003.
- ⁷Etkin, B. Reid, L. D., *Dynamics of Flight Stability and Control*, Third Edition, John Wiley and Sons, Inc., New York, NY, 1996.
- ⁸Nelder, J. A., Mead, R., “A Simplex Method for Function Minimization,” *Computer Journal*, 7, 1965, pp. 308 – 313.
- ⁹Drouin, A., Brisset, P., “PaparadzY: Do-It-Yourself UAV,” *4th European Micro-UAV Meeting*, Toulouse, France, Sept. 15-17, 2004.
- ¹⁰Krashanitsa, R., Platanitis, G., Silin, D., Shkarayev, S., “Autopilot Integration into Micro Air Vehicles,” *Introduction to the Design of Fixed-Wing Micro Aerial Vehicles*, edited by T. J. Mueller, J. C. Kellogg, P. G. Ifju, and S. V. Shkarayev, AIAA, Reston, VA, 2006.
- ¹¹Krashanitsa, R., Platanitis, G., Silin, B., Shkarayev, S., “Aerodynamics and Controls Design for Autonomous Micro Air Vehicles,” *AIAA Atmospheric Flight Mechanics Conference and Exhibit*, August 21-24, 2006, Keystone, Colorado, AIAA 2006-6639.
- ¹²Silin, D., Malladi, B., Shkarayev, S., “The University of Arizona Micro Ornithopters,” Proceedings from the 2nd US-European Workshop and Competition on Micro Air Vehicles, October 30 – November 2, 2006, Eglin AFB, Florida.

Appendix 5

Flight Dynamics of Flapping-Wing Air Vehicle

This page intentionally left blank

Flight Dynamics of Flapping-Wing Air Vehicle

Roman Y. Krashanitsa,¹ Dmitry Silin,² and Sergey V. Shkarayev³
University of Arizona, Tucson, Arizona, 85721, USA

Gregg Abate⁴
Air Force Research Laboratory, Munitions Directorate, Eglin AFB, FL 32542-6810, USA

The research and development efforts presented in this paper address the flight dynamics of a flapping-wing air vehicle (ornithopter). The 74-cm wing span ornithopter was equipped with the automatic control system that provides the stability augmentation and navigation of the vehicle, and flight data acquisition. Wind tunnel tests were conducted with the control surfaces fixed in neutral position and flapping motion of the wings activated by a motor at a constant throttle setting. Coefficients of a lift, drag, and pitching moment were determined at a free stream velocity of 7.2 m/sec and the angle of attack varied from 0 to 41 degrees. In addition, variations of derivatives of aerodynamic coefficients with the freestream velocity were investigated. A series of flight tests were conducted with fixed controls demonstrating ornithopter stability in all axes. Proportional control laws were programmed into the autopilot for the closed-loop controls. A number of test flights of the autonomous ornithopter were conducted with the telemetry acquisition. During the autonomous flights, the autopilot performed waypoint and altitude navigation demonstrating stable performance.

Keywords: flapping, flight, ornithopter, dynamics, wind tunnel, stability, experiments.

Nomenclature

α	= angle of attack
C_D	= drag coefficient [$C_D = D/(0.5\rho V^2 S)$]
C_L	= lift coefficient [$C_L = L/(0.5\rho V^2 S)$]
C_M	= pitching moment coefficient [$C_M = M/(0.5\rho V^2 S \bar{c})$]
$C_{D^*}, C_{L^*}, C_{M^*}$	= drag, lift, and pitching moment coefficient derivatives
\bar{c}	= wing mean geometric chord
D	= drag force
L	= lift force
M	= pitching moment
S	= wing planform area
V	= freestream velocity

I. Introduction

In recent years, a number of research studies have been conducted on the important aspects of flapping flight in nature and on flapping-wing micro air vehicles (ornithopters). These studies focused mostly on the kinematics of

¹ Research Assistant Professor, Dept. of Aerospace and Mechanical Engineering, 1130 N. Mountain Ave.

² Graduate Research Assistant, Dept. of Aerospace and Mechanical Engineering, 1130 N. Mountain Ave.

³ Associate Professor, Dept. of Aerospace and Mechanical Engineering, 1130 N. Mountain Ave., Member, AIAA

⁴ Team Leader, Airframe Dynamics & Robust Control, AFRL/RWGN, Associate Fellow AIAA

flapping wings, unsteady flow physics, and associated aerodynamic forces.

Some of the notable works in the field of flapping flight were completed by zoologists. Willmott and Ellington¹ studied the kinematics of the flight of a hawkmoth *Manduca Sexta* using two high-speed video cameras. Their study revealed the mechanics of the body motion and the range of wing flapping and feathering angles during a flight.

Frampton et al.² experimentally investigated effects of wing flapping and rotation on the generated thrust. Thrust-to-power ratios and efficiency parameters were determined. The obtained results indicate that a wing, flapping and rotating in phase, generates larger thrust, whereas a wing with rotational motion lagging the flapping motion by 90 degrees results in a better power efficiency.

Flapping-wing micro air vehicles generate lift and thrust for forward motion using their flapping wings, emulating birds and insects. However, just mimicking the flight of birds and insects is insufficient for designing flapping-wing vehicles. Here is how this viewpoint was elucidated by Mueller and DeLaurier:³ “The primary motivation for studying animal flight is to explain the physics for a creature that is known to fly... An ornithopter designer, in contrast, is trying to develop a flying aircraft, and its ability to achieve this is no given fact.” Furthermore, a successful ornithopter design provides a verifiable physical model of flight in nature.

Aerovironment pioneered the design of radio-controlled micro ornithopter called Microbat.⁴ The most successful vehicle of this type has a half-ellipse wing planform with a 20-cm wingspan flapping at 22 Hz. The project proved to be challenging because of the limited knowledge on unsteady aerodynamics of flexible flapping wings of the size this small and lack of enabling micro technologies.

DeLaurier and his group developed a 35-cm radio-controlled ornithopter capable of hovering.⁵ The kinematics of the 4 wings (X-wing) mimics the “cling-flip” mechanism employed by some insects and birds. Hovering flights in excess of one minute were achieved with a flapping frequency of 28 Hz. It was noted that transition to forward flight remains a problem, but that it may be overcome by an intelligent flight stabilization system.

Ellington⁶ summarized the flight kinematics and dynamics of insects, which could be useful for prospective insect-size MAV designs. The motion of the flapping wing is described with respect to a flapping plane, also called a stroke plane. Insects have been observed to perform quick maneuvers by tilting the stroke plane of their wings, just like a helicopter. Lateral direction changes can be accomplished by a roll of the stroke plane (often by increasing flapping amplitude and/or angle of attack of the outside wing). Angle of attack changes also initiate low-speed acceleration. For slower flight and hovering, the body hangs below the wing bases, and the insect benefits from a passive pendulum-like stability.

An ornithopter competition has been added to the 8th International MAV Competition in Tucson, Arizona in 2004. This competition involved building the smallest radio-controlled ornithopter that can fly the most laps around a pylon course in 2 min. The pylons were spaced 40 feet apart and the ornithopters flew either an elliptical course around them or a figure-8 through them. The University of Arizona (UA) won the 2004,⁷ 2005,⁸ and 2006⁹ competitions with 28-cm, 20-cm, and 15-cm ornithopters, respectively.

The primary objective of the present study is to investigate flight dynamics and automatic controls for flapping flight by using an ornithopter as a physical model. Specifically, better understanding of dynamics of flapping flight will be achieved by combining wind tunnel testing and in-flight telemetry data.

II. Ornithopter Design and Specifications

The 74-cm ornithopter (Figs. 1 and 2) was built and equipped with the automatic control system providing stabilization and navigation of the vehicle, and in-flight data acquisition and transmission to the ground station. The off-the-shelf Cybird ornithopter was selected for the autopilot integration. This ornithopter underwent a thorough flight testing. Utilizing this flight experience the ornithopter has been modified in order to improve its payload capability. The original airframe had a tail consisting of a single surface, with adjustable elevation and controllable rotation, thus allowing directional control. This tail was replaced with a V-tail of twice as large area with the opening angle of 105°, and a 2.5 times longer tail boom. With these modifications more effective pitch and roll controls were achieved. After the necessary adjustments of the center of gravity position, the ornithopter was able to fly at a maximum speed of 10 m/s, withstanding a wind up to 3 m/s, and perform a series of sharp turns while maintaining an altitude. Its flight endurance at a moderate throttle setting was in excess of 7 min with a payload of 50 grams. The ornithopter geometry, components, and mass data are listed in Tables 1 and 2. Moment of inertia presented in Table 1 is defined with respect to the center of gravity.



Fig. 1 Autonomous ornithopter on the ground (left) and in flight (right).

Table 1. Ornithopter Specifications.

Parameter	Value
Wingspan (cm)	74
Length (cm)	53
Height (cm)	14
Wing area (cm ²)	991
Tail area (cm ²)	231
Tilt angle of the tail (deg)	-16
CG location from wing pivot (cm)	7.3
CG location from root chord (cm)	4.1
I_{yy} , (kg m ²)	1.4×10^{-3}

Table 2. Ornithopter Components.

Component	Description	Mass (g)
Wing	Carbon rods, nylon cloth	15
Tail	Carbon rods, nylon cloth	11
Fuselage with gearbox and nose	Fiberglass, EPP foam	78
Motor	Speed 370	28
RC receiver	PENTA 5	3
Speed controller	Electryfly 20A	4
2 Micro servos	Blue Arrow 3.6g	7
3-cell Lithium-Polymer Battery	Thunder Power 730 mAh	46
Autopilot	Paparazzi Tiny	22
Attitude sensor	IR sensor board	7
Radio modem	XB Pro 2.4 GHz	3
Misc	Wires, foam pads, etc	16
Total		248

In the present study, the ornithopter was equipped with the Paparazzi autopilot¹⁰ utilizing previous experience with this autopilot integration,^{11,12} into micro air vehicles. The autopilot includes a Phillips ARM7 microprocessor, a built-in U-Blox GPS processor with an 18-mm patch antenna mounted on the controller PCB, and an infrared sensor board to determine the attitude of the vehicle. The autopilot board was installed on the top of the airframe right underneath the wing (Fig. 2). In order to protect the board from vibrations, it was mounted using a block of foam. All the radio control components were located right under the board in the frame cutouts, thus the weight of the wiring was also minimized. An on-board antenna and a pair of X-Bee Pro modems by Maxstream, Inc. provided a wireless communication between the vehicle and the ground station. The flight control software consisted of the autopilot software on-board the aircraft and the ground station software. In flight, the autopilot sent telemetry data back to the ground station. Currently, the telemetry data include: GPS-based location data; speed, altitude, and climb rate of the airplane; pitch and roll angles of the aircraft provided by infrared sensors; autopilot status data; and position of the control surfaces. These data play a major role in performance analyses during the flight tests and adjustments of the control gains.

Longitudinal control of the ornithopter was accomplished by the proportional control for the altitude hold, with an inner pitch attitude loop. Similarly, the lateral-directional control was accomplished by an outer heading hold loop and an inner bank angle control loop, both using proportional control.

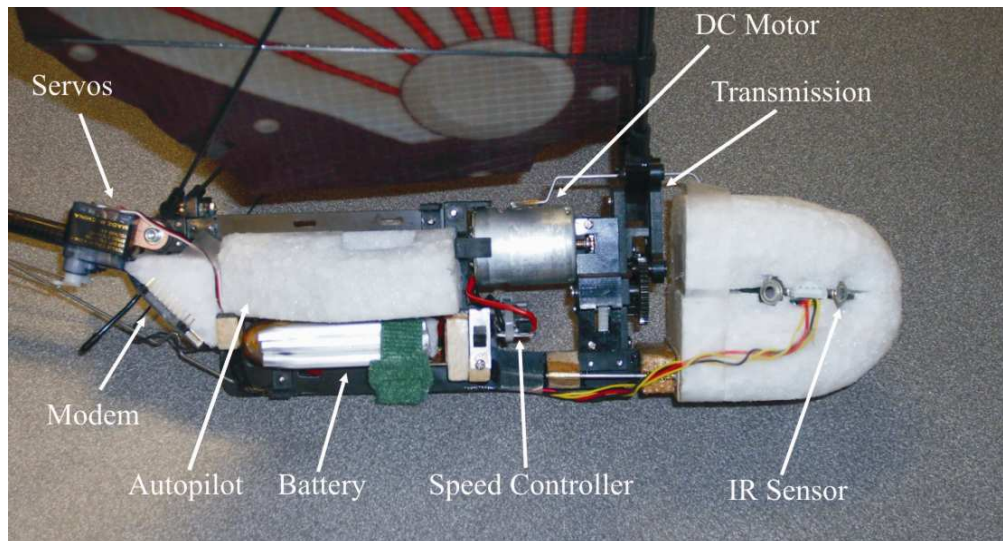


Fig. 2. Components of the ornithopter.

III. Wind Tunnel Measurements

Wind tunnel testing of the 74-cm ornithopter was performed in the Low Speed Wind Tunnel at the Aerospace and Mechanical Engineering Department of the University of Arizona (Fig. 3). This open contour wind tunnel has a 3×4 feet test section and a freestream velocity range from 2 to 50 m/s. The flow is laminarized in a settling chamber to less than 0.3% turbulence in the axial direction. The wind tunnel is equipped with a six-component balance. Force measurements are done using precision strain gages. Data from these strain gages are logged using the three National Instruments SCXI-1321 terminal blocks in low-noise SCXI-1000 chassis capable of sampling at 330,000 Hz.

Preliminary flights of the ornithopter were conducted including horizontal dashes at a constant speed. From the telemetry data acquired during these flights, the ornithopter was cruising at 7.2 m/s at the throttle setting at 67%.

The ornithopter was tested in the wind tunnel in a fully assembled configuration. Thus, measured aerodynamic forces, coefficients, and their derivatives include contributions of all components of the ornithopter: flapping wings, V-tail and fuselage. The elevons were mechanically fixed in a neutral position.



Fig. 3 The ornithopter in the wind tunnel.

A. Lift, Drag, and Pitching Moment Coefficients

The aerodynamic coefficients C_L , C_D , and C_M were determined at a freestream velocity of $V = 7.2$ m/s. The angle of attack was varied from 0 to 41 degrees. The throttle setting for flapping wings was chosen at 45%, 55%, 65%, and 75%. These settings correspond to a static flapping frequency of 6, 8, 10, and 12 Hz, respectively. They were measured using the digital tachometer HCAP0401.

Drag, D , lift, L , and pitching moment, M , were measured in the wind tunnel-based coordinate system. In this coordinate system the positive horizontal axis is directed downstream. The positive vertical axis is directed upward. The drag is defined as a positive force if the drag is greater than the thrust of a flapping wing. The pitching moment was determined about the center of gravity of the ornithopter.

As can be seen in Fig. 4, the lift coefficient increases with the throttle increase. At the throttle setting of 65%, the condition for the balanced level flight, in which the lift force equals to the weight, is satisfied at $\alpha = 20^\circ$ and $C_L = 0.86$. Quadratic interpolation was used for the determination of the lift coefficient derivative with respect to the angle of attack, C_{L_α} . For the throttle setting of 65% and $\alpha = 20^\circ$, it was found that $C_{L_\alpha} = 2.19 \text{ rad}^{-1}$. Note that no abrupt stall is observed in Fig. 4 for all throttle settings tested.

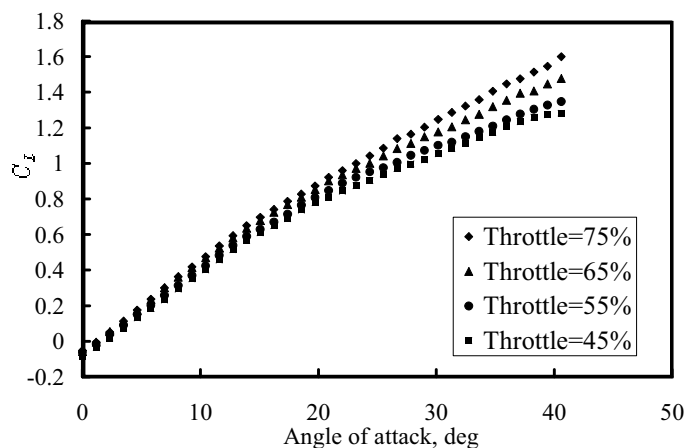


Fig. 4 Lift coefficient variation with angle of attack.

The drag coefficient curves presented in Fig. 5 are convex. In these results, a negative drag should be interpreted as a forward thrust. At moderate angle of attack, an increase of throttle setting provides a higher thrust generated by the flapping wings. As the angle of attack increases, the drag curves converge for all tested throttle settings. At a throttle setting of 65%, the thrust generated by flapping wings is in balance with the overall drag of the ornithopter at $\alpha = 20^\circ$ and, hence, $C_D = 0$. The drag curve slope at this point is $C_{D_\alpha} = 0.85 \text{ rad}^{-1}$.

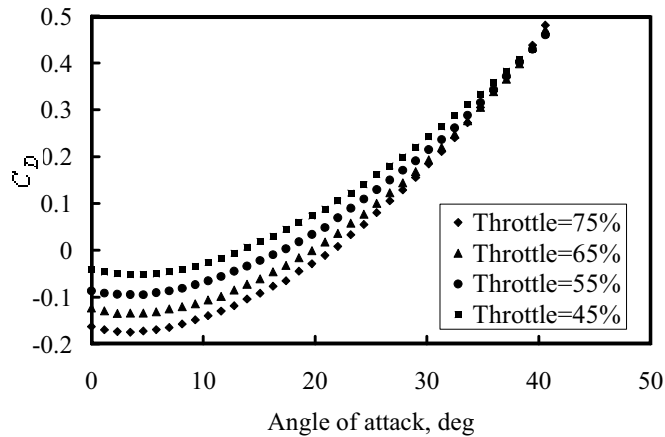


Fig. 5 Drag coefficient variation with angle of attack.

In the present tests, the zero pitching moment was not reached for the specified range of angle of attack. However, it can be predicted by extrapolation to the range of angle of attack from 44° to 48°.

The pitching moment coefficients presented in Fig. 6 are positive at $\alpha = 0^\circ$ and have negative slopes for all throttle settings tested. Positive value of the pitching moment at $\alpha = 0^\circ$ and negative pitching moment slope in a vicinity of the balanced angle of attack are two necessary conditions for longitudinal static stability under control-fixed conditions. This is a classical criterion of static stability developed for the conventional aircraft and based on this criterion the ornithopter is statically stable.

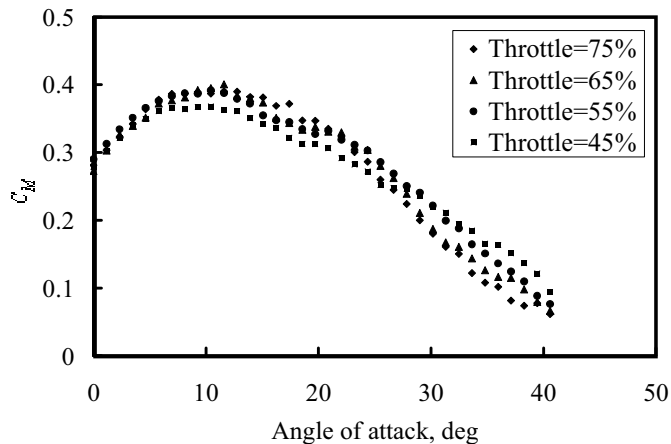


Fig. 6 Pitching moment coefficient variation with angle of attack.

B. The V Derivatives (C_{D_V} , C_{L_V} , C_{M_V})

The V derivatives reflect variation of aerodynamic coefficients with the freestream velocity and are important in the analysis of dynamic stability of an aircraft. In order to determine these derivatives, the ornithopter was tested in the wind tunnel at the constant angle of attack of $\alpha = 20^\circ$. The freestream velocity was varied from 7 to 7.5 m/s. Plots of aerodynamic coefficients can be seen in Fig 7. Here, dotted lines represent linear regressions. Derivatives were determined by using linear regression equations. For $\alpha = 20^\circ$ and at the throttle setting of 65%, the V derivatives of lift, drag, and pitching moment coefficients are $C_{L_V} = 0.114$, $C_{D_V} = -0.0151$, and $C_{M_V} = 0.04$, respectively.

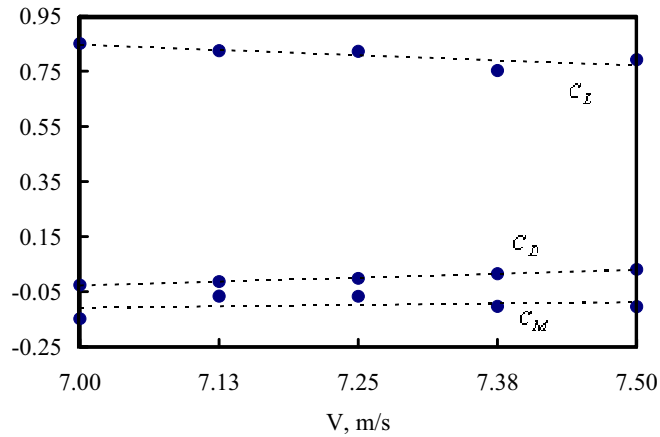


Fig. 7 Variation of aerodynamic coefficients with freestream velocity.

IV. Flight Test Results and Discussions

A. Flight with Fixed Controls

Flight experiments were conducted keeping the distance from the ground station to the ornithopter 10-20 m in order to maximize downlink bandwidth. In the course of flight experiments, telemetry data on the roll and pitch angles of the aircraft, its in-plane location (longitude and latitude), and altitude were acquired by the autopilot and transmitted to the ground station computer. The speed of the data transmission between computer and modem was set at 38,400 bps. The length of the transmitted data sample was 96 bit. Due to the specifics of the radio transmission protocol and distance effects on the quality of the signal, some samples were missing, resulting in the average sampling rate of 20 Hz.

The elevon angles to trim were determined from flights, in which the pilot flew the ornithopter via a radio transmitter. Then, the ornithopter flew 10 to 15 s dashes at a constant throttle setting at 67% and elevons fixed in the trimmed position.

The flight altitude variation and in-plane trajectory for the Flight 1 are shown in Figs. 8 and 9, respectively. The length of the dash was about 100 m. During the flight, both the altitude and flight direction have changed in oscillatory manner with a period of about 10 sec.

In-flight pitch and roll angle data were acquired and analyzed using the fast Fourier transform function from MATLABTM. Pitch and roll spectra are presented in Figs. 10 and 11, respectively. They are very similar in appearance with a dominant frequency of about 1.5 Hz.

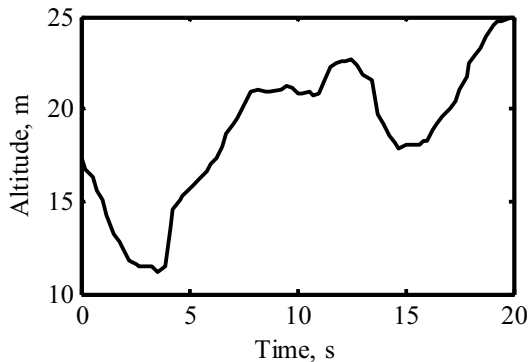


Fig. 8 Altitude history in Flight 1.

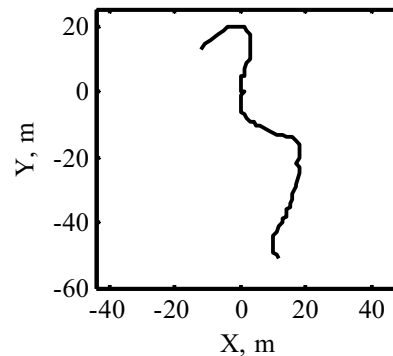


Fig. 9 Flight trajectory.

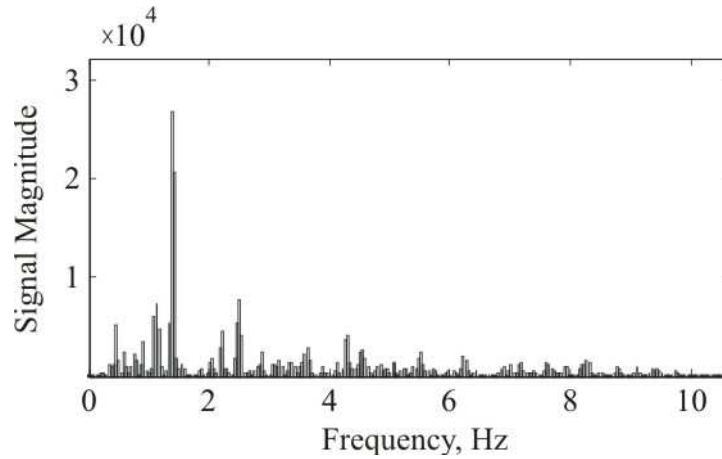


Fig. 10 Spectrum of pitch in Flight 1.

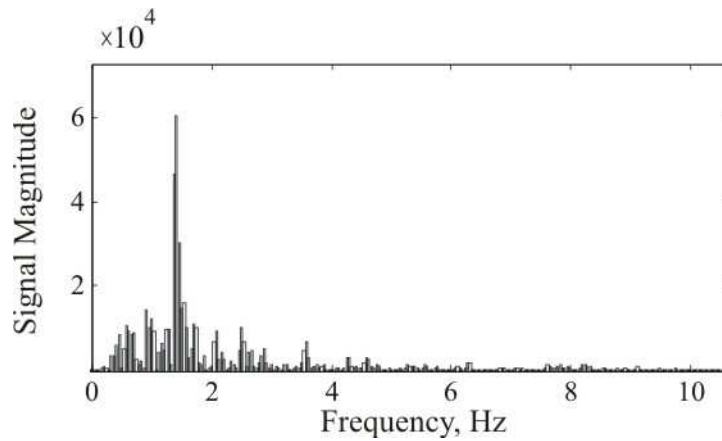


Fig. 11 Spectrum of roll in Flight 1.

The flight altitude variation and in-plane trajectory for the Flight 2 are shown in Figs. 12 and 13, respectively. This flight was shorter in time than the first one. The altitude was oscillating around the average value of about 22.5 m with a period of oscillations of 5 s. The flight trajectory seen in Fig. 13 is a semi-circular one with a radius of 15 m. For this flight, the elevators were fixed at the trimmed position, while ailerons were fixed slightly off the trimmed position. This explains a semi-circular flight path.

Pitch and roll angle data from the flight were also analyzed using fast Fourier transform. Pitch and roll spectra shown in Figs. 14 and 15, respectively, feature a dominant frequency at about 1.5 Hz, same as in the Flight 1.

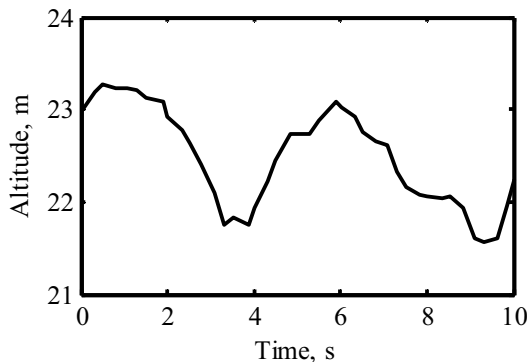


Fig. 12 Altitude history in Flight 2.

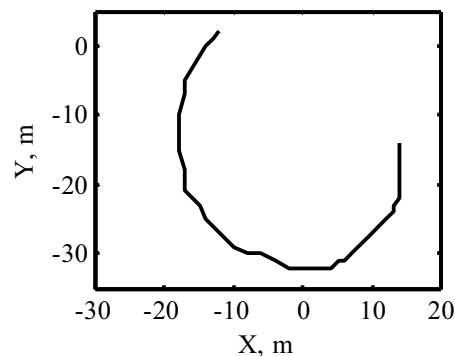


Fig. 13 Flight trajectory.

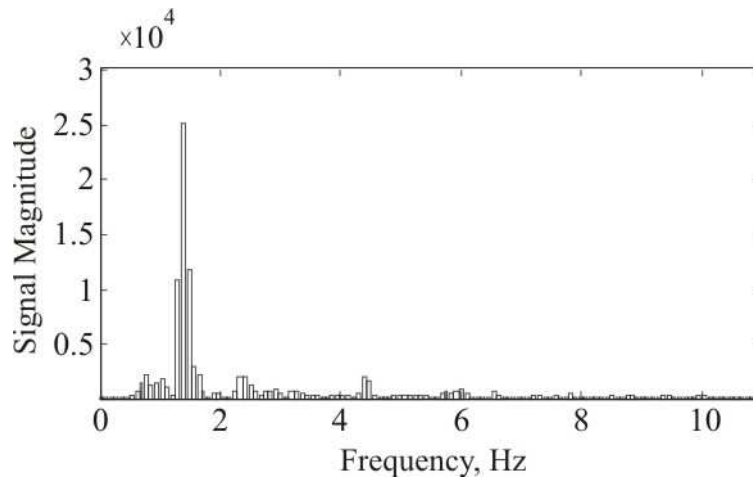


Fig. 14 Spectrum of pitch in Flight 2.

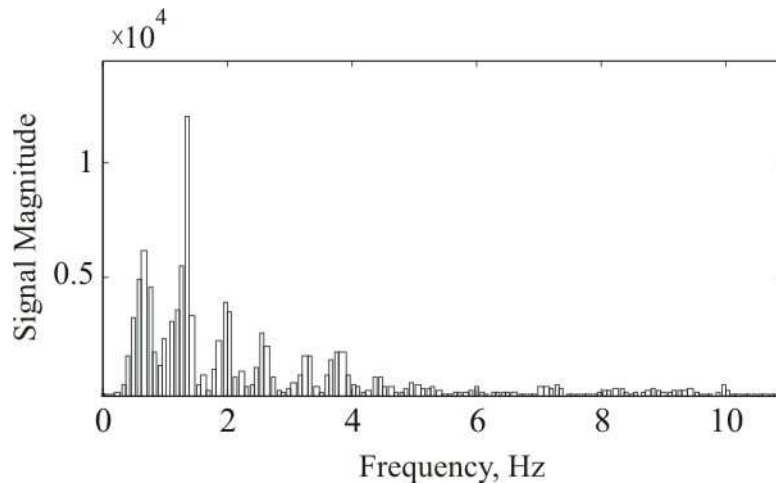


Fig. 15 Spectrum of roll in Flight 2.

The ornithopter flights performed with the controls fixed in a predefined position demonstrate similar type of oscillatory dynamics in both roll and pitch motions. There is a dominant harmonic at 1.5 Hz showed in both rotational motions and one possible cause for these oscillations is in the dynamics of the flapping-wing apparatus itself.

B. Autonomous Flights

Six autonomous flights were completed. The data acquired from one of the flight of the total duration of 350 sec are shown in Figs. 16–24. The flight plan was to navigate the aircraft between two waypoints. The only constraint put on the navigation was to fly within 5 m from a waypoint. The autonomous flight trajectory is shown in Fig. 16, where waypoints are labeled as “waypoint 1” and “waypoint 2”.

The ground speed was measured using an on-board GPS unit and presented in Fig. 17. Since the wind was present during the flight, the ground speed was changing for the flight segments in the wind and against the wind, and was varying within the range of 5-10 m/s.

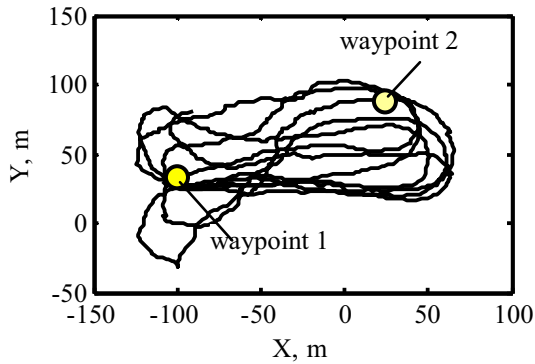


Fig. 16 Autonomous flight trajectory.

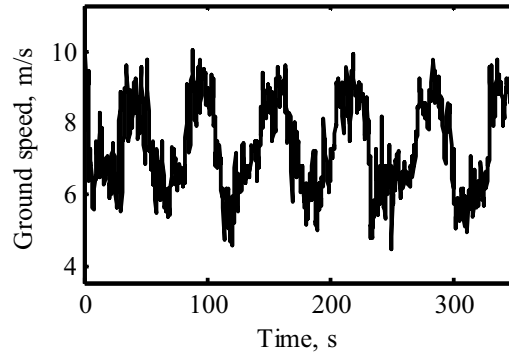


Fig. 17 Ground speed variation.

The throttle was controlled by the autopilot for the whole duration of the flight. As can be seen in Fig. 18, the throttle was varying in the range of 40%-80% for the major portion of the flight.

The plot of the on-board 3-cell battery voltage versus time is shown in Fig. 19. The flight started at the voltage value of 11.2V and at the end of the flight battery voltage was at 10 V.

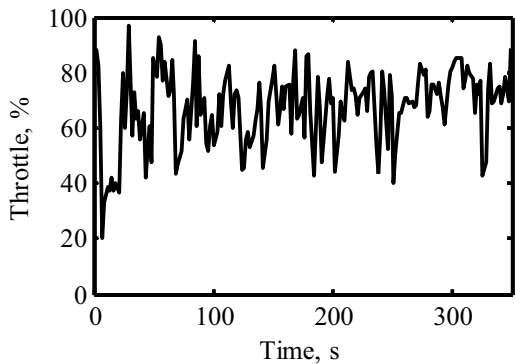


Fig. 18 Throttle time history.

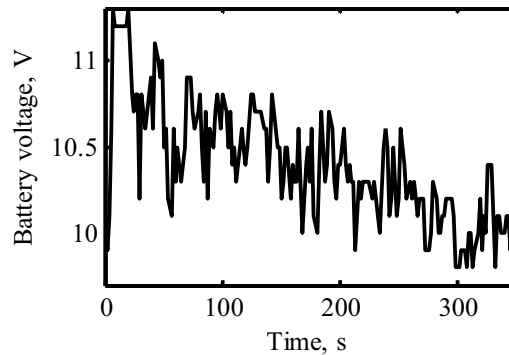


Fig. 19 Battery voltage change during flight.

Throttle setting and elevator were controlled by the inner loop of the altitude control algorithm. Results of the altitude control are shown in Fig. 20 as the actual altitude versus commanded altitude. Maximum altitude error for the duration of the flight was about 7 m and the average error was about 1 m. After 280 second of the flight time, the altitude was increased to 70 m (Fig. 20) by the command from the ground station. The ornithopter reacted by gaining 10 m in about 40 s.

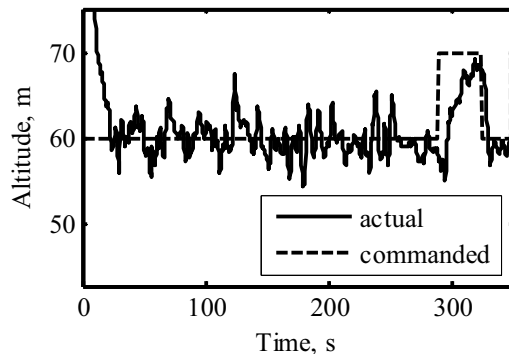


Fig. 20 Actual and commanded altitude variations.

Time histories of actual versus commanded roll and pitch angles are shown in Figs. 21 and 22, respectively. Elevator and aileron command histories are shown in Figs. 23 and 24, respectively.

Raw data for the actual values of roll and pitch were taken at about 4 Hz sampling frequency. Maximum error for the roll is about 15° , and for the pitch is about 15° as well.

There is a systematic error of -8° in a pitch time history (Fig. 23), which is probably due to initial trimming of the elevator. However, the altitude error was minimal (within 1-2 m on average). The average values of aileron and elevator deflections were less than 10% of the total range for servo for the whole duration of the flight.

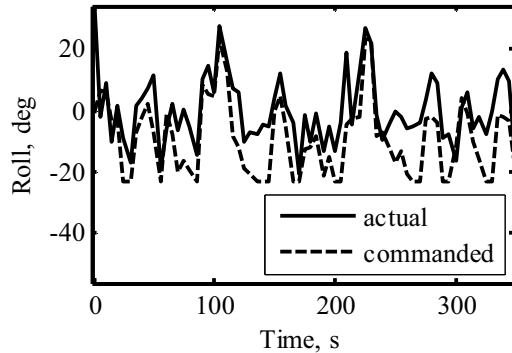


Fig. 21 Measured and commanded roll.

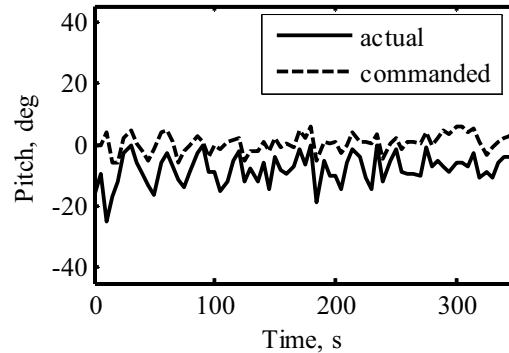


Fig. 22 Measured and commanded pitch.

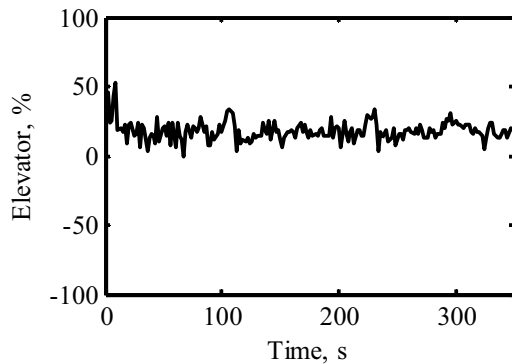


Fig. 23 Elevator command history.

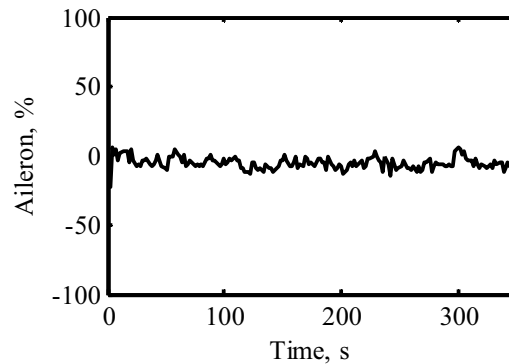


Fig. 24 Aileron command history.

V. Summary

In the present study, the experimental ornithopter was built and the autopilot was integrated into the vehicle. The autonomous ornithopter is a unique test bench for the investigations of aerodynamic forces, dynamics, and automatic controls in flapping flight.

Wind tunnel tests were conducted on the ornithopter. Values of lift, drag, and pitching moment were measured. Aerodynamic coefficients and their derivatives were determined in order to analyze performance and stability of the ornithopter. The longitudinal static stability under control fixed conditions was analyzed with the help of classical theory developed for the conventional aircraft. Based on this analysis, the ornithopter is statically stable.

Several control fixed and autonomous flights were performed in order to examine variation in a dynamic behavior of the flapping-wing apparatus. Telemetry data were acquired including altitude, in-plane trajectory, pitch and roll angles. Data were analyzed using fast Fourier transform techniques. The flights performed with the controls fixed demonstrate similar type of oscillatory dynamics in both roll and pitch motions. There is a dominant harmonic at 1.5 Hz and one possible cause for these oscillations is in the dynamics of the flapping-wing apparatus itself.

Flight experiments demonstrated that the ornithopter is capable of a controlled sustained flight in the autonomous mode.

VI. Acknowledgments

This work has been sponsored under a research grant from the Air Force Research Laboratory, Munitions Directorate, Eglin AFB, FL. The authors also would like to thank David Addai and Gavin Kumar for their contributions to the flight experiments.

References

- ¹Willmott, A. P., and Ellington, C. P., “The Mechanics of Flight in the Hawkmoth *Manduca Sexta*, II. Aerodynamic Consequences of Kinematic and Morphological Variation,” *The Journal of Experimental Biology*, 200, 1997, pp. 2723 – 2745.
- ²Frampton, K. D., Goldfarb, M., Monopoli, D., and Cveticanin, D., “Passive Aeroelastic Tailoring for Optimal Flapping Wings,” *Fixed and Flapping Wing Aerodynamics for Micro Air Vehicle Applications*, edited by T. J. Mueller, Vol. 195, AIAA, Reston, Virginia 2001, pp. 473–482.
- ³Mueller, T. J., and DeLaurier, J. D., An Overview of Micro Air Vehicle Aerodynamics, In: *Fixed and Flapping Wing Aerodynamics for Micro Air Vehicle Applications*, edited by T. J. Mueller, Vol. 195, AIAA, Reston, VA, 2001, pp. 1-12.
- ⁴Keennon, M., and Grasmeyer, J., Development of Two MAVs and a Brief Vision for the Future of MAVs Design, AIAA-2003-2901, AIAA International Air and Space Symposium and Exposition: The Next 100 Years, Dayton, Ohio, July 14-17, 2003.
- ⁵DeLaurier, J., “Ornithopter Research,” 2003 Bioflight Workshop, NASA Langley Research Center, August 7-8, 2003.
- ⁶Ellington, C. P., “The Novel Aerodynamics of Insect Flight: Applications to Micro Air Vehicles,” *The Journal of Experimental Biology*, Vol. 202, 1999, pp. 3439-3448.
- ⁷Thompson, P., Ward, G., Kelman, B., and Null, W., “Design Report: Development of Surveillance, Endurance, and Ornithoptic Micro Air Vehicles,” 2004 International Micro Air Vehicle Competition, Tucson, Arizona, 10 p., April 2004.
- ⁸Olson, D. H., Silin, D., Aki, M., Murrieta, C., Tyler, J., Kochevar, A., Jehle, A., and Shkarayev, S., “Wind Tunnel Testing and Design of Fixed and Flapping Wing Micro Air Vehicles at the University of Arizona,” *Micro Air Vehicle Design Papers*, Konkuk University, South Korea, 9 p., 2005.
- ⁹Yanagita, T., Lind, T., Malladi, B., Silin, D., Coopamah, D., Berka, T., Han, B., Rodriguez, S., and Shkarayev, S., “Simulation Wind Tunnel Testing, and Design of Fixed and Flapping Wing Micro Air Vehicles,” *Micro Air Vehicle Design Papers*, 10th International Micro Air Vehicle Competition, May 2006, Provo, Utah.
- ¹⁰Drouin, A., and Brisset, P., “PaparaDzIY: Do-It-Yourself UAV,” *4th European Micro-UAV Meeting*, Toulouse, France, Sept. 15-17, 2004.
- ¹¹Krashanitsa, R., Platanitis, G., Silin, D., and Shkarayev, S., “Autopilot Integration into Micro Air Vehicles,” *Introduction to the Design of Fixed-Wing Micro Aerial Vehicles*, edited by T. J. Mueller, J. C. Kellogg, P. G. Ifju, and S. V. Shkarayev, AIAA, Reston, VA, 2006.
- ¹²Krashanitsa, R., Platanitis, G., Silin, B., and Shkarayev, S., “Aerodynamics and Controls Design for Autonomous Micro Air Vehicles,” *AIAA Atmospheric Flight Mechanics Conference and Exhibit*, August 21-24, 2006, Keystone, Colorado, AIAA 2006-6639.

Appendix 6

Autonomous Micro Air Vehicles with Hovering Capabilities

This page intentionally left blank

Autonomous Micro Air Vehicles with Hovering Capabilities

Review of the AFRL Grant FA86510710002
to the University of Arizona
PI: Sergey Shkarayev

Program Manager: Gregg Abate, AFRL

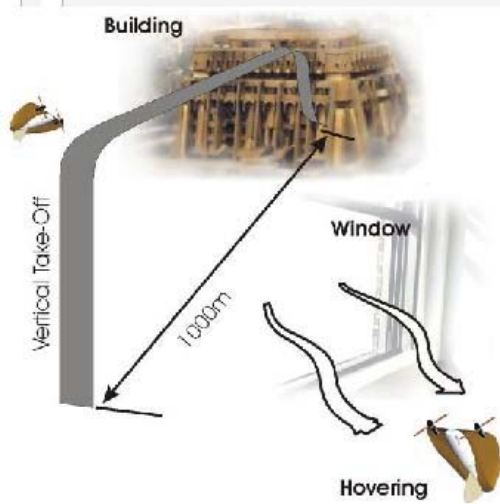
July 15, 2008

Personnel and project management

The part of this project represents collaborative efforts of the University of Arizona and ISAE, Toulouse, France towards the development of VTOL MAV technologies. It was sponsored by grants from the AFRL to UA, and by EOARD to the ISAE

- UA Faculty
Sergey Shkarayev, PI
Roman Krashanitsa, Research Professor
- UA Students
Bill Silin
David Addai
Bharani Malladi
- ISAE collaborators
Jean-Marc Moschetta
Boris Bataille

Research motivation and objectives



- Urban operation scenario
- Rapid ingress/egress
- Vertical take-off and landing
- Hovering
- High maneuverability in tight space, flying into windows and inside of buildings

Research Objectives:

- (1) to develop concepts of MAVs with hovering capabilities, while maintaining fast horizontal flight
- (2) to conduct research studies on aerodynamics and flight dynamics of fixed-wing and flapping-wing MAVs

Stated Plan

Task 1. Conceptual design of fixed-wing VTOL MAVs [Completed Sept 2007]

- 1.1 Flight performance analysis for three VTOL MAV concepts
- 1.2 Development of novel propulsion and design method for VTOL

Task 2. Aerodynamics of fixed and flapping wings [Completed March 2008]

- 2.1 Studies on VTOL MAV propulsion
- 2.2 Wind tunnel measurements on wing under free stream and slip stream
- 2.3 Development of model for zero-lift drag of thin cambered wing
- 2.4 Wind tunnel studies on an ornithopter

Task 3. Flight testing of VTOL MAVs [Completed May 2008]

- 3.1 Test flights with stability augmentation
- 3.2 Studies on automatic controls for VTOL MAV in hover
- 3.3 Technology demonstration and assessment

Task 4. Flight dynamics and controls of flapping-wing MAVs [Completed Sept 2007]

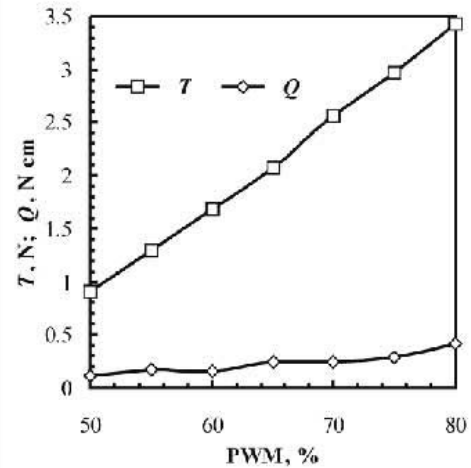
- 4.1 Dynamic model for an ornithopter
- 4.2 Integration of autopilot into ornithopter
- 4.3 Flight dynamics of an ornithopter

Task 1. Conceptual design of fixed-wing VTOL MAVs

Contra-rotating props tilt-body



Speed 0-15 m/s



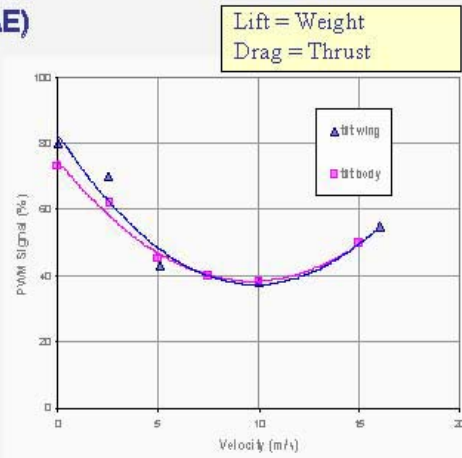
Torque for contra-rotating system is 10 times lower in comparison with a single propeller

VTOL MAV Concepts (Cont.)

Side-by-side props tilt-wing vs tilt-body (ISAE)



Speed 0-15 m/s
Tilt angles 0°, 30°, 60°, 90°
PWM signal 40, 60, 80, 100%



Tilt-wing requires more power in transition

VTOL MAV Design Concepts (Cont.)

Aerodynamics and flight performance for three VTOL MAV design concepts were analyzed:

Tilt-rotor

Major drawback – downloading from rotors onto the wing



Tilt-wing

Major drawbacks – more power required, complex wing tilting mechanism



Tilt-body

Major advantages – simple design, low torque

Proof of concept VTOL MAV was tested in manual and auto flights



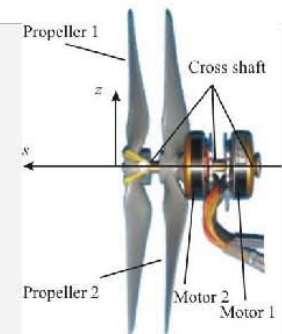
Wingspan (cm)	30
Length (cm)	20
Wing area (cm ²)	488
Weight (g)	185
Endurance (min)	~20
Speed (m/s)	0-15

This vehicle can be considered a milestone on the way to a fully functioning prototype

Novel propulsion and design method for VTOL

Developed propulsion system of coaxial contra-rotating motors-propellers

one prop/motor directly behind the other in the axial direction, spinning in opposite directions, no gear box needed

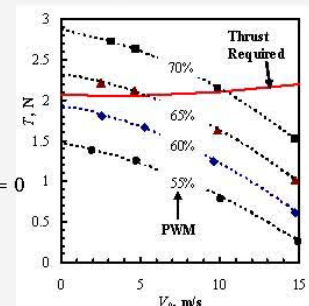


Design method is proposed for MAV in hover and vertical flight

The method is based on the analysis of the thrust available from the propulsion system and thrust required for the vertical flight

$$T - W - 0.5\rho \left[C_{D_0} V_0^2 (S_0 - S_p) + (-0.0009w^2(0) + 0.0147w(0) + 0.0237) \int_{S_p} V_p^2(s) dS_p \right] = 0$$

The method utilizes the developed zero-lift-drag model. Flight tests proved that the developed method and data are sufficient for designing VTOL MAVs

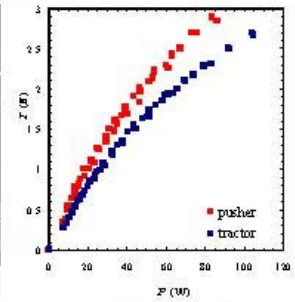
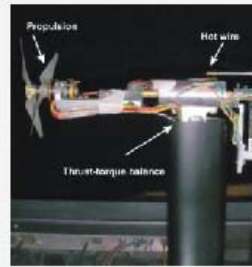


Task 2. Aerodynamics of fixed and flapping wings

Studies on VTOL MAV propulsion

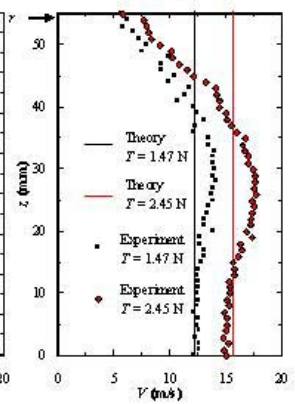
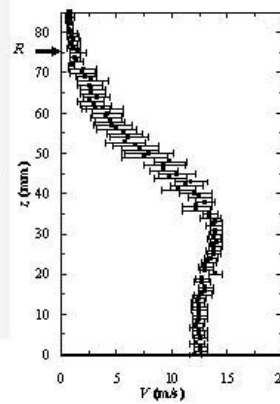
Propulsion evaluation on motor testing bench

single vs coaxial – no gains, no losses
 coaxial 10 times lesser torque
 pusher vs tractor – a significant form drag on tractor



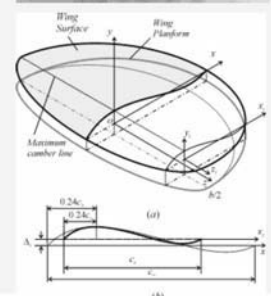
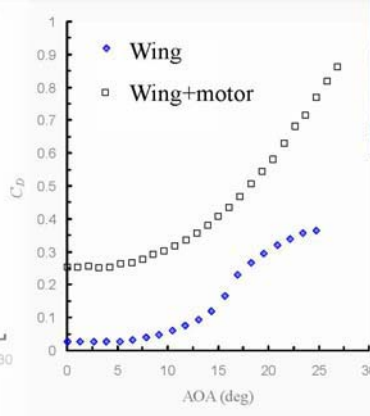
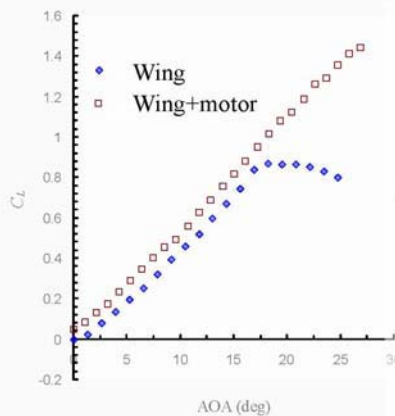
Hot wire measurements

Fluctuations in velocities in terms of a STD are indicative of non-stationary, pulsating flow behind the propellers
 Propeller momentum theory can accurately predict average air velocity
 The radius of the stream tube to be used for sizing wing, fuselage, control surfaces



Wind tunnel measurements on low Re wing under free stream and slip stream

PWM = 55%, Re = 100,000



It was found that the propulsive-induced flow had significant effects on aerodynamic coefficients:

C_{D0} , C_{Dmin} , $C_{L\alpha}$, C_{Lmax} , C_{L0}

Model for zero-lift drag for thin cambered wing

Propeller induced velocity at the distance s from the propeller disk

$$w(s) = 0.5 \left[\sqrt{V_0^2 + \frac{2T}{\rho\pi R^2} \left(1 + \frac{s/R}{\sqrt{1 + (s/R)^2}} \right)} - V_0 \right]$$

Total drag can be expressed as

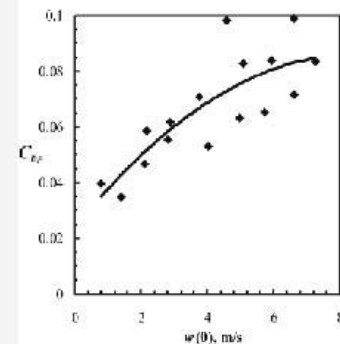
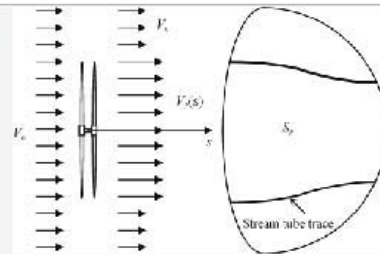
$$D_0 = D_{V_0} + D_{V_p}$$

$$D_{V_0} = 0.5 \rho C_{D_0} V_0^2 (S_0 - S_p)$$

$$D_{V_p} = 0.5 \rho C_{D_p} \int_{S_p} V_p^2(s) dS_p$$

Zero-lift drag coefficient in the stream tube

$$C_{D_p} = \frac{D_0 - 0.5 \rho C_{D_0} V_0^2 (S_0 - S_p)}{0.5 \rho \int_{S_p} V_p^2(s) dS_p}$$



Aerodynamic theory for a low Re number wing under free stream and slip stream in MAV fast transition is needed

Task 3. Flight dynamics and controls for VTOL MAV Test flights with stability augmentation

Avionics

3 double-axis MEMS gyroscopes IDG300

Series of stability augmented flights demonstrated:

- Rapid ingress/egress and transition
- Transition hover-to-horizontal and horizontal-to-hover
- Hovering



<http://youtube.com/watch?v=6iPJUaQA2OM&feature=related>

Autonomous hovering of VTOL MAV

Avionics for automatic hovering

Paparazzi autopilot
 2 double-axis MEMS gyroscopes IDG300
 Ultrasonic range sensor Maxbotix LV-EZ1

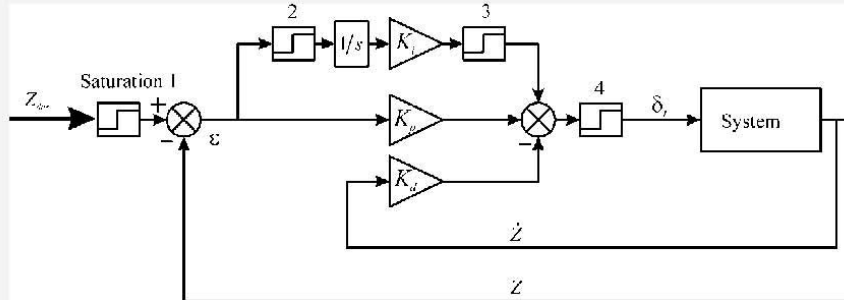
Control laws

PD

Dynamics of hovering

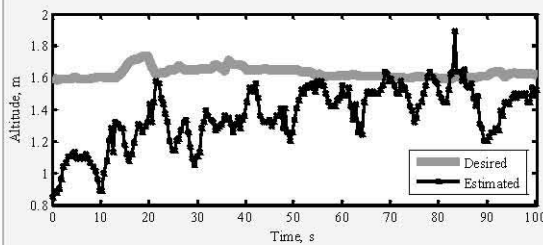
$$m\ddot{Z} = T - D - mg$$

$$D_{V_p} = 0.5\rho C_{D_p} \int_{S_p} V_p^2(s) dS_p$$

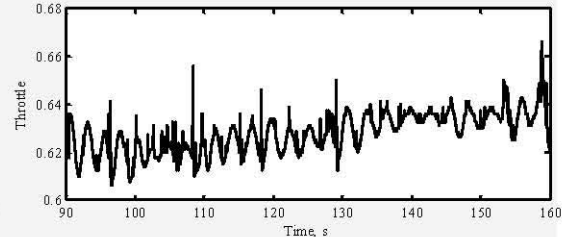
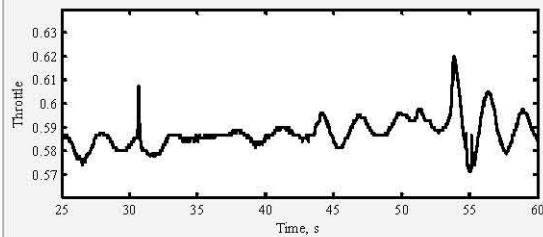
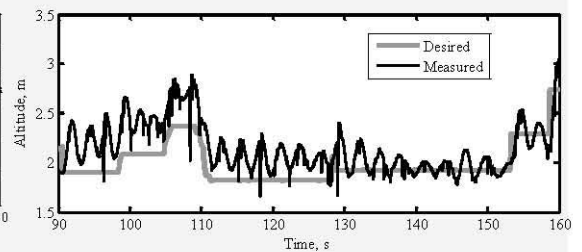


Autonomous hovering of VTOL MAVs (cont.)

Flight 1



Flight 2



Technology Demonstration and Assessment

- 1st US-Asian Demonstration and Assessment of Micro-Aerial and Unmanned Ground Vehicle Technology, Agra, India, 2008
- 12 teams from universities and companies from US, Europe, Asia, and Australia
- University of Arizona tied 1st place and won 3 major awards



Mini-Vertigo
VTOL MAV



Dragonfly
Autonomous MAV



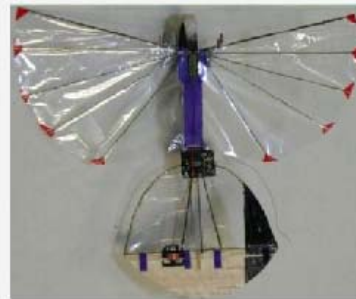
Sim UGV

Next steps: studying flight dynamics to design control laws for steady flight, pitch-up and -down transition; ground and wall effects, vertical landing, development of fully functioning VTOL MAV prototypes

World smallest flapping-wing MAV (UA)



Manduca sexta (giant moth)
Wing span, 12-15 cm
Speed 0-6 m/s
Flapping Frequency 25 Hz



UA *Ornithopter* (micro air vehicle)
Wing span, 15 cm
Speed 2-4 m/s
Flapping Frequency 25 Hz

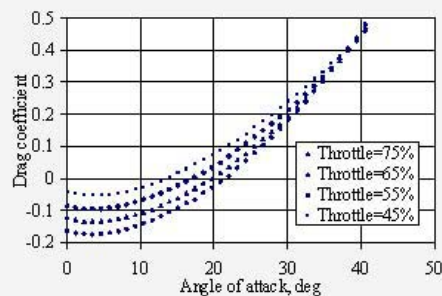
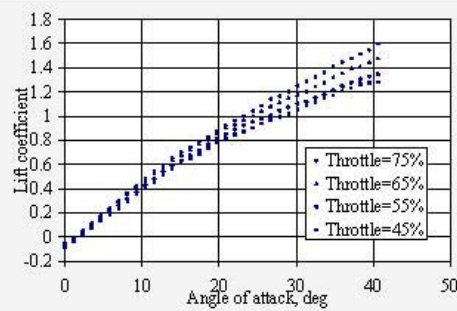
Autonomous ornithopter



Wingspan (cm)	74
Length (cm)	53
Height (cm)	14
Wing area (cm ²)	991
Tail area (cm ²)	183
Weight (g)	248

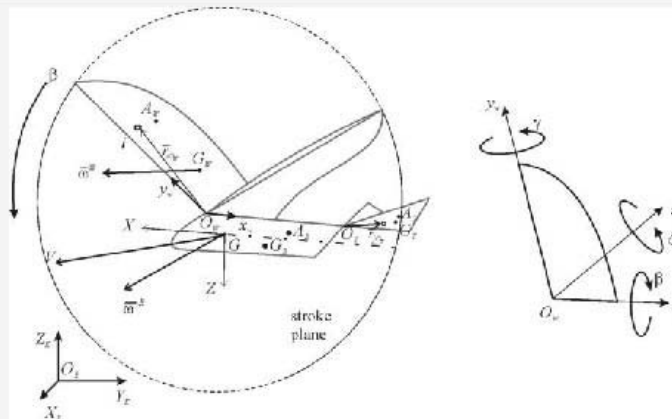
Channel	Function
Guidance	
Heading	via roll
Altitude	via flapping freq
Control	
Pitch	RPM, V-tail controls
Roll	V-tail controls

Task 2.4 Wind tunnel measurements on ornithopter



Lateral aerodynamics has to be studied

Task 4. Flight dynamics of flapping wing MAVs Dynamic model for ornithopter



Equations of motion

$$m_{TO} \ddot{\bar{r}}_G = \bar{F}_a^B + 2\bar{F}_a^T + 2\bar{F}_a^W + \bar{F}_g^{TO} - 2 \int_W \left(\ddot{\mathbf{R}}_1(\bar{r}_W)_{XYZ} + \frac{d^2}{dt^2} (\mathbf{R}_1 \mathbf{R}_W)(\bar{r}_{iW})_{xywz_w} \right) dm_w$$

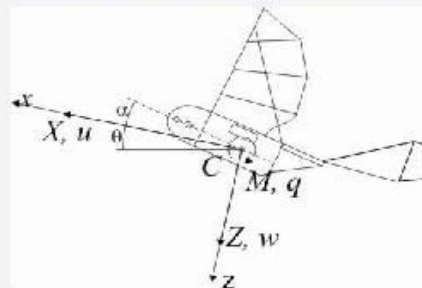
$$\bar{M}_G^W + \bar{M}_G^T + \bar{M}_G^B = m_w \bar{r}_{G_wG} \times \bar{a}_G + \dot{\bar{H}}_G^W + \bar{r}_{G_rG} \times \bar{a}_G + \dot{\bar{H}}_G^T + \dot{\bar{H}}_G^B$$

Linear time-invariant model

- Stroke-averaged forces and moments
- Use of small perturbations and linearization of equations of motion

$$\dot{\mathbf{x}} = \mathbf{A}\mathbf{x}$$

$$\mathbf{x} = [\Delta u \quad w \quad q \quad \Delta \theta]^T$$



$$\mathbf{A} = \begin{bmatrix} \frac{X_u}{m} & \frac{X_w}{m} & 0 & -g \cos \theta_0 \\ \frac{Z_u}{m - Z_{\dot{w}}} & \frac{Z_w}{m - Z_{\dot{w}}} & \frac{Z_q + m\lambda_0}{m - Z_{\dot{w}}} & \frac{-mg \sin \theta_0}{m - Z_{\dot{w}}} \\ \frac{1}{I_y} \left[M_u + \frac{M_{\dot{w}} Z_u}{m - Z_{\dot{w}}} \right] & \frac{1}{I_y} \left[M_w + \frac{M_{\dot{w}} Z_w}{m - Z_{\dot{w}}} \right] & \frac{1}{I_y} \left[M_q + \frac{M_{\dot{w}} (Z_q + m\lambda_0)}{m - Z_{\dot{w}}} \right] & -\frac{1}{I_y} \frac{M_{\dot{w}} mg \sin \theta_0}{m - Z_{\dot{w}}} \\ 0 & 0 & 1 & 0 \end{bmatrix}$$

Numerical results

Dimensional derivative	Non-dimensional derivative	Roots of the characteristic equation
$X_u = C_{x_u} \rho u_0 S / 2$	$* C_{x_u} = -0.114$	$\lambda_1 = -783.26$
$Z_u = C_{z_u} \rho u_0 S / 2$	$* C_{z_u} = -0.0151$	
$M_u = C_{m_u} \rho u_0 \bar{c} S / 2$	$* C_{m_u} = 0.04$	
$X_w = C_{x_w} \rho u_0 S / 2$	$* C_{x_w} = -0.85$	$\lambda_2 = -18.47$
$Z_w = C_{z_w} \rho u_0 S / 2$	$* C_{z_w} = -2.19$	
$M_w = C_{m_w} \rho u_0 \bar{c} S / 2$	$* C_{m_w} = -0.97$	$\lambda_{3,4} = -0.12 \pm 0.76i$
$X_q = C_{x_q} \rho u_0 \bar{c} S / 4$	$C_{x_q} \approx 0$	
$Z_q = C_{z_q} \rho u_0 \bar{c} S / 4$	$C_{z_q} = -2a_t V_H$	
$M_q = C_{m_q} \rho u_0 \bar{c}^2 S / 4$	$C_{m_q} = -2a_t V_H l_t / \bar{c}$	
$X_{\dot{w}} = C_{x_{\dot{w}}} \rho u_0 S / 4$	$\dagger C_{x_{\dot{w}}} = 0$	
$Z_{\dot{w}} = C_{z_{\dot{w}}} \rho u_0 S / 4$	$\dagger C_{z_{\dot{w}}} = 0$	
$M_{\dot{w}} = C_{m_{\dot{w}}} \rho u_0 \bar{c}^2 S / 4$	$\dagger C_{m_{\dot{w}}} = 0$	

* Measured in WT

Integration of autopilot into ornithopter

Test flights of an ornithopter:

- Control-fixed,
- Stability augmented mode
- Fully autonomous mode

Telemetry data included roll and pitch angles, in-plane location, and altitude

Sampling rate (~20Hz) for data series varied due to RF transmission protocol and distance effects

Data analysis utilizes low pass filtering and FFT

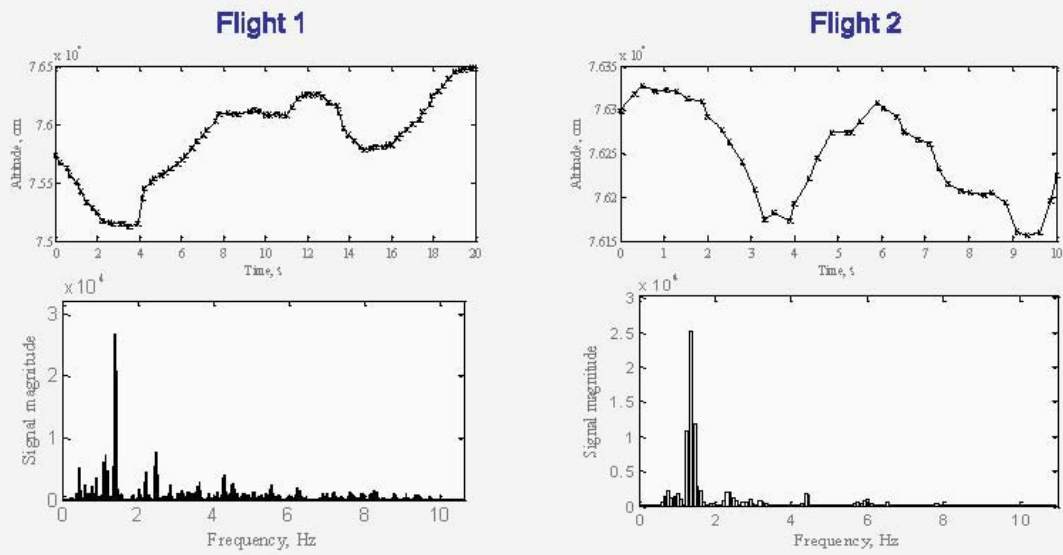
The autonomous ornithopter is a flying test bench for investigation of aerodynamic forces, stability and controls in flapping flight



Flight dynamics of an ornithopter (cont.)

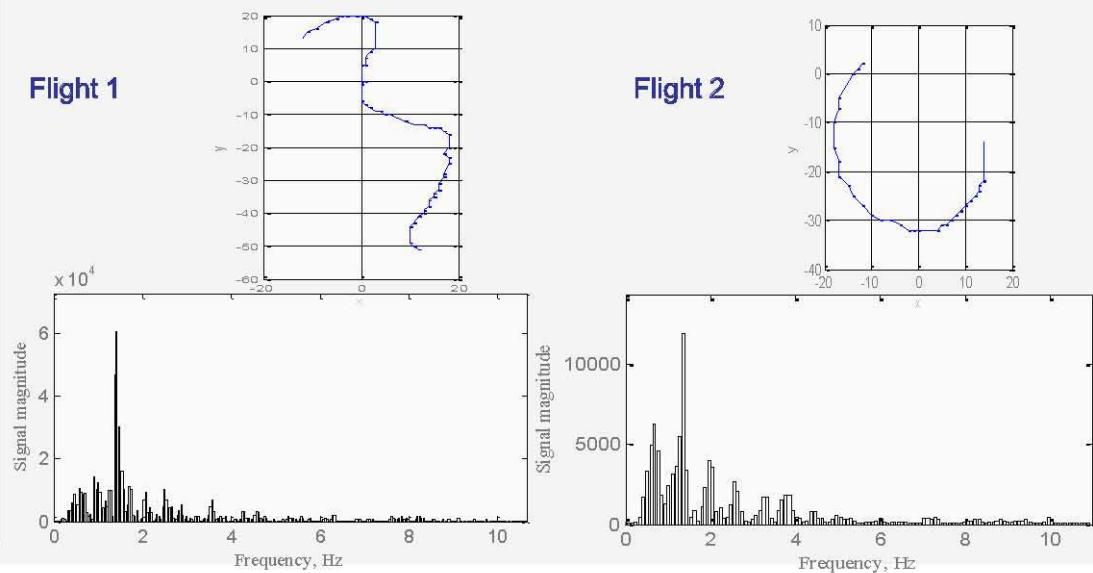


Longitudinal dynamics of an ornithopter in control-fixed level flights



Flight dynamics of an ornithopter (cont.)

Roll dynamics of an ornithopter in control-fixed level flights



More flight tests with more sensors, complete dynamic model identification

Research Transfer Activities for the Current Grant

1. Proof of concept VTOL MAV was designed, built and flight tested
2. UA tied 1st place at 1st US-Asian Demonstration and Assessment of Micro-Aerial and Unmanned Ground Vehicle Technology, Agra, India, 2008
3. Experimental aerodynamics and flight data on fixed and flapping wings MAV
4. Zero-lift drag model for a low Re wing under free stream and slip stream
5. Dynamic model for flapping-wing MAV
6. Shkarayev, S., Moschetta, J.-M., and Bataille, B., "Aerodynamic Design of VTOL Micro Air Vehicles for Vertical Flight," *J. of Aircraft*, 2008 (accepted).
7. Krashanitsa, R., Silin, B., Shkarayev, S., and Abate, G., "Flight Dynamics of Flapping-Wing Air Vehicle," AIAA Atmospheric Flight Mechanics Conference, 18-21 August 2008, Honolulu, Hawaii.
8. Poinsot, D., Bernard, C., Krashanitsa, R., and Shkarayev, S., "Investigation of Flight Dynamics and Automatic Controls for Hovering Micro Air Vehicles," AIAA Atmospheric Flight Mechanics Conference, 18-21 August 2008, Honolulu, Hawaii.
9. Shkarayev, S., Moschetta, J.-M., and Bataille, B., "Aerodynamic Design of VTOL Micro Air Vehicles," 3rd US-European Competition and Workshop on Micro Air Vehicle Systems (MAV07), 17-21 September 2007, Toulouse, France.

Research Transfer Activities for the Current Grant (cont.)

10. Malladi, B., Krashanitsa, R., Silin, B., and Shkarayev, S., "Dynamic Model and System Identification Procedure for Autonomous Ornithopter," 3rd US-European Competition and Workshop on Micro Air Vehicle Systems (MAV07), 17-21 September 2007, Toulouse, France.
11. Moschetta, J.-M., Bataille, B., Thipyopas, C., and Shkarayev, S., "On Fixed-Wing Micro-Air Vehicles with Hovering Capabilities," AIAA Atmospheric Flight Mechanics Conference, Reno NV, Jan 2008.
12. Shkarayev, S., Design, aerodynamics and controls for VTOL MAVs, 1st MAV Workshop, REEF, Florida, May 2007.
13. Shkarayev, S., and Abate, G., Recent studies on aerodynamics and controls for fixed-wing VTOL MAVs, 2nd MAV Workshop, REEF, Florida, May 2008.
14. Shkarayev, S., The Aerodynamics of Membrane Flapping Wings with Applications to Micro Air Vehicles, Summer Faculty Fellowship Program at AFRL, July 2008.
15. Krashanitsa, R., Silin, B., Shkarayev, S., and Abate, G., "Flight Dynamics of Small Flapping-Wing Air Vehicle," *International Journal for MAV Design*, 2008, (in preparation).

This page intentionally left blank

DISTRIBUTION LIST
AFRL-RW-EG-TR-2009-7020

Defense Technical Information Center 1 Electronic Copy (1 File & 1 Format)
Attn: Acquisition (OCA)
8725 John J. Kingman Road, Ste 0944
Ft Belvoir, VA 22060-6218

EGLIN AFB OFFICES:

AFRL/RWOC (STINFO Office)	- 1 Hard (Color) Copy
AFRL/RW CA-N	- STINFO Officer Provides Notice of Publication
AFRL/RWGN	- 1 Copy
AFRL/RWAV	- 1 Copy